12-17-2014

Silicon Doping Profile Measurement Using Terahertz Time Domain Spectroscopy

Chih-Yu Jen

R.I.T

SILICON DOPING PROFILE MEASUREMENT USING TERAHERTZ TIME DOMAIN SPECTROSCOPY

by

CHIH-YU JEN

A dissertation submitted in partial fulfillment of the requirements
for the degree of Doctorate of Philosophy in Microsystems Engineering

Microsystems Engineering Program
Kate Gleason College of Engineering

Rochester Institute of Technology
Rochester, New York
DECEMBER 17, 2014

Silicon Doping Profile Measurement Using Terahertz Time Domain Spectroscopy

By

Chih-Yu, Jen

Committee Approval:

We, the undersigned committee members, certify that we have advised and/or supervised the candidate on the work described in this dissertation. We further certify that we have reviewed the dissertation manuscript and approve it in partial fulfillment of the requirements of the degree of Doctor of Philosophy in Microsystems Engineering.

_____ _____

Dr. Christiaan Richter Date

Assistant Professor (Advisor), Department of Chemical Engineering

_____ _____

Dr. Santosh Kurinec Date

Professor and Head, Department of Microelectronic Engineering

_____ _____

Dr. Stefan F. Preble Date

Associate Professor, Microsystems Engineering

_____ _____

Dr. Zhaolin Lu Date

Associate Professor, Microsystems Engineering

_____ _____

Dr. Agamemnon L. Crassidis Date

Associate Professor and Graduate Director, Department of Mechanical Engineering

Certified by:

_____ _____

Dr. David Borkholder Date

Director, Microsystems Engineering Program

_____ _____

Dr. Harvey J. Palmer Date

Dean, Kate Gleason College of Engineering

ABSTRACT

Kate Gleason College of Engineering
Rochester Institute of Technology

Degree: Doctor of Philosophy **Program:** Microsystems Engineering

Authors Name: Chih-Yu, Jen

Advisors Name: Christiaan Richter

Title: Silicon Doping Profile Measurement using Terahertz Time Domain Spectroscopy

Doping profiles in silicon greatly determine electrical performances of microelectronic devices and are frequently engineered to manipulate device properties. To support engineering studies afterward, essential information is usually required for physically characterized doping profiles.

Secondary ion mass spectrometry (SIMS), spreading resistance profiling (SRP) and electrochemical capacitance voltage (ECV) profiling are mainstream techniques for now to measure doping profiles destructively. SIMS produces a chemical doping profile through the ion sputtering process and owns a better characterization resolution. ECV and SPR, on the other hand, gauge an electrical doping profile from the free carrier detection in microelectronic devices. The major discrepancy between chemical and electrical profiles is at heavily doped ($>10^{20}$ atoms / cm^3) regions. At the profile region over the solubility limit, inactive dopants induce a flat plateau and only being detected by electrical measurements. Destructive techniques are usually designed as stand-alone systems for the remote usage. For an *in-situ* process control purpose, non-contact approaches, such as non-contact capacitance-voltage (CV) and ellipsometry techniques, are currently under developing.

In this dissertation, novel terahertz time domain spectroscopy (THz-TDS) is adopted to achieve an electrical doping profile measurement in both destructive and non-contact manners. For this brand new application, everything has been studied from bottom-up. Firstly, the measurement uncertainty from the change of a bulk wafer thickness and the recognition of the doping profile dissimilarity were proven experimentally. The phosphorus refractive index from 1.2×10^{15} cm^{-3} to 1.8×10^{20} cm^{-3} levels was then generated physically for the modeling of the complex THz transmission and its shift to the Drude Model prediction is explained two scientific mechanisms. Through the experimental demonstrated of the proactical degeneracy, relative strategies were proposed to shrink or break it. The doping profile measurement was finally performed by both methods. We conclude that THz-TDS can be designed as either an either *in-situ* or stand-alone system to estimate a doping profile in semiconductor materials.

ACKNOWLDEDGMENTS

I felt so fortunate to be surrounded by many loving people and now it is my pleasure to thank all of them for their love, encouragement, support and blessings.

First of all, I would like to express my sincerest gratitude to my advisor Professor Christiaan Richter, for his valuable guidance and generous support throughout my entire graduate studies at RIT. His pioneering vision in terahertz development, abundance of knowledge and open-mind spirit inspired and motivated me. Without his insightful suggestions and persistent help, this dissertation would not have been accomplished.

I would like to express my hearty thanks to Professor Stefan F. Preble for sharing his space and instruments for the setup of our THz-TDS system. Without a wonderful maintenance and well calibrated system, I cannot process my experiments smoothly to obtain adequate data for my researches.

I would like to express my deepest appreciation to Professor David Borkholder, Professor Santosh Kurinec, Professor Zhaolin Lu, Professor Agamemnon L. Crassidis and Professor Jiandi Wan for serving as my dissertation committee, willing to share their invaluable opinions and their useful critiques on my research.

I would like to thank staff members in the Semiconductor & Microsystems Fabrication Laboratory (SMFL), especially Mr. Sean O'Brien. Their willingness to give their time and help so generous have been appreciated. I can always get timely answers about equipment operations from Sean to continue my researches. My grateful thanks are also extended to Professor Karl Hirschman and Ms. Patrica Meller, for their kindness and help to me.

I want to express my gratitude to Dr. Ninkov, Mr. Paul Lee, Dr. Liang Cao, Mr. Zihao Wang, Mr. Tarun Mudgal, Mr.Gaurav Tulsyan, Mr. Brendan Mc Namara and Dr. Chu-Yu, Lee, for their help in offering me useful technical discussions. Zihao supported me the SEM analysis for the Si thickness determination and Chu-Yu helped me to explore the possibility of external co-operation. Special thanks should be given to Dr. Wangshi Zhao. As my girlfriend, she gave me encouragement all the time and accompanied me during my ups and downs.

I would like to thank Ms. Yi-Mei, Lin, Dr. Jianming Dai and Dr. Xi-Cheng Zhang for their ECV and Plasma THz supports in my researches. Without them, there is no way to generate the refractive index library to 8 THz: the best research accomplishment of the whole topic. Scientific input regarding the behind mechanisms is kindly fgiven by Dr. Andersen and Dr. Conwell.

Finally, I would like to express my appreciation to my dearest parents, Mr. Hua-Lin Jen, Ms. Sha-Mei Hwang and my younger brother Mr. Tso-Min, Jen. Thanks for their unconditional love to me, trust me and always being on my side.

TABLE OF CONTENTS

LIST OF FIGURES

the reduction in signal at the sampling time alone (i.e. the rest of the pulse waveform is not measured). Note that a sample thicker than the reference would result in a rightward shift and also a reduction in signal at the sampling time. Hence, in practical applications one needs to use a reference sample that is a priori known to be either thicker or thinner than all the samples to be measured or the sampling time should be offset from the reference peak. ··· 40

Figure 3.8 The THz electric field of a pulse transmitted through the reference wafer minus the THz electric field of a pulse transmitted through the sample (etched wafers) with both fields measured at a fixed sampling time (the sampling time was chosen to be the reference sample peak position). The reference sample is the unetched Si wafer and the samples are thinned by the number micrometers indicated on the x-axis. The parameters used in the theoretical prediction of what a perfectly noise free measurement should look, like according to equation 3.4, is $\boldsymbol{\beta} = 5.5\cdot10^{24}$ and A = 1.303 mV and n = 3.42. ··· 41

Figure 3.9 (a) The measured resonant frequency shift for every one of the resonant peaks in the window from 0.3 to 1.5 THz (labeled k = 4, 5,…,17). All peaks were measured for all wafers. The legend shows the amount of silicon etched (δ) for a given wafer. The lines is plots of equation 3.6 using L_0 = 518 μm and n = 3.42 for all wafers and for δ the profilometer measured quantity as shown in the legend. (b) The slope of best fit lines to the data in 3.9a plotted against the amount of silicon etched. The red line is the theoretically predicted

LIST OF TABLES

LIST OF ACRONYMS

SIMS .....Secondary Ion Mass Spectrometry

SRP .....Spread Resistance Profiling

ECV.....Electrochemical Capacitance Voltage

CV .....Capacitance Voltage

THz-TDS.....Terahertz Time-Domain Spectroscopy

SMFL .....Semiconductor & Microsystems Fabrication Laboratory

SBD.....Schottky Barrier Diode

EM.....Electromagnetic

μPCD .....Microwave Detected Photoconductive Decay

FTIR.....Fourier Transform Infrared Spectroscopy

MIR.....Mid-Infrared

NIR.....Near-Infrared

PVMC .....Photovoltaic Manufacturing Consortium

nc-CV.....Non-Contact CV

CVD .....Chemical Vapor Deposition

FIR .....Far-Infrared

UV-Vis.....Ultraviolet–Visible

GaAs .....Gallium Arsenide

E_{THz} .....THz Amplitude

TRTS.....Time Resolved Terahertz Spectroscopy

SOI .....Silicon on Insulator

mc-Si .....Multi-Crystalline Silicon

SiO_2 .....Silicon Dioxide

CW .....Continuous Wave

UR .....University of Rochester

SNR.....Signal-to-Noise Ratio

FWM .....Four-Wave-Mixing

ATC.....Asymmetric Transient Current

THz-ABCD .....THz-Air-Breakdown Coherent Detection

PMT .....PhotoMultiplier Tube

BBO .....Beta Barium Borate

DM .....Dichroic Mirror

DR .....Dynamic Range

DFT .....Discrete Fourier Transform

FWHM .....Full Width at Half Maximum

PV .....Photovoltaic

P_{31}.....Phosphorus

B_{11} .....Boron

HF .....Hydrogen Fluoride

HR-SEM .....High-Resolution Scanning Electron Microscopy

CMP .....Chemical Mechanical Polishing

IB.....Impurity Band

MIT .....Metal-Insulator Transition

LFD.....Logarithmic function diffusion

RFD.....Rational function diffusion

RTP .....Rapid Thermal Annealing

EG .....Ethylene Glycol

DIW.....Deionized Water

BOE.....Buffer Oxide Etch

1 INTRODUCTION

1.1 Terahertz Technique

Terahertz radiation (T-ray, 1 THz = 10^{12} Hz), shown in Figure 1.1, lies in the frequency segment of electromagnetic spectrum between the gap of infrared and microwave regions with well-known frequency (100 GHz – 10 THz), wavelength (30 μm – 3 mm) and photon energy (0.4 – 40 meV). The proper photon energy and long wavelength make T-ray a suitable technique in fields of astronomy [1, 2] as well as analytical science. There was a hard time to implement the terahertz technique because the background noise (25meV, or 6THz at room temperature), resulted from the incoherent light, limits the generation and detection of light in the far-infrared and terahertz range. In year 1985, the first prototype of THz system was developed and used for scientific purposes. Nowadays, continuous-wave THz systems and pulses based THz-TDS have been applied in various research fields, such as biological and medical science [3-6], non-destructive evaluation, homeland security [7-9], quality control [10, 11], ultra-fast computing [12] and so on. Due to uninterrupted technological innovations of photonics and nanotechnology [13, 14], cutting-edge THz devices and high–frequency electronics with ascensive performances continuously benefit coming THz systems in advanced. In the semiconductor field, the position of THz technique is getting raised through researches on devices operated at the THz frequency, like resonant tunneling diodes [15], THz signal-photon detectors [16], schottky barrier diodes (SBDs) [17] and etc. Many historic achievements and fundamental principles of THz researches can be traced back through some review papers [18, 19]. To make THz techniques more popular, developing commercial applications is a must.

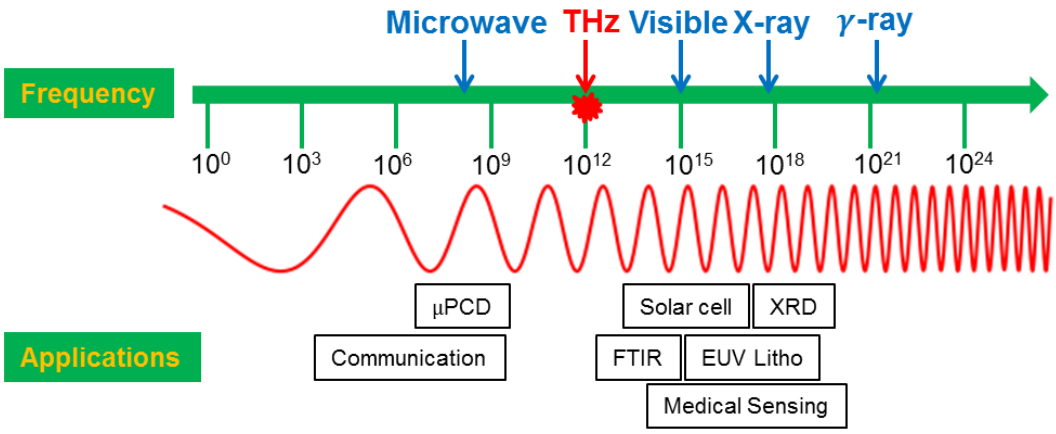

Figure 1.1 The overall electromagnetic spectrum with applications in individual segments.

Free carrier absorptions of two doping levels in all electromagnetic (EM) frequencies are depicted Figure 1.2. THz-TDS over here displays major advantages over microwave detected photoconductive decay (μPCD) [20] and fourier transform infrared spectroscopy (FTIR) techniques [21], which utilize EM wave in neighboring microwave and infrared regions, respectively. In MIR (Mid-Infrared), NIR (Near-Infrared) and visible regions, free carrier absorptions are either negligible and/or obscured by other optical features like impurity absorption, phonon or inter-band absorption due to its weak photon energy (0.4 – 40 meV). Therefore pure behaviors from free carriers are ambiguous in these regions to characterize. Researchers instead focus on studies regarding impurity absorption, phonon or inter-band absorption in above regions. For example, FTIR is generally used to study the impurity absorption and molecule vibration in materials. If any study emphasizes the pure behavior of free carrier, microwave and terahertz frequencies are the viable options for a direct observation. In this dissertation, our research aims at the carrier dynamic and optical properties in silicon utilizing a general THz-TDS. The ultimate goal is to develop a practical metrology for microelectronic industries. The same analytical procedure can be applied to study carrier properties in various semiconductor materials.

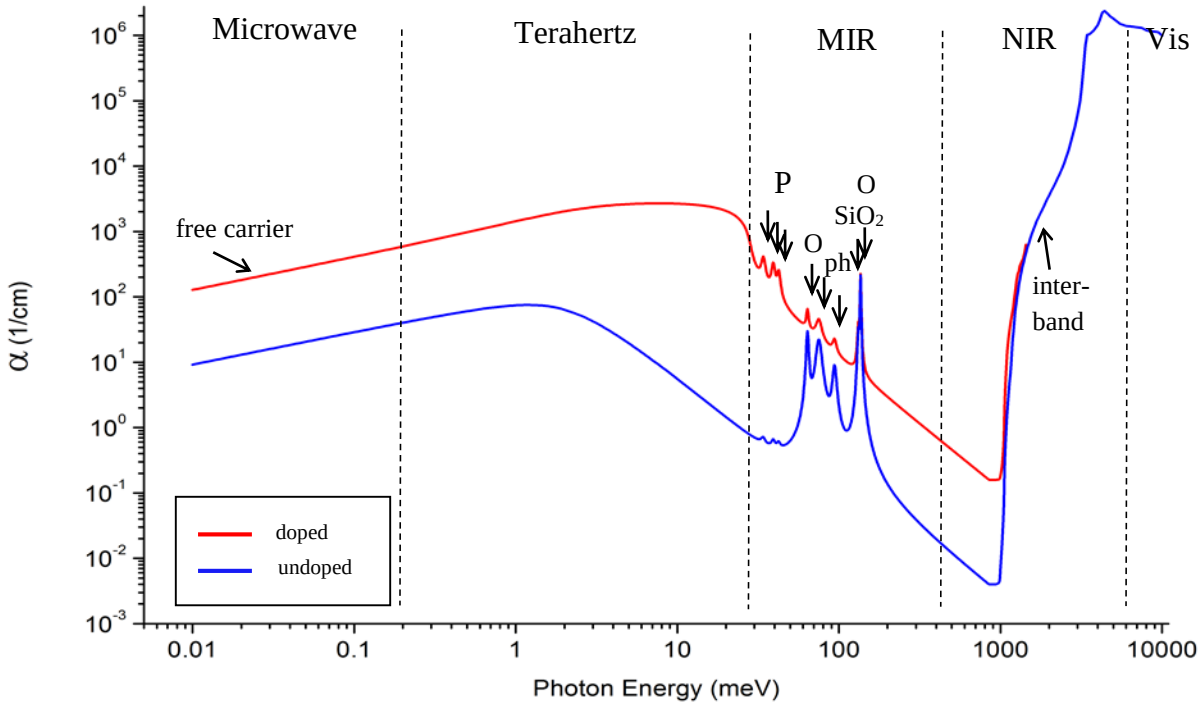

Figure 1.2 Absorption coefficients of phosphorus doped (10^{18} cm^{-3}) silicon and lightly doped (10^{15} cm^{-3}) silicon from the microwave to the visible. This log-log plot of the global optical landscape of Si clearly illustrates (see text) why THz is the optimal spectral window for the metrology we propose. (The physical processes contributing to the optical features are labeled: SiO_2 refers to silica clusters and "ph" stands for phonons, which although weak in nonpolar Si is not completely absent.)

Although photon energy in microwave regions is also low, several advantages make THz frequencies a better option to detect the pure behavior from free carriers. Figure 1.3 shows the susceptibility of the free carrier absorption between moderately doped (10^{18} cm^{-3}) and lightly doped silicon (10^{15} cm^{-3}) from Figure 1.2. There is virtually no contrast between two doping levels above the THz region, excellent contrast in the THz region and moderate to low contrast in the microwave region. The magnitude of this contrast matters because it determines the sensitivity (the magnitude of doping differences or deviations that can be detected). The dispersion (steepness of the slope) matter even more: The dispersion is of critical importance for a metrology of the kind proposed here because it is the differences in the transmittance, reflectance, absorbance and phase delay of different adjacent frequencies (in a single broadband

pulse) through the specimen. These attractive features make THz-TDS an outstanding metrology technique to monitor the electrical performance of the device and can be potentially utilized in the inline process control in the semiconductor fabrication process. Moreover compared to the μPCD with the single frequency information, measured THz spectrum in the frequency domain contains multiple frequencies information, which leads to potentially complicated applications.

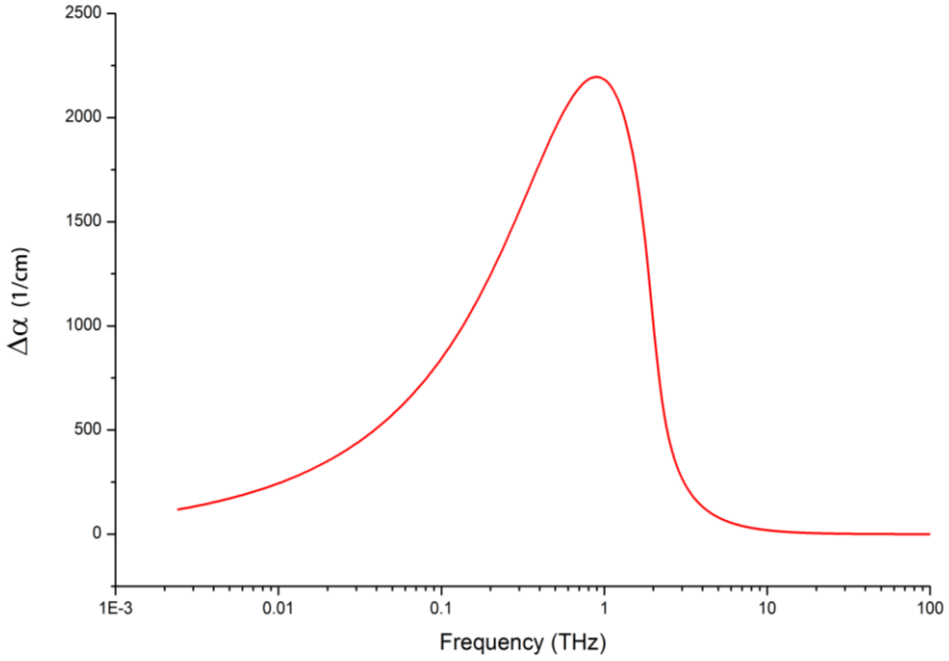

Figure 1.3 The difference of free carrier absorption between 10^{15} cm^{-3} and 10^{18} cm^{-3} P doped Si as a function of wavelength. Note that the free carrier absorption is very weak at frequencies above the terahertz region. At frequencies lower than the terahertz region there is free carrier absorption. However the contrast and dispersion is much less than in the terahertz. Hence, even if a comparable broadband fast microwave technique could be developed it will by necessity have significantly less resolution (capability to accurately resolve the shape of the doping profile) and sensitivity.

1.2 Research Motivation

The motivation of this research is to design a commercial metrology for the prediction of electrical doping profiles in microelectronic devices utilizing the outstanding advantages in THz regions. Nowadays mainstream characterization techniques of doping profile measurements are designed as stand-alone systems, which are hard to feedback measurements in a timely manner.

The brand-new THz-TDS approach enables us to consider a potentially non-contact option. During 2012, the U.S. Photovoltaic Manufacturing Consortium (PVMC) embarked on a 'Pareto exercise' with 38 separate organizations from industry, national labs and academia to identify and prioritize the critical challenges in c-Si metrology. Like several similar panels and workshops this effort identified, among other challenges, the unmet need for: "High-throughput evaluation of the emitter doping process (e.g. doping uniformity, in-line resistivity, junction depth, doping profile measurement on a textured surface). SIMS [22, 23], SRP [24, 25] and ECV profiling [26, 27] are widely used techniques to determine a doping profile measurement but hard to satisfy the demand of the high-throughput evaluation. Different from them, THz-TDS is the only broadband technique in THz regions to deliver an optical metrology, which is capable of achieving a doping profile mapping that is:

- Non-contact / non-destructive
- Fast measurement
- High sensitivity
- High resolution
- Directly measure both the frequency dependent absorption and phase shift
- Provide additional information (mobility, crystallinity, lifetime)

Non-contact techniques open a popular field for the industry to deal with the high throughput production through an *in-situ* process control rom the real-time feedback of tool condition. Merits in THz techniques motivates us to develop an alternative metrology for the inline process monitor purpose.

1.2.1 Summary of Competing Profile Measurement Techniques

A functional comparison regarding the doping profile measurement between the proposed THz technique and common existing alternatives is summarized in the Figure 1.4. Except repeatedly mentioned destructive techniques, CV, non-contact CV (nc-CV) and ellipsometry techniques are belong to non-destructive metrologies, which could be potential competitors to the THz-TDS approach. Currently the most reliable high resolution technique for a doping profile determination is SIMS. This technique is destructive, slow and expensive and measures the chemical profile as opposed to the active doping profile. The CV technique requires that a metal-semiconductor (Schottky) junction be formed with the sample. The capacitance of this junction is then measured at various voltages and an underlying theoretical model (typically the Shockley or depletion approximation model as first proposed by Hilibrand and Gold in 1960 [28]) together with empirical correction factors is used to infer properties of the substrate. Estimates based on this technique are generally acceptable if the junction is sufficiently shallow. The underlying theoretical model and empirical corrections used are relevant to the material measured, where the junction is laterally uniform. Traditional CV instruments predict a doping profile when presented with a sample with the same 'confidence' whether sample properties like crystallinity or passivation exactly fit the model and parameters used or deviate significantly [29, 30]. Hence the conventional CV technique often performs best when measuring surface resistivity and shallow junctions. The detection of heavily doped regions is the limitation in this technique due to a too thin space charge region formed by an applied voltage. Usually profiles with $> 10^{19}$ cm^{-3} regions cannot be precisely determined. The ECV technique exploits this strength by cycling between an etching step and a CV measurement step. As such it can be more accurate than conventional CV but is also destructive and slower. Non-contact CV attempts the conventional CV measurement without the physical contact by using a probe that capacitively

couples to the sample surface, typically a Kelvin probe. State of the art instruments in this field, like Semilab's suite of non-contact CV tools, can measure various useful parameters like "average surface doping", "dielectric capacitance", "flat band voltage" and "total oxide charge" [31, 32]. However thin chemical vapor deposition (CVD) grown epi-layers do not be claimed to reliably map sub-surface doping depth profiles. SRP measures the sheet resistance over a defined distance to determine the surface carrier concentration. Tan *et al* [33] reported the capability of measuring profiles with the ultra-shallow (121nm) junction and obtained a reasonable agreement with the result from SIMS. As a non-contact and non-destructive technique, ellipsometry (particular IR ellisomtery) comes closest to having most of the benefits of the technique proposed here. Commercial far-infrared (FIR) or terahertz ellipsometers is not available at present, but we understand that the Woollam Corporation and collaborators are working on the concept [34, 35]. Ellipsometry is particularly good at characterizing very thin films like passivating layers or anti-reflective coatings [36]. The existing ultraviolet-visible-near infrared (UV-Vis-NIR) ellipsometers do however have a significant disadvantage relative to FIR or terahertz light when it comes to doping profile mapping. It is because 1) free carrier absorption (and the ability to detect the doping profile by the free carrier interaction) decrease roughly by $1/\nu^2$ with ν being the frequency of the light used as a probe – simply put NIR light is significantly less sensitive to the doping profile than FIR light. 2) MIR and NIR spectra are complicated by the presence of impurity (and in some materials phonon) absorption that overshadows the free carrier absorption at resonant wavelengths and makes doping profile determination next to impossible when using these regions of the electromagnetic spectrum (detail interpretation is mentioned in the previous section).

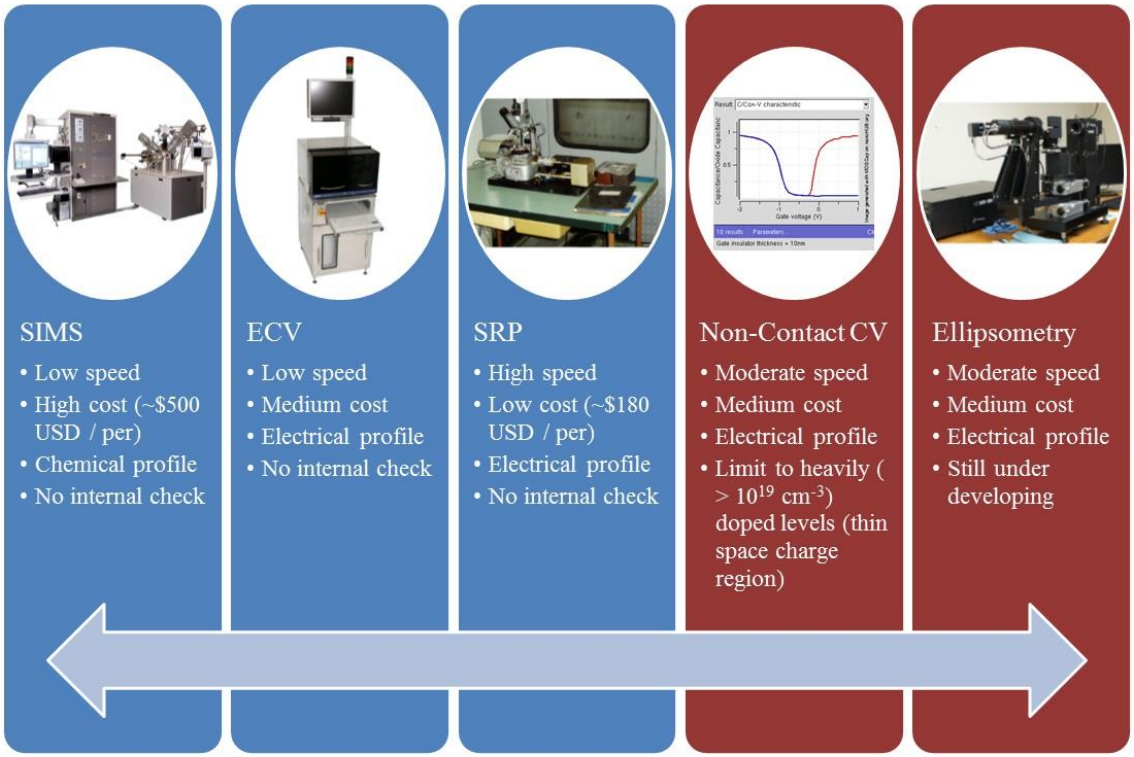

Figure 1.4 The benchmark of various characterization techniques for the doping profile measurement.

1.3 Operating Principle of THz-TDS

THz-TDS can be designed as transmission and reflection mode setups, where a transmission mode system is adopted in the whole research here. Pulses based THz-TDS relies on a relatively high energy laser source to achieve photon-excitation, THz pulse generation and detection. The schematic of THz-TDS, as depicted in Figure 1.5 (a), starts with a femtosecond laser produced optical pulse train (~250fs, 835 nm) by a mode-locked Ti:Sapphire laser system. As generated THz pulses have sub-picosecond duration, they are broadband with significant power from tens of GHz up to a few THz. The laser pulse train is then divided into two parts by a film-coated beam split. One part is directed to hit a THz emitter, made by a BATOP interdigital photoconductive THz antenna with microlens array, gallium arsenide (GaAs) chip with a low temperature grown GaAs absorbing layer and hyperhemispherical silicon lens. The GaAs chip

with a low temperature grown GaAs absorbing layer contains larger amount defects to confine the carrier recombination time in picosecond level and a 15V DC bias across the antenna conducts the collection of photo-excited electron-hole pairs to produce THz EM waves. These waves are well approximated by oscillating Hertzian dipoles, whose radiated electric field is proportional to the time derivative of electron-hole pairs. The Hi-resistivity silicon hyperhemispherical lens is set up to guide randomized THz waves to the same direction, enhancing the coupling efficiency of the THz pulses train between the photoconductive dipoles and free space (shown in Figure 1.5 (b)). EM THz pulses then propagate in the free space and reach a placed specimen. After penetrating the specimen, transmitted pulses with amplitude and phase changes are measured by an ultrafast THz detector. The photoconductive detection of THz radiation pulses are implemented through an inverse process of THz emission and requires the other part of the optical laser pulse train as a reference signal. For that, a Zaber delay stage with a moving mirror manipulates the arrival time of transmitted pulses to interfere the photocurrent generation, which is proportional to E_{THz}. (THz electric field) A Lock-in amplifier then processes the internal calculation and collection based on the photocurrent generation to map out an entire terahertz pulse. The traveling distance of the THz generation side has to be the same as the one in the detector side to assure the arrival of the same pulse. An air reference or a substrate specimen is generally required to cancel out the background noise. The power spectrum in THz region is very sensitive to the water vapor and several absorption peaks has been discovered at specific frequency locations [37]. To eliminate these water vapor induced noise during the measurement, a nitrogen or compressed air with a much lower humidity is generally injected into a sealed box. Labview graphic interface organizes the overall system operation to perform a real-time and convenient measurement. The specialty of THz-TDS is to directly extract both real and

imaginary part refractive index inside the specimen without resorting to the Kramers-Kronig relations.

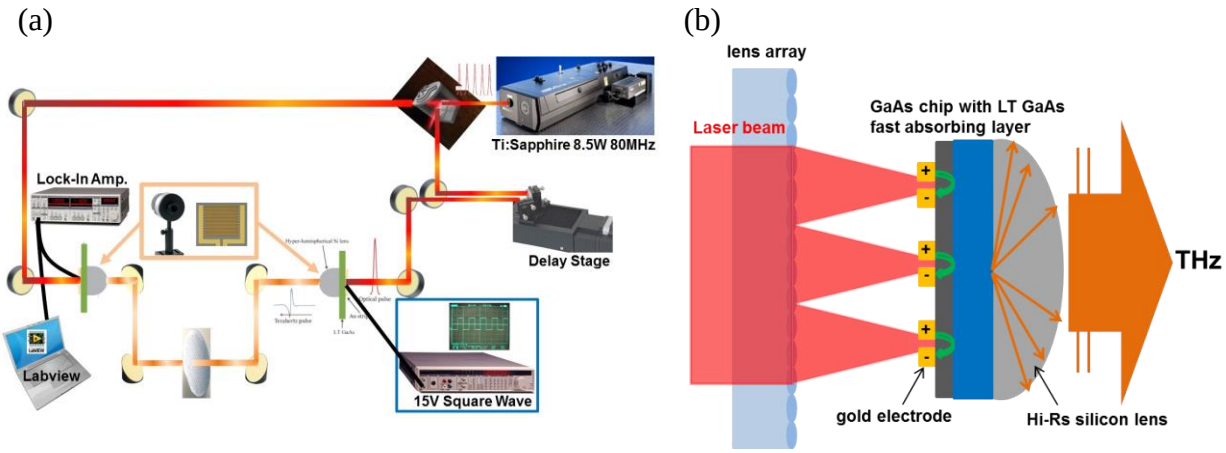

Figure 1.5 (a) The schematic setup of a transmission mode THz-TDS (b) The operation principle of the generation of THz radiation

The system described above mainly does the characterization of intrinsic carrier dynamic and optical properties in materials. Transient carrier dynamic in materials can also be directly investigated through this system in picosecond to nanosecond timescales by splitting out an additional laser source to photo-excite extra carriers. The THz detection is generally synchronized right after the photo-excitation to record the free carrier distribution as a function of time (carrier lifetime). It is so called time resolved terahertz spectroscopy (TRTS). People utilize this lifetime information to interpret various properties in nanomaterials such as crystal structure. Hence TRTS is considered as a powerful option for the academic research of advanced materials. We start from the usage of a standard THz-TDS in this research for the potential commercialization purpose and may consider this TRTS system in the future.

1.3.1 Pro's and Con's of THz-TDS

To summarize, THz-TDS has a number of advantages over above incoherent techniques:

- The time-gated detection of THz pulses allows all spectrometer components to be

used at room temperature.

- The direct complex refractive index extraction doesn't need the usage of the Kramers-Kronig relations.

- Fabry-Perot reflections in thick substrates can be removed by windowing the time-domain data.

- The time-resolved photoconductivity on picosecond timescales can be measured in a non-contact manner.

However, there are also disadvantages to limit the population of THz-TDS, such as a costly ultrafast laser and a narrower bandwidth than FTIR. While using a reflection mode THz-TDS, the induced phase-sensitivity is more apparent than the transmission geometry. The position of mirrors needs to be precisely determined to prevent phase errors entering into the calculated optical properties [38, 39].

1.4 Contributions to Terahertz Science and Technology

Key contributions to the terahertz community in this dissertation are:

1. Explore the potential application of utilizing a typical THz-TDS to monitor material thicknesses. The proof of concept demonstration is done on a lightly doped silicon wafer. The same analytical procedure can be applied to other materials.

2. Demonstrate the doping profile recognition in silicon using a typical THz-TDS. The experimental result suggests the practical feasibility of an *in-situ* monitor after the diffusion and ion implanted process.

3. A unique strategy is designed using silicon-on-insulator (SOI) wafers to physically generate a complex refractive index library of phosphorus dopant in silicon from concentrations 1.2×10^{15} cm^{-3} to 1.8×10^{20} cm^{-3}. Phosphorus refractive index in silicon follows the Dude model estimation and the offset can be interpreted physical mechanisms. The same method can be utilized to generate libraries from others dopants and semiconductor materials in heavily doped regions.

4. Although THz-TDS provides abundant information for a doping profile measurement, measurement noise from various sources could induce the multiple degeneracy and lead a wrong profile prediction. How serious of the multiple degeneracy is theoretically studied through the numerical simulation and experimentally proven using various SIMS profiles.

5. Non-contact and destructive doping profile measurements are conceptually demonstrated and compared with SIMS profiles. The same flat plateau in heavily doped regions is confirmed by the predicted electrical doping profiles from other techniques.

1.5 Dissertation Overview

This dissertation presents numerical and experimental demonstrations of silicon doping profile measurements using a transmission mode THz-TDS. These results are structured as follows.

Chapter 1 introduces the terahertz technique, research motivation, potential competitors and operation principle of THz-TDS. The commercial application of the whole research is also addressed.

Chapter 2 introduces Drude model, Drude-Smith model and transfer matrix, which are essential theories used in the whole research to calculate complex THz transmission. A literature review about the progress of the THz-TDS research in the semiconductor field is also summarized to emphasize the specialty of our research.

Chapter 3 describes the THz measurement uncertainty from the thickness change of a lightly doped silicon wafer. In our research, the estimation of complex THz transmission requires the knowledge of a precise bulk silicon thickness. Resolutions of all indices from single THz measurement are compared and the result indicates sub-micron (~200 nm) to micron resolutions. The frequency index, Fabry-Pérot cavity resonances, is finally adopted in the whole research due to its sub-micron resolution. The same analytical procedure can be applied to other materials.

Chapter 4 conceptually presents the recognition of phosphorus and boron profiles using a typical THz-TDS. Various profiles through different implant dosages and drive-in time in silicon are recognized by the residual THz radiation after penetrating through the sample. Surface morphology is proven to overcome by seeing no difference on multi-crystalline (mc-Si) solar cells with ~4μm texture heights. The *in-situ* process monitor after the diffusion and ion implanted process is feasible in both semiconductor and photovoltaic industries.

Chapter 5 introduces the invented strategy of generating the phosphorus refractive index library in THz regions. The formation of an abrupt and thin doped layer in silicon makes this method special and the SOI wafer is chosen because of its excellent dopant stop capability in the middle silicon dioxide (SiO_2) box layer. This empirical library covers refractive indices from $1.2\times10^{15}cm^{-3}$ to 1.8×10^{20} cm^{-3} and surprisingly is close to the estimation from Drude model. The offset is well interpreted by electrons in impurity bands with heavier effective masses and THz

emissions. The library is then used to calculate complex THz transmission after penetrating distinct doping profiles.

Chapter 6 discusses the multiple degeneracy problem through the numerical simulation and utilizes liquid diffusion profiles with kink-and-tail distributions as an example. Suitable mathematical models to depict the kink-and-tail feature are also introduced in this chapter. Multiple degeneracy represents that several doping profiles own the same THz measurement. The modeling result indicates that the theoretical degeneracy does not exist but the measurement uncertainty induced practical degeneracy impacts the profile measurement a lot. The existence of the practical degeneracy is proven through various SIMS profiles and relative strategies to break the practical degeneracy are also proposed.

Chapter 7 firstly calibrates the empirical refractive index library from Chapter 5 and then conceptually demonstrates the performance of doping profile prediction in both non-contact and destructive ways. In the destructive measurement, the anodic oxidation process is combined with a typical THz-TDS to implement a doping profile construction and displays the discrepancy in heavily doped regions to the SIMS profile. Other layer removal techniques with a similar performance of thickness control can be considered as alternative options. In the non-contact prediction, proper initial guess profiles along with the proposed fitting strategy are combined to successfully predict close doping profiles with benchmark to their SIMS measurements. The development of advanced fitting algorithms and practical programming are left as future work.

Chapter 8 summarizes work as well as an outlook for future work.

Chapter 9 lists all the publications and scheduled submissions.

2 BACKGROUND THEORY

In this chapter, the introduction starts from historical and academic reviews of THz techniques, followed by the THz generation and detection through three main techniques. Drude and Drude-Smith models are important theories to estimate conductivities in various carrier concentrations. Those information is put into the transfer matrix to calculate the optical THz transmission and reflection after penetrating through multiple layers.

2.1 Literature Review of Applications of Terahertz Techniques

The potential contribution to the terahertz community by the research proposed here is best appreciated by considering it in the context of a brief history of terahertz spectroscopy. The diagram in Figure 2.1 summarizes the major developments in this field. The experimental physics of generating and detecting broadband terahertz pulses has been largely perfected starting with the discovery of the Austin switch in 1975 [40] and culminating in new directions like air plasma generation [41]. The first THz spectroscopy system was designed in 1985 and then applied in various research topics. An understanding of how to use far-infrared pulses to probe matter has been developed and reviewed by Schmuttenmaer *et al.*[42]. In recent years, the first commercial THz-TDS with affordable robust implementations was designed by the company Z-Omega and brought into the market through continuous technology innovation. Clearly the current moment presents a unique opportunity for research that can bridge and combine the capability to generate and detect THz developed over decades with the materials and spectroscopy know-how resulting from this capability. New opportunities, driven by

advances in fiber lasers, are considered for implementation in future manufacturing control and metrology.

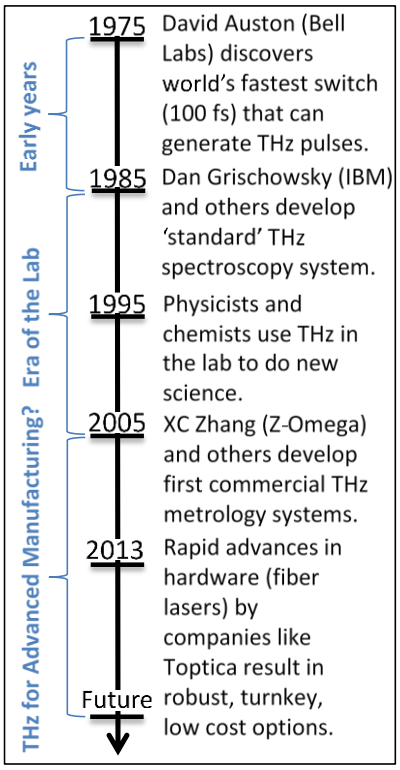

Figure 2.1 Historical development of terahertz techniques

Compared to a typical THz-TDS, TRTS is more often employed to study the transient carrier dynamic in advanced materials by measuring a signal change in a sub-picosecond level, which makes TRTS a powerful technique for the fundamental science research. In 2002, Ferguson *et al.* reviewed how continuous wave (CW) and pulsed THz system being used in the material researches such as biomolecule and semiconductor [18]. In the same year, Averitt *et al.* discussed the application on colossal-magnetoresistance manganites and high-temperature superconductors and admitted the system capability in the dynamics of quasiparticles at the Fermi level [43]. In 2004, Schmuttenmaer *et al.* reported studies in bulk semiconductors, semiconductor heterostructures and superconductors using TRTS as well as the experimental

considerations from the system design point of view [42]. In 2007, Masayoshi *et al.* summarized state-of-the art THz sources at that moment and applications in industries and basic science [13]. In 2010, Němec *et al.* reviewed studies in chemical filed, emphasizing polymer-fullerene heterojunctions and dye-sensitized nanoparticles [44]. In 2011, similar reviews were updated in fields of organic molecules, aqueous solutions, bulk and nanostructure semiconductors, imaging techniques, superconductors and correlated electron systems by Baxter, Jepsen, Ulbricht, Basov and Adam *et al.* [14, 45-48]. Recently, a review in solid state system was reported by Lloyd-Hughes *et al.* in 2012 [49]. Extensively academic researches in chemical and physical fields indicate the popularity of terahertz techniques. However, our research goal aims at the practical application with the consideration of future commercialization. Instead of using expansive TRTS system, the whole research is initialized on a typical transmission mode THz-TDS system.

2.2 Generation and Detection of THz Radiation

To understand the proper option in the future system design, popular THz techniques are introduced and compared in this section. Three major techniques are now utilized to generate and detect THz radiation. What we use in the research to generate the THz radiation is belong to the photoconductive antenna technique. Frequency photo-mixing technique might be the most cost-effective solution to generate the THz information directly in frequency domain. To acquire a broader bandwidth information, Xi-Cheng, Zhang's group at University of Rochester (UR) innovated the air plasma system [41] and has reported the THz bandwidth up to 40 THz.

2.2.1 Photoconductive Antenna Technique

The detail schema and operation principles of this technique have been addressed in the section 1.3. Although a pulses based laser system makes this technique not the cheapest option to

use, an excellent signal-to-noise ratio (SNR) supports its popular usage in academic fields. The major disadvantage of this technique is its limited bandwidth.

2.2.2 Frequency Photo-Mixing Technique

Different from the photoconductive technique, frequency photo-mixing technique overlaps and focuses two lasers with a frequency difference in THz regions onto the semiconductor device to generate CW radiation in the frequency domain directly. Free space THz photo-mixing was firstly demonstrated by Brown *et al.* in 1995 with frequencies up to 3.8 THz [50, 51]. The advantages of this technique are tunable frequency regions from 300 GHz to 3 THz, 1MHz spectral resolution and cost-effective implementation by fiber lasers. However the poor radiation power (~10^{-8}W) limits its application, especially for the system design in a transmission mode.

An example CW-THz spectrometer was mentioned by Hindle *et al.* in his 2008 paper [52]. Two Ti:Sapphire lasers with a THz frequency separation and identical polarisations are mixed in free space or fiber optic couplers and focused onto a semiconductor device (Photo-mixer), which can be the same as the one described in the section 1.3. Therefore, the major system difference to a THz-TDS is the laser source. The THz radiation power (P_{THz}) strongly correlates to the incident laser powers P_1 and P_2, the applied voltage V_{BIAS}, the charge lifetime τ, the antenna resistance (R) and capacitance C, and the difference frequency ω_{THz} ($\omega_1 - \omega_2$). The formula $\frac{V_{BIAS}^2 (P_1+P_2)^2 R}{(1+\omega_{THz}^2\tau^2)(1+\omega_{THz}^2 R^2 C^2)}$ is typically used to identify the P_{THz}. The maximum emission is generally limited by the breakdown voltage of the electrode array and the thermal management of the substrate. Different from a THz-TDS, a bolometer is set up to detect the power of incident THz radiation and the overall bandwidth information is calculated by a Lock-In amplifier and collected by tuning the separation of THz frequencies.

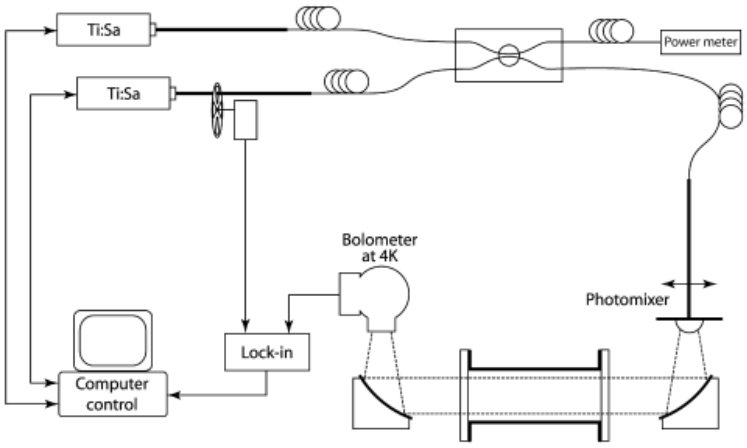

Figure 2.2 Schematic diagram of a CW-THz spectrometer [52].

2.2.3 Air Plasma Technique

Air plasma THz technique is another type of photo-mixing technique, which utilizes the optical rectification from a pulses based laser system. The existing nonlinear optical rectification techniques are improved by exciting ambient air or selected gases with intense femtosecond laser beams to generate and detect pulsed THz radiation with a high peak electric field and ultra-broad bandwidth up to 30 THz [41]. THz emission in gas plasma, shown in Figure 2.3 (a), can be generated through the ponderomotive force from single-wavelength optical excitation [53] or the laser mixing of a fundamental bean (ω) and a second harmonic beam (2ω) [54-57], which are well estimated by the full-quantum mechanical model, a bridge between the four-wave-mixing (FWM) model and asymmetric transient current (ATC) model [41, 54, 57]. The detection process lies in a third-order nonlinear process and was named as THz-air-breakdown coherent detection (THz-ABCD) by sensing a second harmonic photon (2ω) from two fundamental photons (ω) + one THz photon ($E_{2\omega}^{THz} \propto \chi^{(3)} E_{\omega} E_{\omega} E_{THz}$) [58, 59]. To detect $E_{2\omega}^{THz}$, the coherent local oscillator $E_{2\omega}^{LO}$ is required by focusing the ω frequency laser beam intensively to ionize air. The cross term $E_{2\omega}^{THz} E_{2\omega}^{LO}$ is measured by a photo-multiplier tube (PMT) to record the amplitude of THz radiation, shown in Figure 2.3 (b).

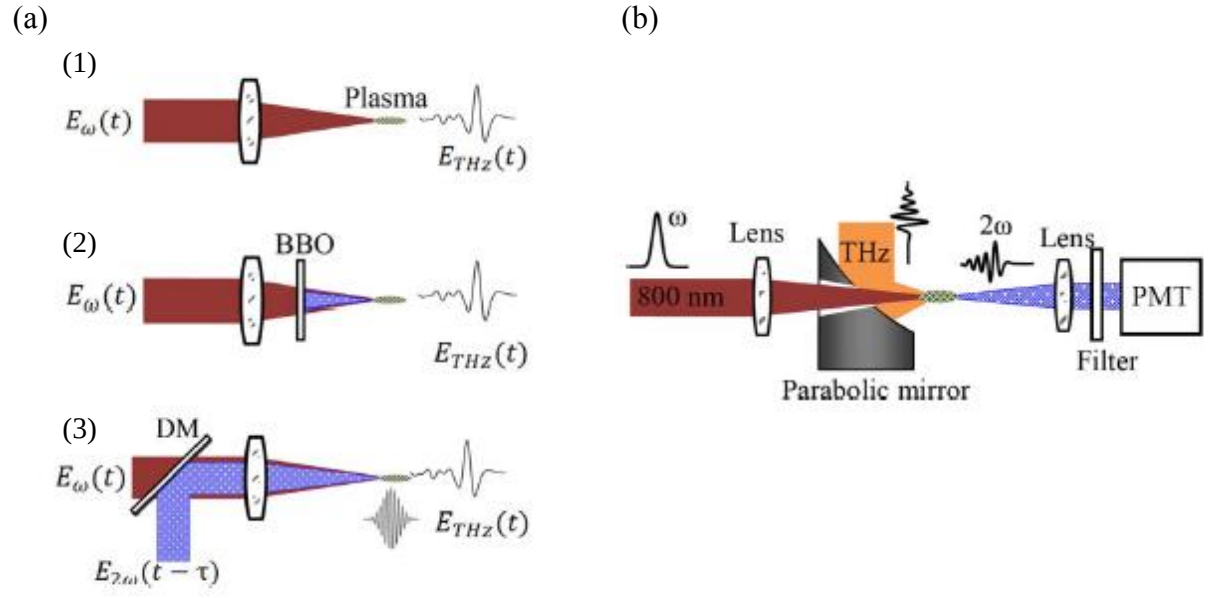

Figure 2.3 (a) Schematic illustration of three ways to generate THz radiation in gases. (1) Ponderomotive force drives electrons and ions to generate THz radiation in single optical beam excitation (ω or 2ω). (2) Two color excitation (ω and 2ω) to generate THz radiation. A fundamental beam (ω) is focused through a thin beta barium borate (BBO) crystal to generate second harmonic (2ω). (3) A dichroic mirror (DM) synchronizes fundamental and second harmonic beam to generate THz radiation. (b) Schematic diagram of the setup of THz radiation detection. The parabolic mirror mixes ω probe beam and THz radiation in the ionized air to generate 2ω optical signal, which is detected by a PMT [41].

2.3 Physical Theories Utilized in the Research

The specialty of THz-TDS is the direct measurement of the frequency dependent permittivity in a dielectric material as well as a complete description of its interaction with electromagnetic spectrum but requires no Kramers-Kronig relations. The square root of the permittivity is known as the complex refractive index. Fundamentally, the complex refractive index ($\tilde{n} = n + i\kappa = \sqrt{\epsilon\mu}$) is the term where the dielectric function (or permittivity, $\epsilon(\omega) = \epsilon_1(\omega) + i\epsilon_2(\omega)$) describes how easily an electric field penetrates the medium and the permeability (μ) details the magnetic response. The dielectric function generally contains a significant imaginary part ϵ_2, which is resulted from the carrier absorption. The corresponding conductivity σ of mobile charges is also complex ($\sigma(\omega) = \sigma_1(\omega) + i\sigma_2(\omega)$) to depict a model of

conduction and the material properties. The conductivity expression is valid for a monochromatic plane wave propagating in the $\hat{k}$ direction with a time dependent electric field $E(t) = E_0 e^{i(kr-\omega t)}$. Changes from above parameters provide essential information to achieve a doping profile measurement.

2.3.1 Drude Model

Drude-Lorentz model describes how the complex refractive index changes as the function carrier concentrations and was proposed by Paul Drude in 1990 to explain the transport properties of electrons in metals [60]. The major assumption of the model is that elastic scattering events are formed in a free electron gas with a complete momentum randomization, which means electron-hole plasma is treated as a non-interacting gas (energy independent). Any long-range interaction between electrons and ions or between the electrons is neglected except instantaneous collisions. Both DC and frequency-dependent conductivity are therefore determined through following equations.

$$\sigma_0 = \frac{Ne^2\tau}{m_0} \tag{2.1}$$

$$\sigma(\omega) = \frac{\sigma_0}{1-i\omega\tau} \tag{2.2}$$

The Drude response describes that the real component of the conductivity achieves its maximum at DC (σ_0) and the maximum of the imaginary component occurs at the radial frequency corresponding to the inverse scattering time τ of the carriers ($\frac{\sigma_0}{1-i}$). In real metals the characteristic frequency $\frac{1}{\tau}$ is in the infrared frequency range, which makes the response not to be found experimentally. For materials with a much lower frequencies $\frac{1}{\tau}$ like certain doped semiconductors, frequency-dependent conductivity was found that closely follows the equation

2.2. In terms of the scattering times, many modifications can be found in the literatures [61-63] under specific material properties. Drude-Lorentz model often fails when the electron scattering rate is energy dependent. When $E_{THz} > 4MV\,m^{-1}$, the THz pulse may accelerate electrons sufficiently to alter their scattering rate, make Drude model no longer sufficient. However, the electric field in our system is lower than above value to avoid this insufficiency.

2.3.2 Drude-Smith Model

There are circumstances when adding additional scattering mechanisms to the Drude model is not enough to describe the frequency dependent conductivity, especially the displacement under E_{THz} becomes comparable to the dimension L of thin film or nanostructure materials. Under this circumstance the conductive response of the medium will differ significantly from that of the bulk material. For the silicon case (m^*=0.28m_e, $\upsilon \sim 2 \times 10^5 ms^{-1}$, and τ~100fs), the estimated L is < 20 nm. Hence N.V. Smith proposed a classical modification to the Drude model that allows for significant deviation from the general Drude features [64, 65]. The model considers the inelastic scattering of the carriers by introducing a memory parameter c, which describes the fraction of the carrier's initial momentum preserved after a scattering event. The frequency dependent conductivity is then illustrated in equation 2.3 by adding a square brackets term that accounts for the fraction of the carrier's initial velocity retained after experiencing the n_{th} collision, c_n.

$$\sigma(\omega) = \frac{\sigma_0}{1-i\omega\tau}\left[1 + \sum_{n=1}^{\infty} \frac{c_n}{(1-i\omega\tau)^n}\right] \tag{2.3}$$

If the carrier's momentum is randomized, $c_n = 0$, resulting to the typical Drude-model. When c = −1, the real part of the conductivity is 0 at DC and the imaginary part of the conductivity is negative at low frequencies. Then the conductivity is dominated by

backscattering. In N.V. Smith's past work, only the first term in the summation is retained. The assumption behind is that the carrier retains part of its initial momentum during the first scattering event, but the velocity is randomized in subsequent scattering events. This modified model is typically used in nanomaterials but our research since the Si substrate wafer we used behaves as a buk material.

2.3.3 Transfer Matrix Method at Incident Angle

Transfer matrix is typically used to describe the transmission and reflection behavior of light in multi-layer films as a function of complex refractive index. The transmitted and reflected wave vector and electric field of an incident light on a single dielectric layer is described in Figure 2.4 as a simplified example. E_0 is the electric vector of the incident beam (THz radiation), E_0' is the reflection beam and $E_T$is the transmission beam (measured THz). The transfer matrix indicates that the overall transmission (reflection) is the sum of an infinite number of transmissions (reflections), which are described by the Fresnel equations. Therefore a system matrix M, given by equation 2.4, is used to describe the whole transmission and reflection coefficients after penetrating a stack of layers $L_1 \dots L_n$. While taking certain titled angles into the consideration during the measurement, the effect is performed in cosine and sine terms to make the equation more complicated.

$$M = \begin{bmatrix} coskL & \frac{-i}{n_1} sinkL \\ in_1 sinkL & coskL \end{bmatrix} = \begin{bmatrix} A & B \\ C & D \end{bmatrix} \; where \; M = M_1 M_2 \dots M_n \qquad (2.4)$$

In equation 2.4, k ($\frac{n_1 \omega}{c}$) is the wave number, L is the total layer thickness and n_1 is the refractive index of the medium. During the equation derivation, the electric and magnetic fields are considered to be continuous at each interface. The complex transmission $\frac{E_T}{E_0}$ (t) and reflection

$\frac{E_0'}{E_0}$ (r) is then abbreviated as a matrix form in equation 2.5 and their solutions (equation 2.6) are utilized in our modeling process.

$$\begin{bmatrix}1\\n_0\end{bmatrix}+\begin{bmatrix}1\\-n_0\end{bmatrix}r=M\begin{bmatrix}1\\n\end{bmatrix}t \tag{2.5}$$

$$t=\frac{2n_0}{An_0+Bnn_0+C+Dn},r=\frac{An_0+Bnn_0-C-Dn}{An_0+Bnn_0+C+Dn} \tag{2.6}$$

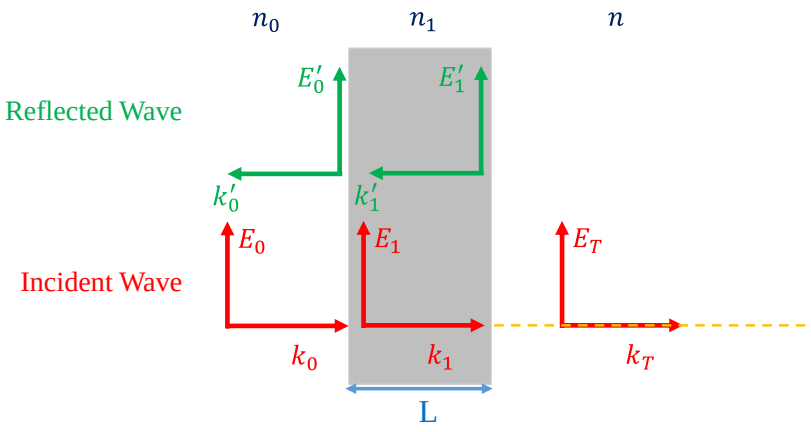

Figure 2.4 The schematic of the transmission and reflection of light in a single dielectric layer. This example is used to conjecture the situation in a multiple layers structure.

2.4 Concept of Doping Profile Prediction using THz-TDS

Predicting a doping profile relies on the interaction of THz radiation from additionally inserted free carriers. THz transmission, absorption and reflectance are all beneficial information but we initialized the research by using just a transmission mode THz-TDS. Three distinct features (see Figure 2.5), including a measured SIMS profile, a theoretical perfect "step" profile and a linear profile, are given as an idea to theoretically forecast the performance of the profile prediction, covering the frequency range up to 5 THz. Exactly the same dopant atoms (the same profile area) is set up in these three profiles to purely study the effect from the profile shape. Figure 2.5 indicates that the change of profile shape itself induces significantly different THz

transmission, absorption and reflectance. Therefore, different profiles are expected to unlikely have exactly the same THz information. The doping profile prediction is basically solving an inverse problem by matching abundant THz information in the frequency domain. The inverse problem of correlating the measured THz requires a 'library' of the frequency dependent complex refractive index and is in general mathematically over-determined by solving one dimensional profile through multiple dimensional information from measured THz information. Naturally the bandwidth and frequency resolution from THz measurements determine and place limits on the spatial resolution of the doping profile.

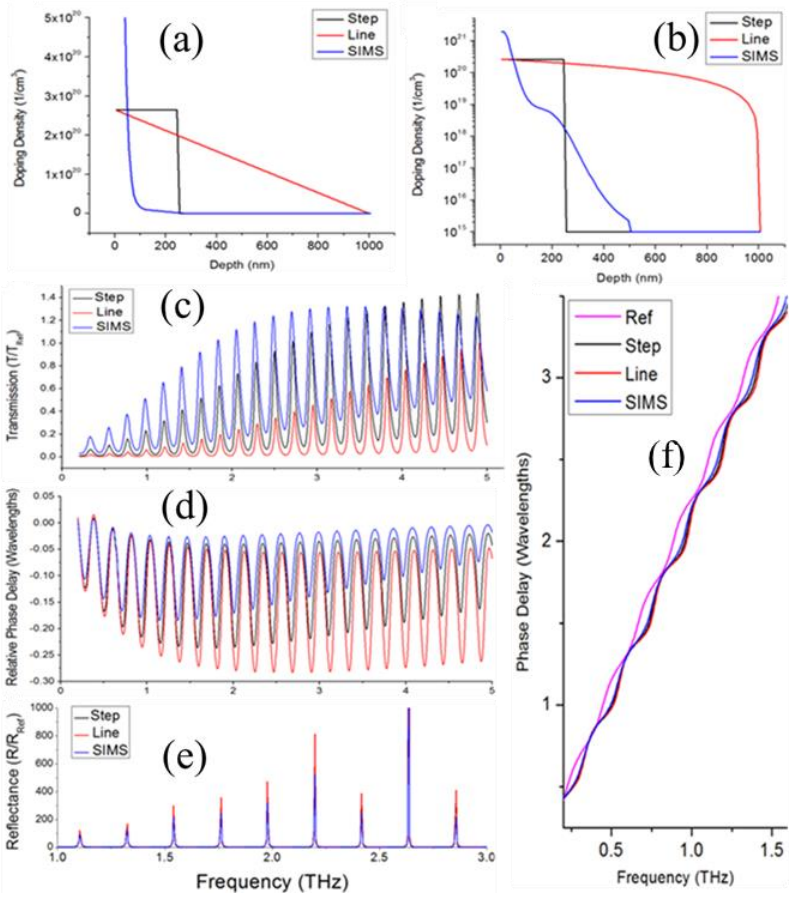

Figure 2.5 (a-b): plots of three doping profiles (the same profiles shown on a linear (a) and a log (b) scale. The "SIMS" profile is an actual typical "kink and tail" profile (measured with SIMS). The other two profiles are theoretical profiles with the exact same amount of P dopant (as in the SIMS sample) distributed as a line or a step respectively. (c) to (f): The simulated transmission (c), phase delay (d, f) and reflectance (e) terahertz spectra of these profiles.

3 SILICON THICKNESS MEASUREMENT WITH THZ-TDS: RESOLUTION AND IMPLICATIONS

When receiving silicon wafers from a supplier, people generally trust the thickness value marked on the label. The crystal structure usually dominates the overall performance in most semiconductor devices and most research topics don't care about the bulk wafer thickness that much. Since we are utilizing a transmission mode THz-TDS, the situation is therefore opposite. To guarantee an accurate profile predictiont, understanding how the change of thickness in silicon impacts the THz radiation is critical, especially in a lightly doped level with a negligible dispersion. For our research purpose, we researched resolutions of all possible indices from a THz-TDS measurement under a ~10^{15}cm^{-3} doped silicon wafer. Many literatures have discussed a similar work from different angles but none of them did the same systematic and practical study like us. The potential application from this topic is an *in-situ* bulk thickness determination using a typical THz-TDS and the same analytical procedure can be applied to various materials. Below content has been published by "*Journal of Infrared, Millimeter, and Terahertz Waves*" in 2014.

3.1 Introduction

THz-TDS provides a direct measurement of the far-infrared complex refractive index of materials. Whenever THz-TDS data is analyzed or "worked up" to extract the refractive index of the sample the sample thickness needs to be supplied by the spectroscopists [66-70]. The thickness therefore needs to be known a priori or measured by different means. The optimal methodology for extracting material parameters (the complex refractive index) from raw terahertz (THz-TDS) data has by necessity been a central topic in the THz-TDS literature

receiving treatment from many prominent researchers. This study is a complement and refinement of the widely used and cited work of Duvillaret and Coutaz discussed below [66, 71-73]. Following Duvillaret and Coutaz's approach published around 2000 several other terahertz researchers contributed perspectives and results on the role of sample thickness in THz-TDS, among them Mittleman [69], Koch [68], Naftaly [74], Withayachumnankul and co-workers [75, 76] and Grischowsky [77, 78]. In all these works the primary focus is on improving the accuracy of complex refractive index measurements with the THz-TDS technique. All these authors identify sample thickness as a critical factor towards this end. Occasionally it has been proposed that THz-TDS also can be used as a metrology tool for measuring sample thickness itself [17, 66, 68-70, 79].

In this chapter we will:

1) Systematically describe five approaches by which THz-TDS can be used to measure film or sample thickness.

2) Develop a basic optical model for every approach and evaluate the accuracy of these models when applied to the case of lightly doped silicon wafers.

3) Measure and compare the resolution of all approaches treated.

Of wider use than the direct question of how accurate THz-TDS can be as a tool for measuring film or sample thickness is the related inverse question: If the value for sample thickness used in a given data workup algorithm is assumed to be L', and the actual sample thickness is L, with $\Delta L = L - L' \neq 0$, then how large will the resulting error in the extracted refractive index be? One can calculate the answer to this question for any given material at any given frequency if one also knows what the measured THz amplitude and phase would be if the

THz-TDS pulse indeed was transmitted through a hypothetical sample with thickness *L'*. This chapter quantitatively studies the variation of the transmitted THz amplitude and phase as a function of small changes in sample thickness specifically for the case of lightly doped silicon. This chapter therefore provides information that can be used to generate quantitative estimates of the uncertainty in the extracted refractive index $\tilde{n}(\omega)$ for a given a certain uncertainty in substrate thickness ΔL in the case of undoped silicon substrates. For other substrates and materials the results can be scaled by the relative refractive index to obtain an estimate of the expected error.

To get a sense of the uncertainty in sample thickness in common terahertz measurements consider for instance the case of silicon wafers, used widely in the semiconductor and photovoltaic industries. For commercial silicon wafers the uncertainty in the thickness of nominally 500 μm wafers typically is well in excess of several 100 nm (unpolished surface roughness and flatness over beam spot size) and can be up to 50 μm (common commercial 'spec' for 'standard' wafers). The situation (typical level of uncertainty) is not much different for many other common terahertz substrates like glass cover slips or quartz slides.

In a widely cited series of treatments Duvillaret, Garet, and Coutaz concluded that sample thickness is frequently the "main source of error in terahertz time-domain spectroscopy" [66, 71, 72]. This is also the conclusion of others [69, 70, 76]. Duvillaret *et al.* proposed strategies for reducing this error and found that by the indirect means of minimizing spurious oscillations in the calculated refractive index $\tilde{n}(\omega)$ they could infer the absolute thickness of nominally 1000 μm wafers to within ± 3 μm [66] which is similar to an approximately 1 μm resolution reported by Ralph *et al.* [77] using the same method. As will be shown below we found that one can achieve about one order of magnitude better resolution by using optimal strategies designed with

only one goal, namely determining the sample thickness as accurately as possible. The refractive index then can be extracted in a second step using the accurate *L* value obtained in the first step. This is different both in details and strategy from the method of Duvillaret *et al.* and others [66, 69] which aim to simultaneously calculate the optical constants (and smooth out spurious oscillations from of the optical parameters, n(ω) and α(ω)) and determine the exact value of *L*.

3.2 Design and Fabrication

3.2.1 Terahertz System Setup

The THz-TDS system used in this work has a conventional configuration as shown in Figure 3.1 and described elsewhere [80-82]. In brief, free space broadband terahertz pulses are generated and detected using photo-conductive antennas (PCA's). To aid the reader in translating our sensitivity results to any given system of interest we will briefly provide information on the most relevant features and characterization of our system. A Ti:Sapphire laser (Coherent Mira) with pulse width 150 fs – 200 fs, 80 MHz rep rate and average power ~ 1.3 W was used to gate two identical PCA's to generate and detect terahertz pulses. The PCA's consisted of an array of 78 interdigitated Au stripline antennae of semi-insulating GaAs (BATOP iPCA-21-05-1000-800-h). The signal from the detector was amplified directly with a Lockin amplifier (SRS 830) without pre-amplification. Figure 3.1 reminds us the detail depiction in section 1.3 and Figure 1.5 (a).

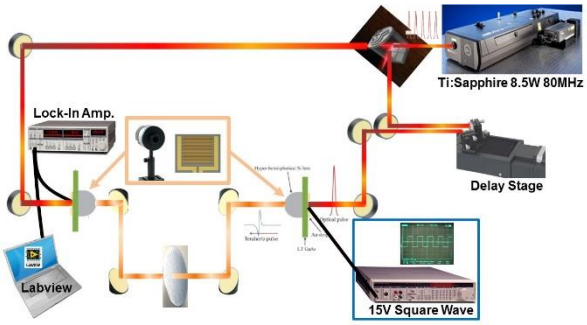

Figure 3.1 Experimental setup of the lab transmission-type THz-TDS

The dynamic range (DR) and signal to noise (SNR) of our system at the time of the measurements reported here were determined as described in Naftaly 2013 [83]. The relevant definitions are:

$$\text{SNR} = \frac{\text{mean magnitude of amplitude}}{\text{standard deviation of amplitude}}$$

$$\text{DR} = \frac{\text{maximum magnitude of amplitude}}{\text{RMS of noise floor}}$$

Meaningful comparison of SNR and DR statistics require knowledge of the number of scans averaged. The mean and standard deviation in the SNR formula for the values reported in Table 3.1 were calculated from 8 runs. Each of the 8 runs itself was the running average of data collected over 10 minutes (10 scans at a scan rate of 1 min/scans). Throughout this paper whenever the accuracy or resolution of a measurement is reported a 'measurement' refers to 1 run as defined in the previous sentence on the spectrometer described in this section.

	Time Domain	Frequency Domain
SNR	134@peak Maximum	Maximum: 288
DR	714@peak Maximum	Maximum: 2221

1) Table 3.1 SNR/DR Result of the lab THz-TDS system.

3.2.2 Silicon Sample Preparation

To determine the resolution of and compare the five different approaches for measuring wafer thickness using THz-TDS a set of wafers was fabricated with thickness $L=L_0-\delta$ with δ ranging from 0.33 μm on the low end to 14 μm on the high end and the manufacturers nominal value for L_0 being 500 μm. The samples were fabricated using the following procedure: A silicon

wafer (CZ, 475-575 μm, p-type, (100), 10-25 Ω-cm) was diced and samples were dry etched with SF_6 plasma in a LAM490 plasma etch system for different time periods and under different gas flow conditions as shown in Figure 3.2. The amount of silicon etched away was measured with a Tencor P2 profilometer. It was confirmed with an ECV analysis that the doping concentration in the wafers used was approximately 1.6×10^{14} cm^{-3} and uniform.

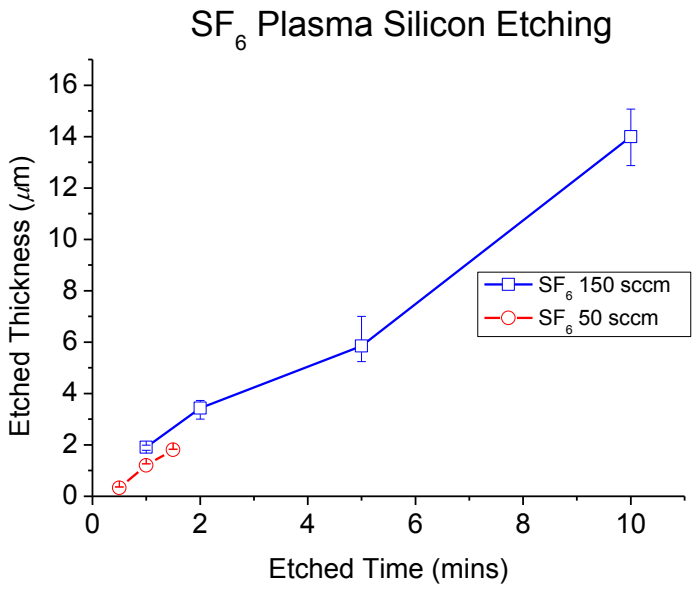

Figure 3.2 The amount of silicon etched away as a function of time

3.3 Results and Discussion

THz-TDS measurements are done by mapping out the waveform (electric field vs. time) of terahertz pulses as shown in Figure 3.3 with a spectrometer as shown in Figure 3.1. The frequency spectra (amplitude vs. frequency and phase vs. frequency) are then obtained by doing a Fourier transform of the time domain data. All THz-TDS based approaches for measuring the thickness of samples, wafers and thin films can be divided into time domain (using the directly measured data or "time domain pulses" as in Figure. 3.3) or frequency domain methods (using the data after a discrete Fourier transform (DFT)).

In the time domain one can use either the transmitted THz peak position (pulse time delay by sample) or THz peak intensities (absorption by sample) to infer sample thickness. Time delay (peak position) is the most direct and perhaps most widely cited approach for inferring thickness in the literature. We will show that peak amplitude is the least sensitive and most problematic of all the approaches considered here. A hybrid approach in which the THz waveform is sampled only at one fixed point in time is sometimes used, primarily because of its speed. We will show here that this approach can at best have the same resolution as the time delay approach but will in practice also be plagued by the problems of the amplitude approach.

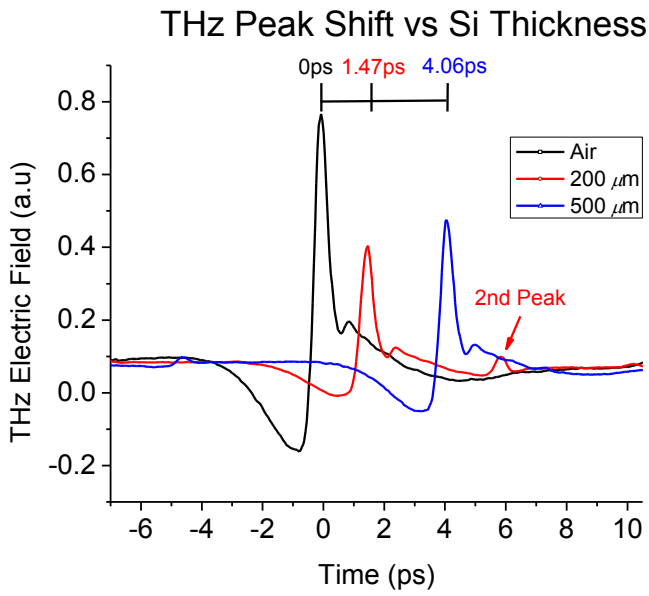

Figure 3.3 Terahertz pulses transmitted through dry air (no sample), a 200 μm Si wafer and a 500 μm Si wafer. The pulse attenuation does not scale with thickness at all since the thinner sample is more highly doped (boron, 10^{16} cm^{-3} vs. 10^{15} cm^{-3}). The relative time delay nonetheless roughly scales with sample thickness. (In Si n is much less sensitive to doping than κ).

By taking a Fourier transform of any time domain pulse, like those shown in Figure 3.3, the power spectrum of the pulse can be calculated. Shown on the inset in Figure 3.4 is a plot of the power transmission ratio of a wafer (the power spectrum of a terahertz pulse propagated through a silicon wafer divided by the power spectrum of an identical pulse when there is no

sample). We will see that there are two approaches in the frequency domain that can be used to measure the thickness of silicon wafers. Both these approaches have higher resolution than any of the time domain methods considered.

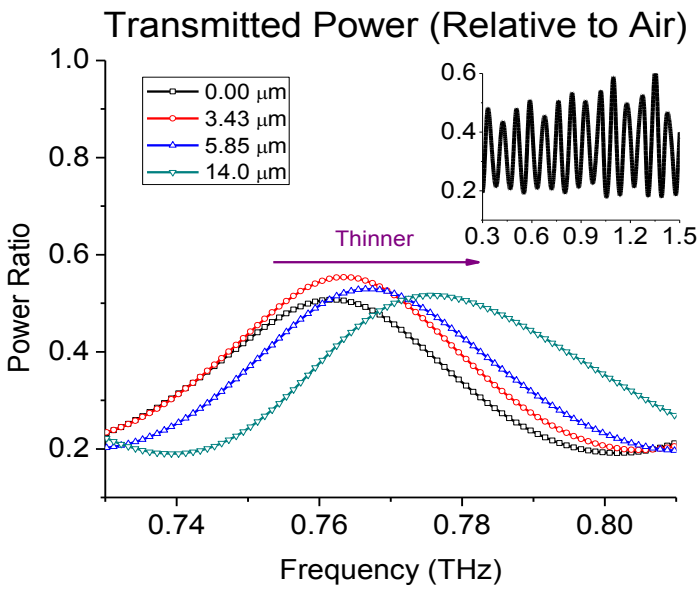

Figure 3.4 The power transmission ratio in the frequency domain under different etched amount of silicon. Thinner thicknesses move resonant peaks to the right side.

3.3.1 Time Domain Method – Peak Amplitude Change

The amplitude of a terahertz pulse will in general decrease as the pulse propagate through a medium due to dispersion and absorption. Hence, one can in principle infer the thickness of a sample by first transmitting a terahertz pulse through the sample to be measured and then transmitting an identical terahertz pulse through a sample with identical composition and with precisely known (or "reference") thickness. These measurements of sample and reference can either be done in back-to-back scans or sometimes is done by mechanically switching between inserting the sample and reference in the THz beam path at a fixed frequency (typically several Hz) and directly detecting the difference with a Lock-in amplifier [84, 85]. As can be seen in Figure 3.3 the THz pulse amplitude is both a function of sample's thickness and the sample's absorption coefficient. As a practical matter the variation in amplitude

encountered from sample to sample frequently is a stronger function of variation in factors that determine intrinsic absorption (like impurity concentrations) than it is primarily or just a function of variation in sample to sample thickness. Nonetheless, if the target application involves samples of sufficiently uniform composition (more precisely sufficiently uniform absorption in the THz region) then one can in principle determine the precise thickness of the sample by measuring the attenuation of the THz peak amplitude.

Since high resistivity silicon has a surprisingly flat (wavelength independent) refractive index over the region of the terahertz spectrum used here (0.1 – 2 THz) [49, 86] we can neglect dispersion when calculating an order of magnitude estimate of the predicted resolution of this approach applied to our test case of lightly doped Si. Neglecting dispersion and making the approximation that

$$\frac{\kappa(\omega)\omega}{c} \approx \frac{\kappa(1THz)*1THz}{c} = \frac{\alpha(1THz)}{2} \tag{3.1}$$

where κ is the imaginary refractive index and α the absorption coefficient.

With these assumptions it is straightforward to derive the following relationship between E_s (the THz electric field amplitude transmitted through an etched sample), E_r (the THz electric field amplitude transmitted through an unetched reference sample) and δ (the amount of etched silicon).

$$E_s = E_r e^{\frac{\alpha}{2}\delta} \tag{3.2}$$

By repeatedly measuring E_s and E_r for the reference sample we found that the standard deviation for a typical measurement of the ratio E_s/E_r on our system is ±0.009. Substituting this uncertainty into equation (3.2) and using a value of 7.5 cm^{-1} for α (measured at 1 THz for the 9 Ω·cm p-type silicon used here) we estimate a theoretically predicted resolution of ~24 μm for determining the thickness of lightly doped Si wafers by back-to-back peak amplitude measurements on a THz-TDS system with comparable SNR to ours. The amplitude ratio E_s/E_r

was measured for every one of the set of etched wafers described in section 3.2. The results are shown in Figure 3.5.

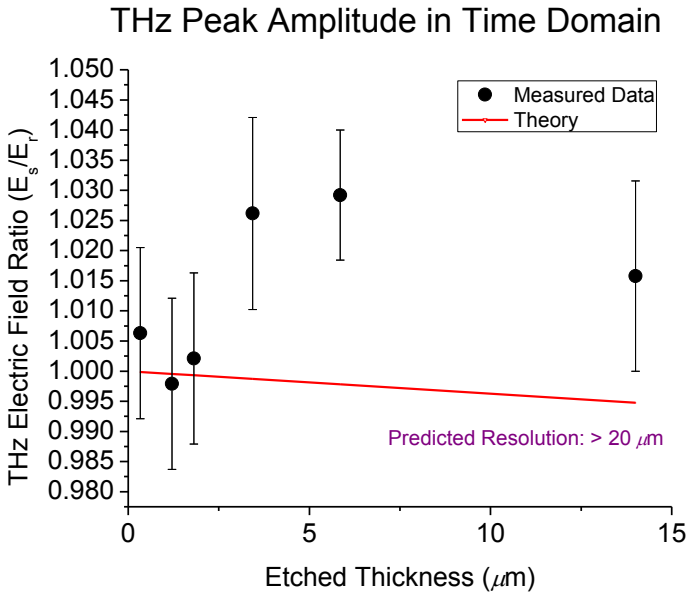

Figure 3.5 The measured THz amplitude ratio as a function of etched silicon thickness. The red line shows the trend the measurements should follow according to equation 3.2. Clearly the amplitude technique does not have the resolution necessary to measure the thickness differences of this set of wafers.

We conclude that no reliable measurement of the thickness of any wafer in our test set can be made by this method and in our measurements this method indeed has, consistent with the theoretical estimate, a resolution no better than 20 μm (for determining the exact wafer thickness of ~ 500 μm lightly doped Si or the thickness of comparable materials on comparable systems). Conversely, if the time domain peak amplitude is the THz-TDS index used in THz based measurement then this quantity is not sensitive to uncertainty or variation in wafer thickness up to at least ±14 μm.

3.3.2 Time Domain Method – Peak Position Shift

The time delay of a pulse propagating through a sample can be determined directly from THz-TDS as shown in Figure 3.3. This approach, inferring sample thickness from pulse delay, is perhaps the

most direct and frequently suggested THz-TDS based approach for thickness measurement in the literature. It was first suggested by Mittleman *et al.* [87, 88] that the time delay in the arrival of terahertz pulses reflected from different interfaces can be used as a means to do 3D tomography. Subsequently this concept has been used to develop metrology that can detect paint thickness [89], coating thickness of tablets and capsules [90-94], silicon wafer thickness [95] and is also the basis for detecting hidden or buried layers in paintings (artwork) [96] Recently Hussain et al. [70, 97] introduced a modification of this approach where they measured the change and peak delay between when the sample is at normal incidence and tilted by 45°.

We will not consider in this study the case where the total thickness of the sample is so thin that it approaches the spectrometer detection threshold or SNR limit; for low absorbing samples this is typically ~10 μm [78, 98]. Instead our focus is on the absolute resolution with which one can measure the exact thickness of thicker samples. However we mention that Theuer *et al.* [78, 98] recently proposed a waveguide based approach that uses pulse delay of a terahertz pulse propagating through a waveguide coated with the sample that have a demonstrated detection threshold of 2.5 μm (Mylar films) and predicted submicron capability. It can be seen in Figure 3.3 (see also [66, 69]) that in every sample scan there is a primary pulse followed by a second pulse and potentially a third and fourth etc. The primary pulse is from THz light that propagated once through the sample (path length L), the second pulse is once internally reflected (path length $3L$), the third pulse is twice internally reflected (path length $5L$) etc. In principle one can use the delay of any of these pulses to determine the sample thickness. The internally reflected pulses experience more delay, which would increase the theoretical resolution obtainable by them (see equation 3.3). However there is a trade-off given the fact that every successive pulse is smaller and significantly more attenuated (due to losses at each reflection and

sample dispersion & absorption) than the previous pulse. A smaller pulse amplitude translates into more uncertainty in peak position, until the n'th pulse eventually becomes undetectably small (with n depending on system DR, sample reflectivity, dispersion and absorption). Here we will calculate and compare the theoretical and experimentally obtained resolution when using either the 1st or the 2nd pulse.

It is straightforward to derive equation 3.3 when neglecting dispersion. The primary pulse transmitted through a sample with extra thickness δ will experience extra delay Δt given by:

$$\delta = \frac{c\Delta t}{n-1} \tag{3.3}$$

and for the k'th pulse the left hand side of equation 3.3 needs to be replaced by $(2k-1)\delta$.

The standard deviation for a typical measurement of the primary peak position for ~500 μm lightly doped Si wafers on our system is 0.0213 ps and for the once internally reflected peak is 0.0772 ps. Substituting these values into the appropriate versions of equation 3.3 and using a value of 3.42 for n (measured at 1 THz) we estimate theoretically predicted resolutions of 2.6 μm (1st peak) and 2.9 μm (2nd peak) for determining the thickness of lightly doped Si wafers by peak position measurements on a THz-TDS system with comparable SNR and DR to ours. The measured THz pulse peak delay for all samples in our test set is shown in Figure 3.6. The experimentally observed resolutions are remarkably consistent with the simple theoretical estimates. Using the primary peak resulted in wafer thickness measurement accurate to within 0.43% ($\pm$ 2.25 μm for a 510 μm wafer). Measurements using the second peak had almost exactly the same accuracy.

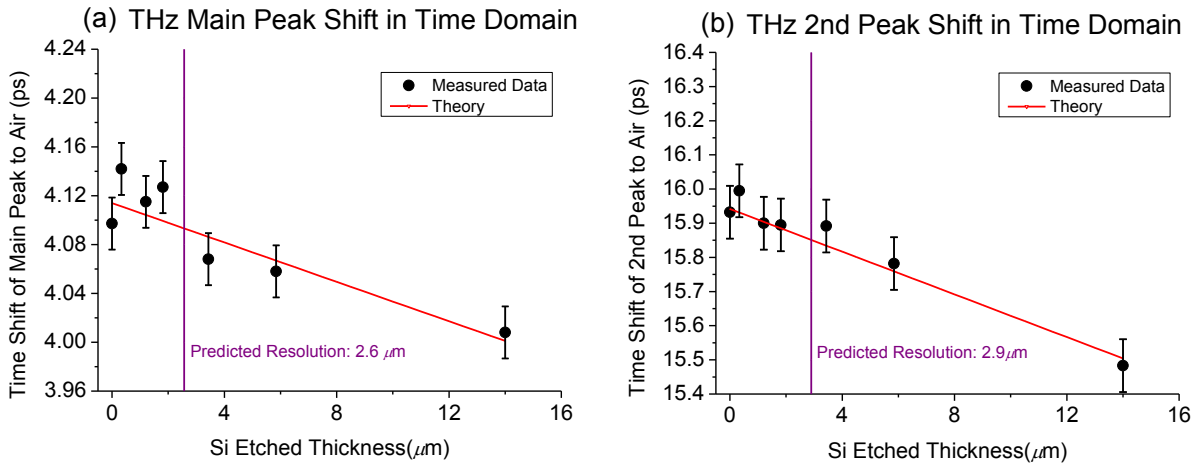

Figure 3.6 (a) The measured main THz peak delay relative to a scan with no wafer (in picoseconds), as a function of etched silicon thickness. (b) The 2nd THz pulse peak location shift in time domain as a function of etched silicon thickness. The red lines are the theoretical approximations to the relationship between sample thickness and peak position calculated using equation 3.3 with L_0 = 510 μm and n = 3.42 in both a & b.

We conclude that the most widely used approach for determining thickness in THz-TDS, namely tracking peak delay, can be used to measure the thickness of ~ 500 μm lightly doped Si wafers to within ± 2.25 μm. (This value is comparable to the reported resolution of this approach for paint thickness measurement of ± 4 μm [89]. Resolution for pharmaceutical tablet coatings is harder to determine due to the local variation in the effective coating refractive index and complexity of the tablet shape but tend to be roughly in the 10 μm or greater range. Hussain *et al.* [70, 97] also estimate the resolution of their approach as being roughly, or at least, 10 μm based on comparison with simple micrometer measurements that themselves have only about 10 μm accuracy.) Conversely, any random variation or uncertainty in wafer thickness greater or equal to 1 to 2 μm will introduce a measurable deviation in THz peak position and any THz metrology or derived quantities that depend on the accuracy of peak position would incur a corresponding bias or error.

3.3.3 Time Domain Method – Hybrid Analysis

We showed in section 3.3.1 that merely tracking the attenuation of the THz peak amplitude has very poor resolution. However, an approach used sometimes (e.g. [99]) because of its measurement speed is to combine the attenuation approach of 3.3.1 and the peak shift approach of 3.3.2 into a single methodology illustrated in Figure 3.7. As can be seen in Figure 3.7, and also inferred from our analysis in sections 3.3.1 and 3.3.2, the change in time delay (shift of the peaks) with thickness is much larger than the change in peak amplitude (this will in general be true for any material that does not highly absorb THz, that is most materials on which transmission THz-TDS is a useful technique). Hence, we see that for any material with moderate to low THz absorption this method is essentially still a measurement of the phase shift. However, instead of measuring the peak position exactly (by mapping out the whole terahertz pulse in time and then determining where the exact peak position is) this approach only samples a single fixed point in time as is illustrated in Figure 3.7. (Typically the sampling point is chosen as the peak position of a reference sample with either exactly known thickness or a desired thickness albeit unknown). When the reference sample is replaced with a sample with a different thickness the peak arrival time will shift, and hence the amplitude at the sampling time will change. The main advantage of this approach is that sampling just a single point in the time domain is much faster than mapping out (scanning across) the whole time domain pulse. For industrial metrology speed of acquisition is often a very important consideration. The main disadvantage of this approach is clearly illustrated in Figure 3.3, that is the amplitude is much more sensitive to sample absorption (and hence impurities or compositional variation) than to thickness. Since the hybrid approach measures both delay and amplitude changes with no way of decoupling these it will always be susceptible to inaccuracy in thickness determination whenever there variation in purity and composition (in any factor that impacts THz absorption).

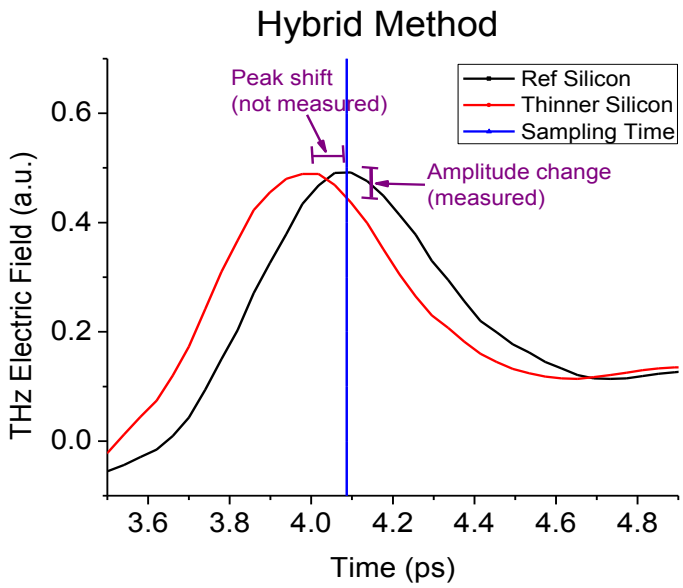

Figure 3.7 A closer look at the transmitted THz pulse peaks for a reference wafer scan and a scan of a slightly thinned wafer. In the hybrid method the signal is sampled at a fixed the sampling time (the blue line which is here chosen as the peak of the reference pulse.) Note that the leftward peak shift (earlier arrival time) of the slightly thinned sample results in a reduced signal at the sampling time. The hybrid method attempts to deduce sample thickness from the reduction in signal at the sampling time alone (i.e. the rest of the pulse waveform is not measured). Note that a sample thicker than the reference would result in a rightward shift and also a reduction in signal at the sampling time. Hence, in practical applications one needs to use a reference sample that is a priori known to be either thicker or thinner than all the samples to be measured or the sampling time should be offset from the reference peak.

The THz peak shift has been introduced in section 3.3.2 and the THz amplitude change for small shifts can be approximated by fitting any suitable function to the peak (in here we use a Gaussian fit). With these assumptions the change in THz amplitude at the sampling time (ΔE) is related to the difference between sample and reference thickness (δ) by:

$$\Delta E = A\left(1 - e^{-\beta\left(\frac{n-1}{c}\delta\right)^2}\right) \tag{3.4}$$

where A and β is the Gaussian fit parameters. (A will be the reference peak amplitude and β is related to full width at half maximum (FWHM) of the peak).

As can be seen in Figure 3.8 for all samples thinned by less than 14 μm the measurement standard deviation is such that for some measurements the quantity $\Delta E = E_{ref} - E_{sam}$ is measured to be less than zero in violation of equation 3.4 – this means a failure of the measurement and that the etched amount is less than the resolution of the measurement approach. (The noise in the amplitude is larger than change in the amplitude due to the peak shift due to the thickness change.) By looking at the recorded peak shapes in Figure 3.7 one can see why the hybrid approach does not scale linearly with thickness. For small thickness differences/peak shifts the peak profile is relatively flat and hence the method is relatively insensitive. For somewhat larger differences the technique becomes relatively more sensitive. For our test set only the 14 μm etched sample falls in the range where we never obtain measurements that 'fail' (i.e. $\Delta E > 0$ for all measurements).

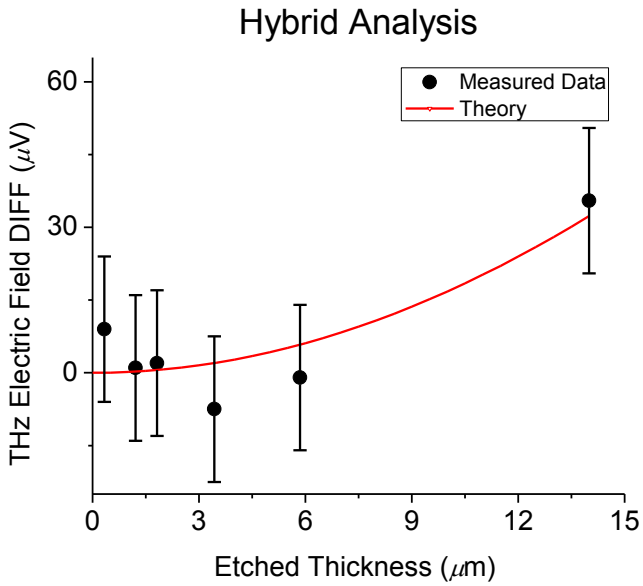

Figure 3.8 The THz electric field of a pulse transmitted through the reference wafer minus the THz electric field of a pulse transmitted through the sample (etched wafers) with both fields measured at a fixed sampling time (the sampling time was chosen to be the reference sample peak position). The reference sample is the unetched Si wafer and the samples are thinned by the number micrometers indicated on the x-axis. The parameters used in the theoretical prediction of what a perfectly noise free measurement should look, like according to equation 3.4, is $\beta = 5.5 \cdot 10^{24}$ and A = 1.303 mV and n = 3.42.

Hence we conclude that it is impossible to reliably distinguish thickness differences when the difference between the sample and the ~ 500 μm reference is smaller than ~ 10 μm. An accuracy/resolution of ± 3.5 μm was estimated when measuring the thickness of wafers that differ by at least 10 μm from the reference. (This reported resolution is only valid close to our case where the thickness difference was 14 μm. Because of the built-in non-linearity of equation 3.4 the resolution of this approach will vary significantly as δ, that is the relative sample to reference thickness, vary.) The hybrid approach has relatively low resolution for thickness measurement and is very susceptible to significant inaccuracy given any variation in sample composition. We therefore only recommend this approach for crude measurements where measurement speed is of primary importance.

3.3.4 Frequency Domain Method – Fabry-Pérot Cavity Resonances

It is clear from the inset in Figure 3.4 that the ~ 500 μm wafer act as a Fabry-Pérot cavity for THz light (λ ~ 150 μm to 1.6 mm) [68, 69, 79]. We will see below that the resonant peaks of this cavity can be used as a very sensitive gauge of the cavity length (sample thickness). Realizing this Withayachumnankul *et al.* [100] suggested using sample Fabry-Pérot fringes to determine sample thickness and noted that the accuracy of the method "needs further study", which is in part what we will do below. In two more recent reports Naftaly *et al.* [74, 83] show that given a high resistivity Si wafer or high quality GaAs wafer with "exactly" known thickness one can use a comparison of the measured Fabry-Pérot resonant peak frequencies of this sample with the theoretically predicted frequencies (using equation 3.5 below) to verify the 'frequency calibration' or accuracy of the spectrometer used. This is an alternative to a more standard approach like comparing the absorption frequencies of a gas (like CO) measured with a given spectrometer to their known positions [74]. Naftaly et al. [74, 83] shows that the conventional

gas absorption line approach and their novel wafer resonance based approach provide approximately equally accurate standards for frequency calibration. Simply put, Nafatly's work show that given an ideal homogenous calibration wafer with exactly known thickness and (non-dispersive) refractive index one can predict the exact frequencies of the Fabry-Pérot resonances: The approach we present in this section is closely related to that of Naftaly since it simply asks the inverse question: With what resolution can the sample thickness of an unknown sample be inferred given a typical THz-TDS spectrometer measurement of the Fabry-Pérot peak positions? We show below how the practically achievable resolution of this technique can be improved by introducing an optimal method for combining the measurements of all the etalon peaks in the spectrometer bandwidth and correlating this data to sample thickness.

It can be seen in the inset in Figure 3.4 that we have (for lightly doped ~ 500 μm) 14 resonant peaks that fall in the frequency range 0.3 – 1.5 THz. If, as before, we neglect dispersion (assume n independent of frequency) it is easy to derive that the frequencies of the resonant peaks will be given by

$$\nu_j = j\frac{\mathrm{c}}{\mathrm{n2L}}, \quad \text{for} \quad j = 1,2,3 \ldots \tag{3.5}$$

This formula accurately predicts all the peak positions in wafer power ratios like those in Figure 3.4. The equation also predicts that the first 3 resonant peaks for lightly doped ~ 500 μm wafers as used here will be below 0.3 THz and hence are to the left of the spectrum seen in Figure 3.4. Peaks 4 to 17 fall within our spectral range. From (3.5) if follows that if the wafer thickness is changed by a distance δ then then resonant frequency will shift by:

$$\Delta\nu_j = j\frac{c}{2n}\left(\frac{1}{L'} - \frac{1}{L}\right) = j\frac{\mathrm{c}}{2\mathrm{n}}\left(\frac{1}{\mathrm{L_0}\text{-}\delta} - \frac{1}{\mathrm{L_0}}\right) \approx j\frac{\mathrm{c}}{2\mathrm{nL_0^2}}\delta \tag{3.6}$$

One can also calculate that the change in spacing in between adjacent resonant peaks with a change in wafer thickness will be given by:

$$\nu'_{j+1} - \nu'_j = \left(\nu'_{j+1} - \nu_{j+1}\right) - \left(\nu'_j - \nu_j\right) = \Delta\nu_{j+1} - \Delta\nu_j = \frac{c}{2n}\left(\frac{1}{\mathrm{L_0\text{-}\delta}} - \frac{1}{L}\right)$$

Hence, $$\nu'_{j+1} - \nu'_j = \frac{\Delta\nu_j}{j} = \frac{c}{2n}\left(\frac{1}{L_0 - \delta} - \frac{1}{L_0}\right) \approx \frac{\mathrm{c}}{2\mathrm{nL}_0^2}\delta \qquad (3.7)$$

Note that equation 3.6 (peak position) depends on the resonant peak number k so that higher frequency peaks shift more than lower frequency peaks with a change in thickness. This means that when using the *absolute position* of resonant peaks to infer thickness higher frequencies should give higher resolution. However, the spacing between peaks is independent of *j*. Hence if one uses equation 3.7 to infer thickness lower frequencies are in principle equally sensitive than higher frequencies. One can base a metrology for wafer thickness measurement either on equation 3.6 (absolute Fabry-Pérot peak position) or 3.7 (spacing between Fabry-Pérot peaks). In theory using "absolute Fabry-Pérot peak position" should do better at higher frequencies and using the "spacing between Fabry-Pérot peaks" should do better at low frequencies. We have tried both approaches here and found the Fabry-Pérot peak position (eqn. 3.6) to give uniformly superior results in our experiments and will only discuss this case in more detail here. Instead of just looking at any one of the 14 peaks in our spectral range we will present here an approach that incorporate data from all 14. This approach resulted in the highest resolution method for measuring wafer thickness presented in this section.

The standard deviation in the measurement of a Fabry-Pérot peak position during a run (see section 3.2) was determined and used for $\Delta\nu_j$ in equation 3.6 to estimate that the theoretically predicted resolution on our system for determining wafer thickness by this approach will be between 200 nm to 960 nm. (We only used peaks in the window from 0.3 to 1,5 THz where our SNR is maximum – note that both the DR and SNR of THz-TDS measurements are very frequency dependent [101].) What specific resolution within this range a particular measurement will have depends on the value for j that is used, i.e. the higher the frequency of the etalon peak used the higher the theoretical resolution of the method will be.

Naturally THz-TDS systems that use ultra-short pulses and hence have bandwidth up to 5 THz can have a maximum theoretical resolution in the ~ 50 nm range provided *n* remains frequency independent for $\nu > 2$ THz, which is the case up to about 4.5 THz provided the resistivity of the silicon is very high (~ 1 kΩ or larger) [102]. For wafers with more typical lower resistivity's sub 100 nm resolution will require the development of an implementation of this approach that takes the variation of n with frequency into account.

The peak shifts for all 14 resonant peaks in our high SNR range was measured for all 6 etched samples (peak shifts is given relative to the un-ethced sample) and is shown in Figure 3.9 (a). Although one can base a thickness metrology on any one of the peak shifts ($\Delta\nu$ at a fixed *j* value) we obtained our best results by taking them all into account. We found the most precise approach to be to fit a best fit line to all the peak shifts of a given sample. (Note, the lines in Figure 3.9 (a) are not empirical best fit lines but are the theoretically predicted outcome according to equation 3.6) Figure 3.9 (b) shows a plot of the slopes of empirical best fit lines to the data of every sample in Figure 3.9 (a) plotted versus the etched amount of that sample. The red line shows the expected shape of this line according to equation 3.6.

In summary, the absolute (or relative) thickness of silicon wafers can be measured with the following methodology:

1) Measure all the Fabry-Pérot peak positions of a reference wafer with known (or desired thickness) within the high SNR bandwidth range of the spectrometer.

2) Measure all the Fabry-Pérot peak positions of the sample.

3) Calculate the frequency shift of all peaks.

4) Fit a best fit line to a plot of the peak shifts for a given sample vs. the peak numbers.

5) Read the wafer thickness from a calibration curve (like Figure 3.9 (b)) that relates the slope ($\Delta\upsilon_j/j$) of the plot in step 4 to the relative difference in thickness (δ).

For our calibration curve we used the theoretical equation 3.6 (red line in Figure 3.9 (b)) and obtained average resolution on a typical run of ±0.26 μm or an accuracy 0.05 % for determining the exact wafer thickness of ~ 500 μm wafers. These results are close to the limits of the flatness and roughness of our wafers and the resolution of the profilometer (variation ~ 100 to 200 nm within the THz spot size). In principle one could probably do even better by generating and using an empirical calibration curve in step 5 provided one has a set of highly polished wafers with precisely known thicknesses.

Since the Fabry-Pérot peak position is not just inversely proportional to the thickness *L* but also inversely proportional to the refractive index n (see equation 3.5) any sample to sample variance in *n*, or lack of a precise knowledge of the sample n, would introduce additional variance and uncertainty into this method for thickness determination and thus reduce its reliability and resolution. Equation 3.6 show that small deviation in thickness δ between a reference wafer and a sample wafer can be detected accurately even if the value of *n* is not known accurately as long as *n* do not vary from sample to sample. Note that equation 3.6 (and 3.7) show that the thinner the sample the more sensitive the method of section 3.3.4 will be. I.e. the shift in peak frequency that result from a given change, or deviation, in sample thickness is proportional to $1/nL_0^2$. (This increased sensitivity is slightly counter-acted when using the approach proposed here that utilizes all the etalon peaks by the fact that thinner samples will have a smaller number of Fabry-Pérot peaks within the spectrometer bandwidth – i.e. thinner samples haves fewer peaks with wider peak to peak spacing.) This trend of more sensitivity with decreased sample thickness naturally cannot hold indefinitely. For any given material *n* and

available THz bandwidth there will be a sample thickness below which there will be no etalon peaks within the measurable terahertz range. In addition to this limit Withayachumnankul *et al.* [103] recently showed that there is a definite lower limit below which THz-TDS cannot reliably detect even the presence of very thin samples and that this critical minimum thickness can be different for phase and amplitude. For amplitude detection (Fabry-Pérot fringes is a feature within the amplitude spectrum) in undoped silicon this critical minimum thickness is found to be > 2 μm. Therefore, for any given material there exists a minimum absolute thickness below which the method of this section cannot be applied. This minimum thickness is typically much larger (~10 μm) than the resolution with which thickness can be determined.

In conclusion, any silicon wafer presents a natural Fabry-Pérot cavity for THz light (with one or more peaks within a 2 THz window thickness for any wafer > 24 μm). The position of the etalon peaks can be used as a very accurate gauge of sample thickness. An optimal method for extracting thickness by measuring the shift in etalon resonances was demonstrated that can have up to ~ 100 nm resolution or better (depending on the spectrometer SNR and bandwidth). Conversely, any terahertz measurement of a quantity (for example $n(\omega)$ or $\sigma(\omega)$) that uses the frequency domain data will be susceptible to error or variation in wafer thickness. The results and framework presented here can be used quantify how sensitive a given measurement is to uncertainty and variation in sample thickness.

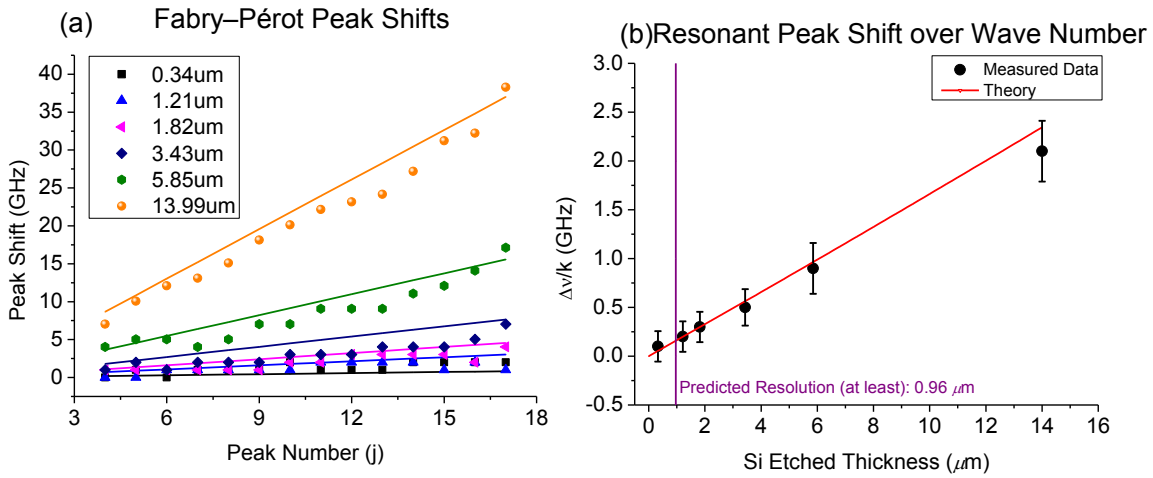

Figure 3.9 (a) The measured resonant frequency shift for every one of the resonant peaks in the window from 0.3 to 1.5 THz (labeled k = 4, 5,…,17). All peaks were measured for all wafers. The legend shows the amount of silicon etched (δ) for a given wafer. The lines is plots of equation 3.6 using L_0 = 518 μm and n = 3.42 for all wafers and for δ the profilometer measured quantity as shown in the legend. (b) The slope of best fit lines to the data in 3.9a plotted against the amount of silicon etched. The red line is the theoretically predicted variation of this quantity as predicted by equation 3.7 with L_0 = 518 μm and n = 3.42.

3.3.5 Frequency Domain Method – Phase Angle Shift

When taking the Fourier transform of the time domain peaks as in Figure 3.3 the Fourier coefficient for any give frequency is a complex number. The square of the modulus of these Fourier coefficients gives the power spectrum as shown in Figure 3.4 and used in the previous section to determine wafer thickness (via Fabry-Pérot peak position). The phase of these Fourier coefficients is the phase delay of the given frequency. Withayachumnankul *et al.* [103] recently showed that one can in many cases detect the presence of very thin films more sensitively by tracking the THz-TDS measured phase rather than the amplitude. (They found a minimum detectable thickness for photoresist films ~ 2 μm when using phase, which translate to ~1 μm for undoped silicon since $n_{Si} \approx 2n_{PR}$). We propose here that this phase delay too can be used to infer wafer thickness. As with the resonant peak position one could in principle use just the phase delay at one arbitrarily chosen frequency. However we found that as in section 3.3.4 one can do much better (in terms

of repeatability and resolution) by an approach that combine data form all frequencies at which the spectrometer used has reasonably low SNR.

The phase of a terahertz wave with frequency ν propagated through a Si wafer minus the phase of the same frequency propagated the same distance (L) through air will give a relative phase delay:

$$\Delta\emptyset_{\text{air}}=\emptyset'-\emptyset=2\pi\nu\frac{(\text{n-1})}{\text{c}}(L_0-\delta)=\text{slope}\cdot \tag{3.8}$$

with $\text{slope}=2\pi\frac{(n-1)}{c}(L_0-\delta)$ for the case of a wafer originally of thickness L_0 with δ etched away.

Now, for the special case of no dispersion ($n(\nu)$ constant) a plot of $\Delta\emptyset_{\text{air}}$ vs. ν will give a line with constant slope given by the formula 3.8. We already noted that undoped Si has a remarkably flat refractive index in the THz region (below 2 THz) and so it is no surprise that the measured phase delay vs frequency plotted in Figure 3.10 is very close to perfectly linear. The plots in Figure 3.10 were obtained by taking the Fourier transform of just the main peak in Figure 3.3 (i.e. by truncating the time domain data before the second peak). One can also take the Fourier transform of just the second once internally reflected peak in Figure 3.3. A plot of the phase of this transform also is close to linear with the relationship between phase delay and frequency for the peak given by:

$$\Delta\emptyset_{air}=\emptyset'-\emptyset=2\pi\nu\frac{(3n-1)}{c}L=2\pi\nu\frac{(3n-1)}{c}(L_0-\delta) \tag{3.9}$$

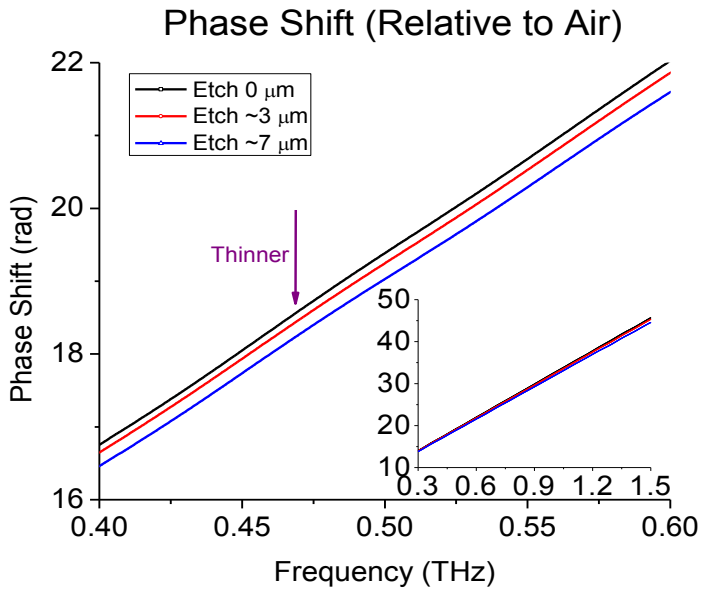

Figure 3.10 The phase delay as a function of frequency for terahertz pulses transmitted through wafers with different thickness relative to an identical pulse transmitted through air.

By measuring the standard deviation (between runs as defined in section 3.2) in the relative phase delay ($\Delta\emptyset_{air}$), and using this uncertainty in equations 3.8 and 3.9 respectively we theoretically predict the resolution of the phase delay approach for measuring sample thickness (δ) as ± 0.94 μm when using the phase delay of the main peak and ± 1.17 μm when using the phase delay of the second (once internally reflected) peak. The phase delay for all frequencies of all etched samples was measured several times (three representative examples are shown in Figure 3.10). The slope of $\Delta\emptyset_{air}$ vs. ν was calculated for every run and the resultant data is plotted in Figure 3.11. By using equations 3.8 and 3.9 to plot δ vs. the slope ($\Delta\phi/\nu$) one can also plot the theoretically predicted shape of these plots (shown in red). We note that the red curves with the correct value (as determined in section 3.3.4) of 518 μm for the unetched wafer (L_0) gives a reasonable but not perfect approximation to the measured data. We hypothesize that the deviation between the theoretical (red) and an empirical calibration (dashed black) line seen in Figure 3.11 (a) could be due to 1) the fact that $n(\nu)$ is not perfectly constant with frequency and/or 2) the error introduced by truncating the time domain data to isolate the first peak. The data in Figure 3.11 (b) have

the same two potential sources of deviation from ideal theory, namely 1) $n(\nu)$ not constant and 2) some information from the first peak overlapping with the second peak and hence being included in the second peak data while the model is for an ideal situation where we can perfectly isolate only once internally reflected data. Because of these sources of deviation between the ideal optical model and measured data we recommend using an empirical calibration curve (dashed black) line instead of the theoretical lines (red). When using the empirical calibration line (in Figure 3.11 (a)) to estimate the wafer thickness the experimentally determined resolution of this method in a typical run is ± 0.87 μm or 0.17 % for telling the exact thickness of an ~ 500 μm wafer.

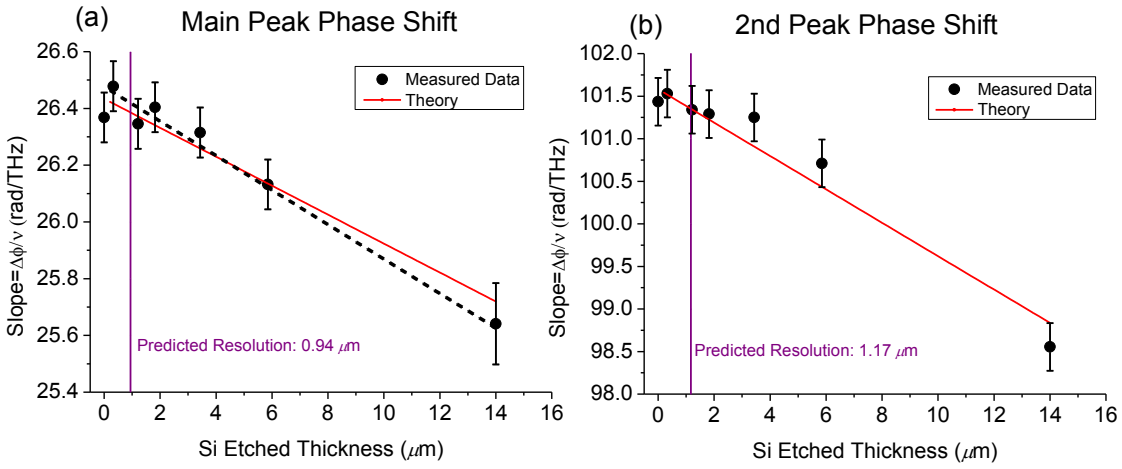

Figure 3.11 (a) A plot of the slope of phase delay over frequency (y-axis) for the main time domain peak at various relative wafer thicknesses (x-axis). (The time domain data was truncated at 12ps after the air reference scan peak prior to the Fourier transform). (b) A plot of the slope of phase delay over frequency for the second time domain peak vs. various wafer thicknesses. (Only the time domain data containing the 2nd peak, from 12ps to 20 ps, was transformed). The theoretical plots was made using equations 3.8 & 3.9 respectively with L_0 = 518 μm and n = 3.44 & 3.46 respectively.

In conclusion, the resolution obtained by tracking phase delay as a function of frequency is almost as high as the resolution for measuring wafer thickness obtained by tracking the Fabry-Pérot interference peaks. However, an empirical calibration curve as opposed to a theoretical curve is recommended. From the THz-TDS spectroscopy point of view any random wafer thickness variation more than 0.17 % from the value used in the "data work-up" will result in a

measurable bias on the phase delay and hence introduce a related error in any quantity calculated based on the incorrect thickness (that could be for instance the manufacturer specified wafer thickness).

3.4 Conclusions

Accurate knowledge of sample thickness is necessary to accurately measure optical material parameters with THz-TDS. Fortunately THz-TDS data typically also contain information on the sample thickness. In the work-up of THz-TDS data this information is often not used or accessed only by an indirect method – varying the value for sample thickness L used in the data work-up so as to maximize the 'smoothness' of the data. In this work we evaluated and compared various direct means for accessing the thickness information in THz-TDS data. We determined the most accurate approaches and quantitatively determined the resolution of every approach for the case of lightly doped ~ 500 μm silicon wafers. The main results are summarized in Table 3.2.

We found that the "Fabry-Pérot peak position" and "phase angle delay" approaches provide the highest resolution thickness measurements for the test case ~ 500 μm silicon wafers. Conversely, any deviation of more than ~ 0.17 % in sample thickness will introduce measurable changes in these aspects of THz-TDS measurements. We found that several simple optical equations fit the observed data remarkably well in the case of lightly doped (1.6×10^{14} cm^{-3}) silicon. Equivalent thickness measurements can be done on more highly doped wafers but calibration curves that take the dispersion into account will have to be developed. The peak frequency shift of Fabry-Pérot cavity resonances is then used in the modeling process of the entire research.

Technique	Resolution	
	Thickness (μm)	% Accuracy
Time Domain		
Peak Amplitude	> 20	> 3.8
Peak Delay	±2.25	0.43
Hybrid Analysis	> 10	> 1.9
Frequency Domain		
Resonant Peak	±0.26	0.05
Phase Delay	±0.87	0.17

2) Table 3.2 The resolution comparison of all experimental methods.

4 RECOGNITION OF PHOSPHORUS AND BORON DOPING PROFILES IN SILICON USING TERHAERTZ TIME DOMAIN SPECTROSCOPY

From previous chapter, the frequency shift of Fabry-Pérot resonances is decided to determine the bulk wafer thickness in the transfer matrix due to its sub-micron resolution. Prior to the final goal: doping profile prediction, the capability of doping profile recognition using THz-TDS needs to be studied. In this chapter, various boron / phosphorus doping profiles are designed to attest the concept with the resolution benchmark to the THz measurement uncertainty. The potential application is the *in-situ* ion implantation and diffusion process monitor. Below content has been published by "*Terahertz Science and Technology, IEEE Transactions on*" in 2014.

4.1 Introduction

As we mentioned before, U.S. PVMC embarked on a campaign with 38 separate organizations from industry, national labs and academia to identify and prioritize the critical challenges in c-Si metrology [104]. Like several similar panels and workshops this effort identified, among other challenges, the unmet need for: "High-throughput evaluation of the emitter doping process (e.g. doping uniformity, in-line resistivity, junction depth, measuring doping profile on a textured surface" [104]. Industry primarily uses SIMS and sometimes ECV measurements to determine or estimate doping profiles [27]. Both these techniques are destructive and slow. SIMS is expensive and rarely available near manufacturing. As a result samples typically need to be sent away for analysis and results are received at best within days.

Rapid progress in ultrafast fiber laser technology in recent years enabled the emergence of several robust commercial terahertz metrology systems suitable for use in a manufacturing environment. A THz-TDS based technique that can monitor doping profiles will be non-contact, non-destructive and much cheaper than SIMS. Moreover this technique can be real time or close to it (for instance inline when tracking only a simple index or measurement time < 10 min for a full detailed high resolution doping profile mapping).

THz-TDS can accurately and rapidly measure the attenuation and phase delay for every frequency in the pulse bandwidth of the terahertz pulses generated and detected (by taking the digital fourier transform (DFT) of the pulse waveform). Over the last few decades this technique has been developed, refined and used mostly in the laboratory for scientific research [40-42, 105-107]. The scientific community used it to track the dynamics of electrons in nanomaterials on sub-picosecond timescales [105, 108, 109], to reveal the fundamental behavior of electrons and holes [110] and to unlock the science of new materials like graphene [111, 112] or superconductors [113, 114]. In all these applications the sample either has to be, or is, modeled as being a uniform film or a film having at most two or three uniform layers. Terahertz imaging is a new and evolving area with scientific and industrial applications [5, 88, 115-121]. As in the scientific work most THz imaging to date map only 2D profiles of uniform materials, or of multilayer materials with at most a few uniform layers on the order of > 10 μm [18, 87, 88, 90-92, 120, 122-125]. Here we propose to extend the use of terahertz spectroscopy to monitor continuously varying depth profiles as opposed to merely monitoring the thickness of one or more uniform layers. The new application we will demonstrate here is the ability to monitor the emitter profile in photovoltaic (PV) cells – both the shape and dosage. By monitor we mean the ability to “recognize” whether profiles in a manufacturing process conform to a known desired

profile and alternatively detect when a deviation occurs. In the PV application domain the THz technique has to date been used to characterize contact defects & cracks [126], mapping areas rich in bulk defects (recombination sites) [127] and roughly mapping doping dosages (ignoring profile differences) [119, 126].

4.2 Research Background

Why is a THz-TDS based approach a good candidate technology for doping profile mapping and/or monitoring and why consider this approach now? The answer is two-fold, recent technological developments and fundamental scientific considerations (semiconductor physics).

4.2.1 Development Progress of THz-TDS

Modern THz-TDS techniques for generating broadband picosecond pulses that can be used as powerful probes originated already in the 1970's with the work of David Austin and co-workers at Bell Labs on designing the world's fastest electro-optic switches and generating ultra-short electrical pulses [40, 128]. These discoveries led to methods for generating and detecting terahertz laser pulses propagating through free space that found wide application in experimental laboratory science [128]. Terahertz spectroscopy is in particular well suited for studying the physics of free carriers in semiconductors and charge transfer dynamics [42, 88, 90, 105, 106, 109-111, 113, 115, 119, 129]. However, the advent of high power robust fiber lasers (enabling affordable robust implementations of THz-TDS) in recent years means that this technique can now also find application outside of the lab including applications in manufacturing and in-line sensing.

4.2.2 Semiconductor Physics with THz Light

In the UV-Vis, NIR and MIR spectral regions of the EM spectrum free carrier absorption

in doped Si is either negligibly weak and/or obscured by other optical features like impurity absorption, phonons or inter-band absorption [38, 61, 102, 130-133]. This leaves only the terahertz and microwave regions as candidates for clear unambiguous optical probes of free carrier properties (density, mobility and as proposed here also doping profiles) in materials like doped silicon. The microwave region, although suitable, has much less dispersion (different velocity/phase shift and absorption of different frequencies) compared to the terahertz region and relatively less contrast between doped and un-doped samples. These fundamental facts about the optical physics of doped silicon renders terahertz light the optimal probe for directly & non-destructively determining the free carrier distribution throughout a junction in doped silicon.

4.3 Experimental Results

The same lab setup THz-TDS, shown in Figure 3.1 and Figure 1.5, is utilized in the research of this chapter. Figure 4.1 shows the electric field of a typical THz pulse that is generated by the THz emitter. Also shown are pulses that were propagated through a commercial PV solar cell wafer (180 μm thick, ~ 10^{16} cm^{-3} p-type substrate with n-type emitter) and a standard IC (507 μm thick, ~10^{15} cm^{-3} p-type substrate with n-type emitter) wafer. Note that transmission through the wafer induces a delay of several picoseconds of the peak arrival time and a change in peak amplitude. The magnitude of the peak delay is determined jointly by the wafer thickness and the refractive index (propagation speed of light in the wafer). In the terahertz region of the EM spectrum the refractive index is almost completely a function of the free carrier density and mobility (and hence the wafer quality and doping). The magnitude of the peak amplitude is likewise determined jointly by the wafer thickness and the absorption coefficient (~ imaginary part of the refractive index) with absorption being the dominant effect. As with the phase shift (delay), absorption in the terahertz region is almost solely free carrier absorption and

hence the amount of absorption as a function of frequency is a very sensitive probe of doping density, and as we will show here also doping profiles.

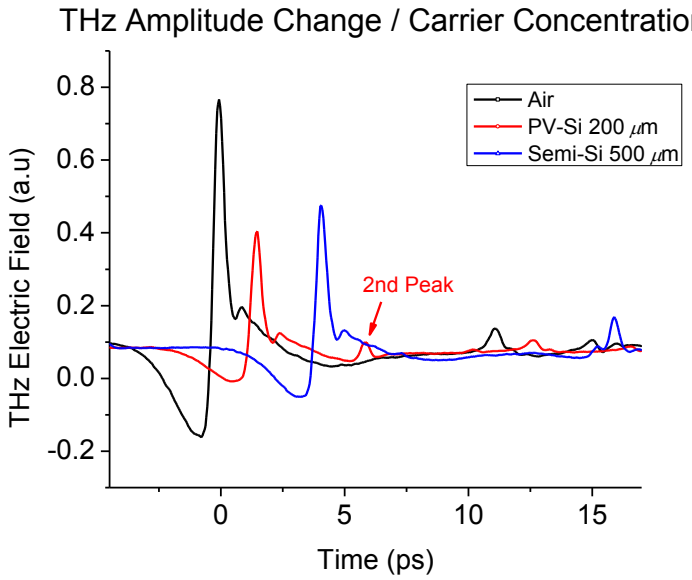

Figure 4.1 Examples of the electric field of THz pulses mapped out with sub-picosecond resolution. Shown is a reference scan just propagated through air (black), a commercial mc-Si PV wafer (red) and an IC silicon wafer (blue).

The terahertz pulses shown in Figure 4.1 are made up of the superposition of terahertz light from approximately 0.2 THz to 1.5 THz. Pulses with this bandwidth can easily be generated with the current generation of robust, turn-key and affordable fiber lasers ideal for manufacturing environments. Using amplified laser systems, and more advanced methods of terahertz generation like plasma generation, individual pulses with terahertz bandwidth form 0.5 to 10 THz and more can be generated (which would allow for even greater ability to monitor doping profiles) [41, 107, 134, 135]. By doing a DFT of the time domain data in Figure 4.1 the spectral or frequency domain information in these pulses can be extracted as shown in Figure 4.2. We have shown previously that this spectral information can be used to extract the precise wafer thickness with much higher accuracy than the time domain data [136]. Here we will show that this spectral data can also be used to monitor doping profile compliance in typical PV wafers.

Shown in Figure 4.2 is the frequency dependent power ratios (pulse propagated through the sample divided by a reference pulse propagated the same distance through air) for the pulses in Figure 4.1. Firstly note that the 'oscillations' result from the well-known Fabry–Pérot effect (the wavelength of terahertz light, 30 to 300 μm in air, is close to the wafer thickness resulting in interference effects) with the thicker IC wafer having more resonant peaks, exactly as expected. Secondly, note that the more highly doped PV wafer has significantly more attenuation (free carrier absorption) than the IC wafer. Thirdly, note that the deeper and somewhat more complicated doping profile in the mc-Si PV wafer typically results in more fine structure in the spectrum.

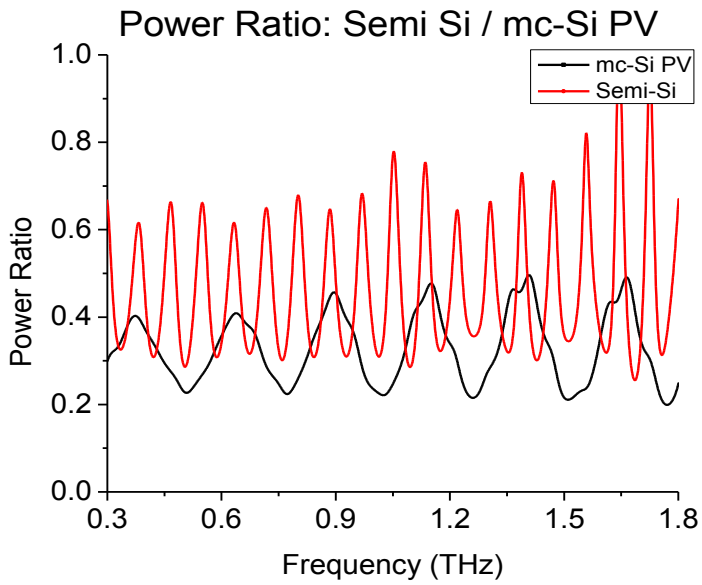

Figure 4.2 The spectral power ratio of the pulses shown in Figure 4.1. The power ratio is calculated by taking the DFT of the pulses in Figure 4.1 and dividing that by the DFT of a reference pulse.

4.3.1 Numerical Simulation of Phosphorus and Boron Doping Profiles

The doping profile recognition concept in this work is demonstrated both for PV solar cell wafers pulled from a manufacturing line and for standard (IC industry) semiconductor silicon wafers with doping profiles fabricated in house in RIT's cleanroom facilities

(Semiconductor & Microsystems Fabrication Laboratory). Silicon wafers (CZ, 475-575 μm, boron-doped, (100), 10-25 Ω-cm) was diced into pieces. A Bruce furnace was used to grow ~17 nm dry oxide on the wafer surface as confirmed by Ellipsometry (Nanometrics Spectrophotometer). A Varian 350D ion implanter was used to implant either phosphorus (P_{31}) or boron (B_{11}) dosages into the sacrificial oxide layer described above. Three dose levels, 10^{14}, 5×10^{14} and 10^{15} atoms/cm^2, were used designed to create doping profiles with different overall doping densities. A 1000 ºC and 3.5, 5, 6 or 12 hours high temperature drive-in process was used to activate the dopants and fabricate different doping profiles. Finally a hydrogen fluoride (HF) solution was used to remove the top dry oxide layer. The resulting doping profiles were predicted by SILVACO simulations and the accuracy of the simulations were confirmed by CDE Res Map measurements together with a PC1D model.

Distinct doping profiles are predicted in Figure 4.3 from a SILVACO simulation. Peak carrier concentrations are obtained from CDE Res Map sheet resistance measurements (in good agreement with the SILVACO simulations) and are 2.0×10^{18}, 9.2×10^{18} and 1.6×10^{19} atoms/cm^3 with a junction depth ~ 2 μm for the various P_{31} implant dosages (10^{14}, 5×10^{14} and 10^{15} atoms/cm^2). For the B_{11} implant dosages (10^{14}, 5×10^{14} and 10^{15} atoms/cm^2) the peak carrier concentrations are 3.2×10^{18}, 7.1×10^{18} and 1.2×10^{19} atoms/cm^3 with a junction depth ~2.25 μm. Figure 4.3 (c) shows a SILVACO simulation of the profiles of samples with identical implant dosages (10^{14} atoms/cm^2) but different drive-in time.

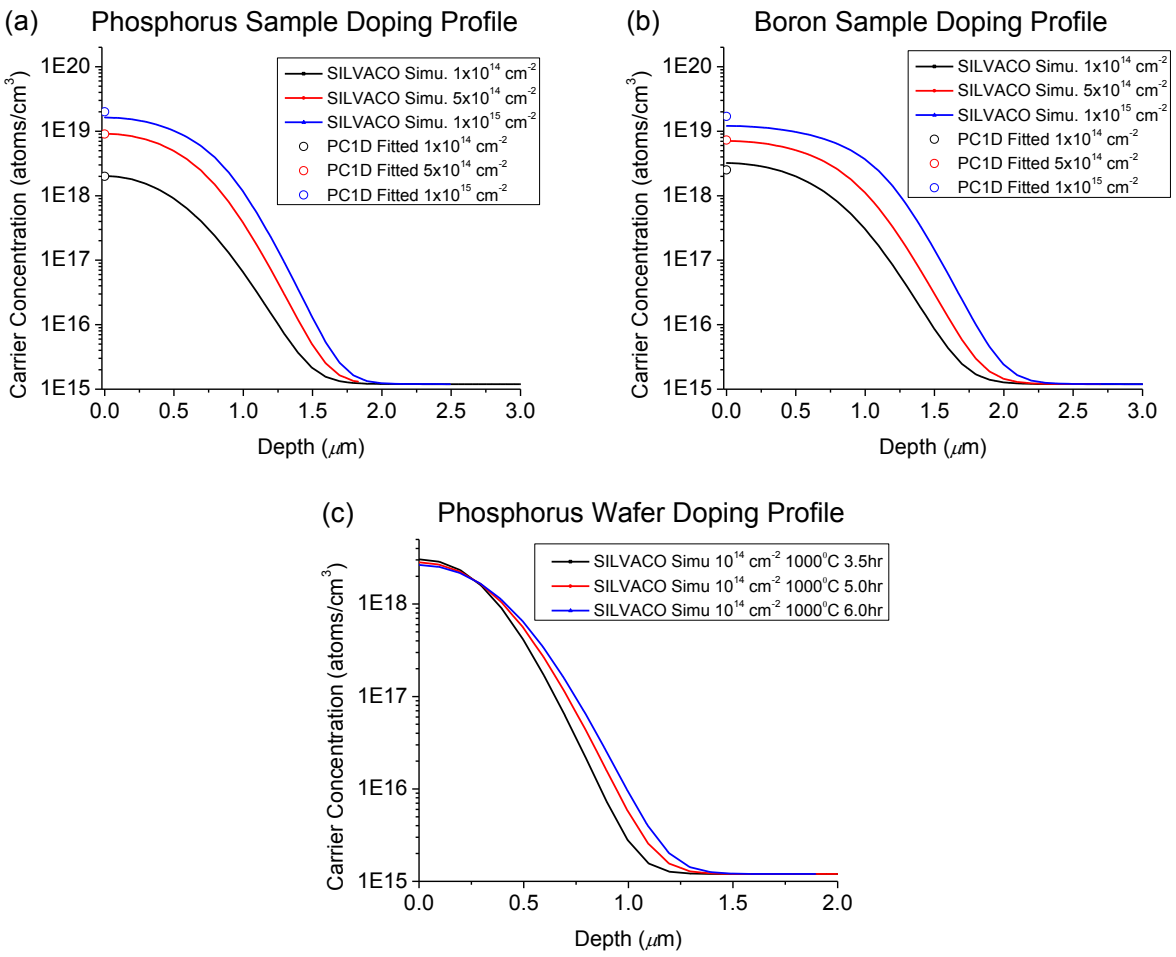

Figure 4.3 SILVACO simulated P_{31} doping profiles. The drive-in time of these profiles is the same (1000ºC 12hr). (b) SILVACO simulated B_{11} doping. The drive-in time of these profiles is the same (1000ºC 12hr). Open circles are peak concentrations from the CDE Res Map measurement and PC1D model. Implant dosages for all plots are given in the legend. (c) SILVACO simulated P_{31} doping profiles. The implantation dosages are the same (10^{14} atoms/cm^2) but the drive-in time are slightly different (3.5, 5 and 6 hrs).

4.3.2 Recognition Result in Time Domain

Figure 4.4 shows the THz measurement in the time domain for several wafers. Relative to the air scan in the Figure 4.1, the maximum (main) peak locations of all P_{31} and B_{11} samples are shifted (delayed) by about 4 ps. This shift is almost completely determined by the increased optical length of the silicon substrate compared to air (refractive indices Air: 1, Si: ~3.4). As expected one can clearly observe smaller THz amplitudes with samples containing higher doping concentrations. The sequence of THz amplitude (E_{THz}(Imp. Dosage)) in the P_{31} samples are E_{THz}

(10^{14}) > E_{THz} (5×10^{14}) > E_{THz} (10^{15}). This result shows that different doping dosages result in distinct THz signals even in the unprocessed time domain data. A similar peak delay is found when looking at the 2nd peak location (15-16 ps), which result from the internal reflection of THz light within the wafer (~×3 optical length). However, the shape and attenuation of this second peak is more complicated since it is altered even more strongly by 1) the dispersion between THz frequencies within the doping profile (which it traverses up to 3 times as opposed to the one time only of the primary peak) 2) the different levels of absorption of different terahertz frequencies within the doping profile region and 3) the unique differential internal reflection of different frequencies from the doping profile (some frequencies will reflect more and some less and at different points within the profile). (The information about the doping profile encoded in the dispersion and frequency dependent absorption is not easily accessible in the time domain. Hence we now turn our attention to the frequency domain by looking at the Fourier transform of pulses like those shown in Figure 4.4 (sample pulses) divided by the Fourier transform of pulses though identical undoped wafers (reference pulses).

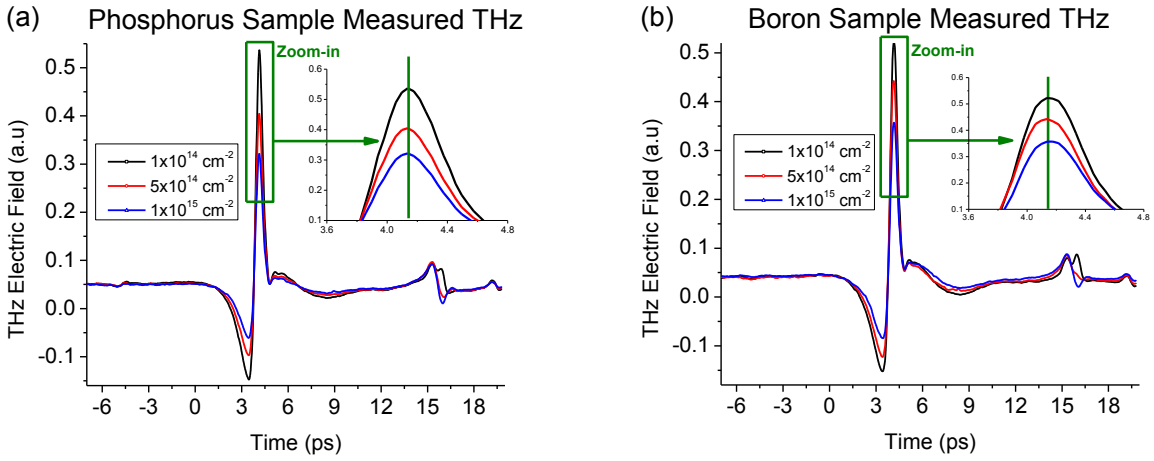

Figure 4.4 (a) THz-TDS measured THz pulses propagated through samples with P_{31} doping profiles with different dosages. (b) THz-TDS measured THz pulses propagated through samples with B_{11} doping profiles with different dosages. The drive-in time of all these profiles is the same (1000ºC 12hr).

4.3.3 Recognition Result in Frequency Domain

As shown in Figure 4.4, the doping layer (junction depth) is too thin to shift the THz peak in the time domain by a detectable amount relative to the much larger shift due to the ~ 500 μm substrate. However, as shown in our previous work [136] the resonant peak positions in the frequency domain is extremely sensitive to not just the physical substrate thickness but also to the increased optical thickness (i.e. light slows down as if the sample is significantly thicker) due to the very high refractive index (> 80) of highly doped silicon. Equally significant is the fact that the doping profile causes unique dispersion (different phase shift between different frequencies) and also unique patterns of internal reflection for different frequencies. These factors together result in a unique transmission spectrum in some ways similar to fingerprint.

It is these considerations that make the power transmission ratio in the frequency domain a very sensitive indicator of doping profile change. To produce the power spectra shown in Figures 4.5 & 6 a DFT of the measured time domain waveform (as in Figures 4.4, 4.7 & 4.8) is done. To calculate the power ratio the transmission spectrum through a doped sample is then divided by a reference spectrum which in this case is the transmission spectrum through an identical wafer with no doping profile (or a piece or area of the same wafer that was not doped). Both the primary and 2nd peaks are included during DFT since as explained above the 2nd peak is relatively rich in structural information regarding the doping profile. (In principle there is also a smaller 3rd and 4th etc. peaks corresponding to multiple internal reflections that can be recorded and included in the analysis provided one has a system with the dynamic range to measure them accurately. In our case however the attenuation of the third peak due to doping was so much that it was at the noise floor and hence it was not included in the analysis here.)

Figure 4.5 show that one can clearly distinguish between different doping dosages in both P doped and B doped samples. The trend of resonant peak amplitude is exactly as expected going from large (less absorption) to small (more absorption) as with implant dosages go from small to large $10^{14}/5\times10^{14}/10^{15}$ atoms/cm^2, respectively. The result suggests that the THz sensitivities to P31/B11 dopants are alike and THz pulses can be used to monitor doping dosages in-line for quick turnaround quality control for both n-type and p-type emitters.

Results as in Figure 4.5 demonstrate that the THz-TDS approach can distinguish differences in doping dosages. (Strictly speaking the technique distinguishes between differences in activated dopants and not implantation dosages because the THz response is to free carrier density and mobility and hence scales only with activated dopants.) This result is not surprising when one consider the very high optical contrast between undoped silicon and doped Si in the terahertz region of the EM spectrum (n=3.4 for undoped vs more than 80 at high doping). However, the answer to the question whether or not THz-TDS can be used to distinguish between doping profiles differences (in shape or depth) when the implant dosages and total (integrated) amount of active dopants are identical is not obvious? To answer this question we fabricated samples with identical implant dosages and total active dopant levels (see Figure 4.3 (c), same implant conditions and drive-in temperature were used, the different wafer pieces were just taken from the furnace at different times). The data in Figure 4.6 shows that the frequency domain power ratios of THz-TDS data can indeed be used to distinguish between doping profiles differences as small as those shown in Figure 4.3 (c).

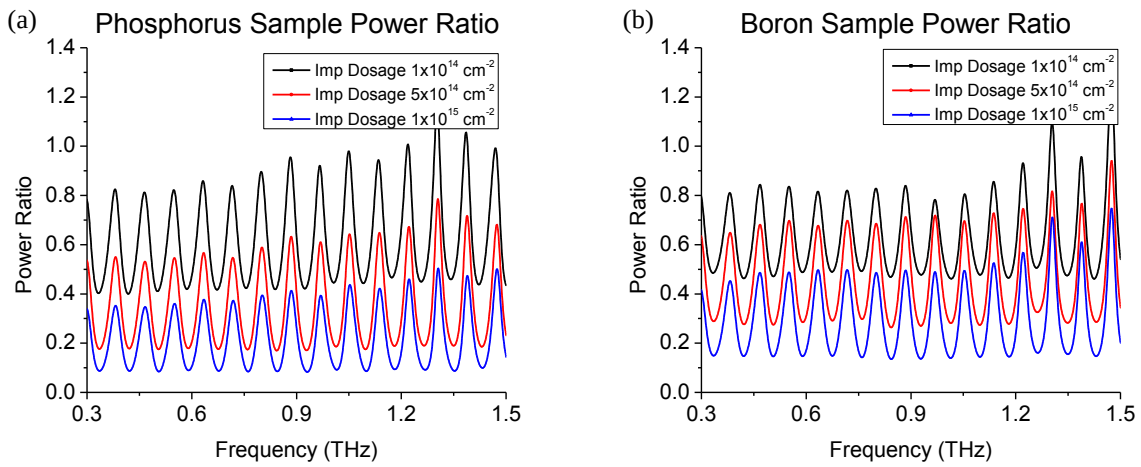

Figure 4.5 (a) Power transmission ratios of P_{31} samples with different implant dosages. (b) Power transmission ratio of B_{11} samples with different implant dosages. The drive-in condition for all spectra is the same (1000ºC 12hr). The reference scans for all power ratios are identical silicon wafers without any doping profile.

4.3.4 Evaluation of THz Measurement Uncertainty

Although a significant power ratio difference is observed, it is important to understand how large (and reliably repeatable) this difference is compared to measurement noise. Figure 4.6 illustrate the relative repeatability (over weeks) of the measurement compared to the doping profile induced differences. A wafer with an implant dosage 10^{14} atoms/cm^2 (P_{31}) and a 1000ºC 3.5hr drive-in time was measured on distinct days and the power ratios were compared to wafers with 1000ºC 5 and 6hr drive-in time (implant dosages are the same). The average point by point difference between the 'very similar' 5 hr and 6 hr profiles is 12.3 % while the average measurement error with our current hardware is 1.1 % (the average deviation between measurements on the same wafer on different days). The measurement noise is an order less than the drive-in condition change and proves the repeatability of the measurement.

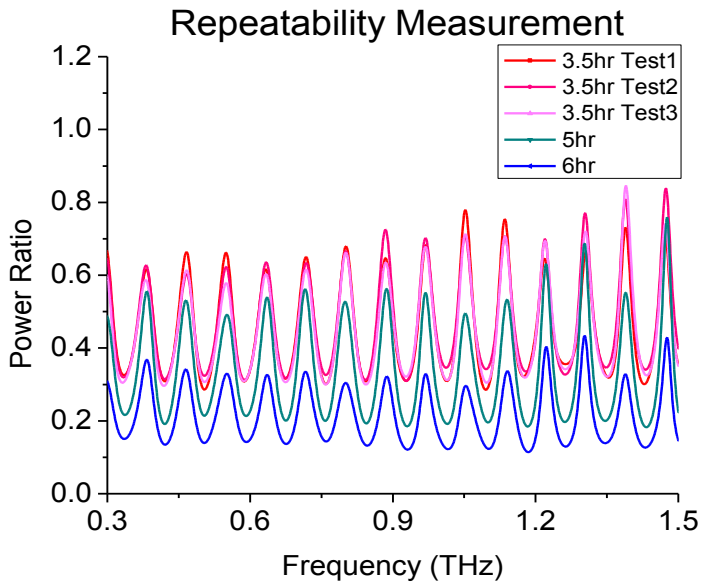

Figure 4.6 Repeatability test of one wafer (dosage 10^{14} cm^{-2}, drive-in time 1000ºC 3.5hr) on three different days. Also shown are two different wafers with different drive in times (5 and 6 hr). The corresponding predicted profiles are shown in Figure 4.3 (c). Note that all these profiles have identical implant dosages – the spectral differences are due only to differences in the doping profile due to drive-in time. The reference scans for all power ratios are identical silicon wafers without any doping profile.

4.4 Recognition Demonstration on a Commercial mc-Si PV Cell

The experiments above confirm that THz-TDS can be used to monitor the diffusion process and in particular dosage, activation and evolution of doping profiles in manufacturing. The question remains whether this technique is compatible with the features of real-world production wafers and solar cells. A particular challenge to many metrologies are the texturing of scattering and antireflective coating layers. Also of concern is the relatively higher (than the ~ 10^{15} cm^{-3} used above) substrate doping levels typically used for the base in Si-PV. To test the applicability of our approach to real world PV manufacturing we obtained and tested wafers from various points in production from a major Si solar cell manufacturer. Figure 4.7 shows time domain THz measurements on wafers from all stages of the typical mc-Si PV production process prior to metallization. (The individual labels are explained in the caption. A combined label, for instance "TX+DF", means the particular wafer was processed through the texturing and diffusion

stages and then pulled for analysis.) Compared to the air reference scan, main peak locations of all sample scans are located at ~ 2 ps due to the 200 μm wafer PV wafer thickness. The typical 10^{16} cm^{-3} substrate carrier concentration absorbs ~ 53% THz amplitude (ratio of TX/Air) and the emitter added by the diffusion process increased terahertz absorption enough to result in another ~50% reduction in THz amplitude. As hoped the edge isolation process do induce any noticeable change in the THz signal. The thin Si_3N_4 layer (~80 nm) indeed does not cause measurable scattering or absorption to the long wavelength THz radiation (30-300 μm) and the very small reduction in THz amplitude observed is likely due to impurities inside the Si_3N_4 layer or a slight increase in the front end reflection loss of THz light.

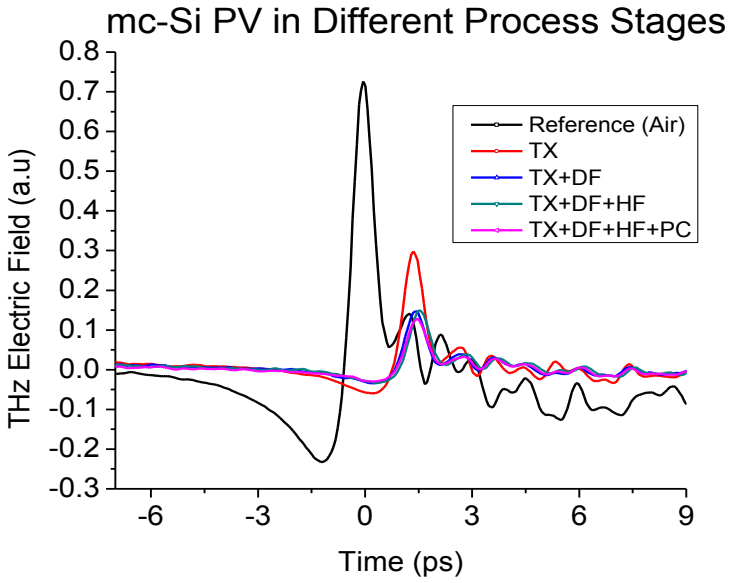

Figure 4.7 Time domain THz measurement in different mc-Si PV process stages. TX: texturing, DF: diffusion, HF: edge isolation, PC: Si_3N_4 anti-reflection coating. Small wiggles after the main peak result from the water vapor in the air. The THz amplitude in the edge isolation stage is the same as in the previous diffusion stage. The impurities in the Si_3N_4 film cause a small THz absorption.

To illustrate the ability to do doping profile recognition or monitoring in commercial PV wafers we fabricated our own doping profiles on the commercial TX wafers (after the texturing but before the doping step). We chose conditions so as to produce roughly similar doping

profiles (junction depths) than the profiles of the commercial PV production line diffusion process. (See inset on Figure 4.8(b) for a comparison of the resultant doping profiles). Time domain and frequency domain THz measurements comparing the industrial production line wafer and our locally produced wafer are shown in Figure 4.8. Note that the differences between the two wafers in the time domain are relatively small as is typical for samples with roughly the same dopant levels. As shown before the frequency domain power spectra are richer in detail able to distinguish doping profile shape differences. Note that neither the texturing nor the relatively highly doped substrate took away the ability of the technique to distinguish between and characterize doping profiles.

Currently, the PV industry typically uses four-point probe measurements to monitor the emitter diffusion process stability through sheet resistance. However, monitoring the surface resistivity is just a rough check because the carrier distribution inside the wafer could be and frequently is different. In the case shown in Figure 4.8 (b) for instance, the two samples have a virtually identical sheet resistance (DF: 70.02 Ω/□, Imp: 71.12 Ω/□) but a significantly different doping profile inside the wafer. This shows clearly that the four-point probe technique cannot by itself completely reliably monitor the actual doping profile compliance. However THz-TDS can distinguish even relatively small sub-surface doping profile difference sometimes in the time domain and even more so in the frequency domain (Figure 4.8 (a)(b)). This capability of THz-TDS could be exploited to achieve higher levels of in-line, or almost real time, on spec process control and quality control in the PV industry – something that especially desirable in high throughput operations.

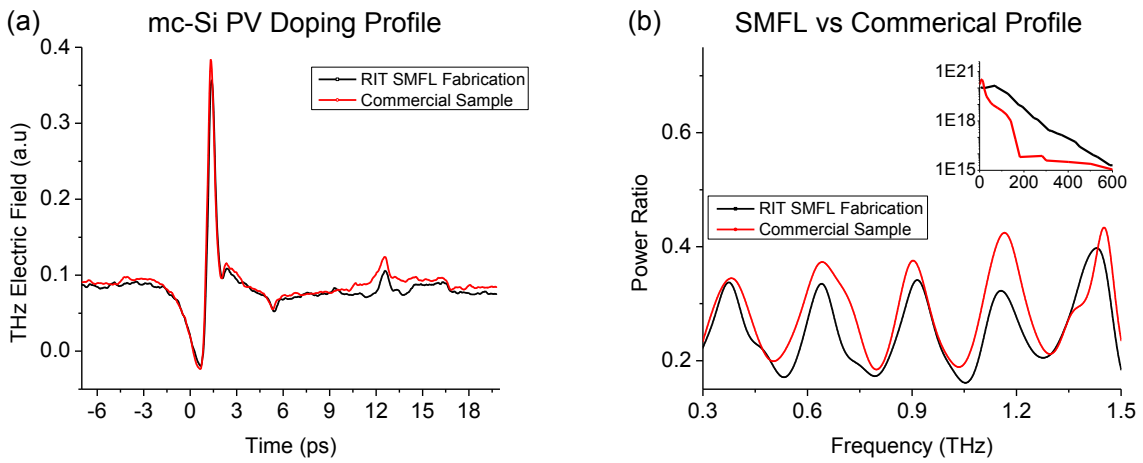

Figure 4.8 THz measurements on mc-Si textured solar cell wafers. Shown are measurements on a sample with a doping profile that resulted from a commercial diffusion process (red) and a doping profile obtained by ion implantation and thermal drive-in in our cleanroom on an identical commercial mc-Si textured wafer (black). (a) Transmitted pulses in real time and (b) power transmission ratios comparing the THz transmission of the commercial diffusion and in-house ion implanted samples all on identical textured mc-Si wafers. The reference in both cases is a textured mc-Si silicon substrate without any doping profile. The smaller figure in the upper-right location depicts the SILVACO simulated and ECV measured doping profiles.

Finally, to further confirm that the large wavelength THz-TDS technique could reliably handle the intentionally surface morphology or texturing (typically pyramid texture structures ~ 4 μm in height) of commercial Si solar cell wafers we measured different locations on the same commercial textured mc-Si PV wafer. Two typical power transmission ratios from two distinct spots are shown in Figure 4.9. The good overlap these spectra and all measured show that variations in the PV surface morphology do not influence the ability of the THz measurement to recognize similar or dissimilar doping profiles. (The terahertz spot-size on the wafer can be chosen down to the diffraction limit of about 1 mm depending on the resolution or amount of area averaging desired.) The ~ 5 mm diameter spot used averages over 1000's of 'pyramids' so that local (on the order ~ 10 to 100 μm) variations in texturing do not introduce random noise in the measurement. Moreover, the long wavelengths (> 200 μm) of the THz radiation used here

means it does not get scattered like the light used in most other shorter wavelength metrology techniques.

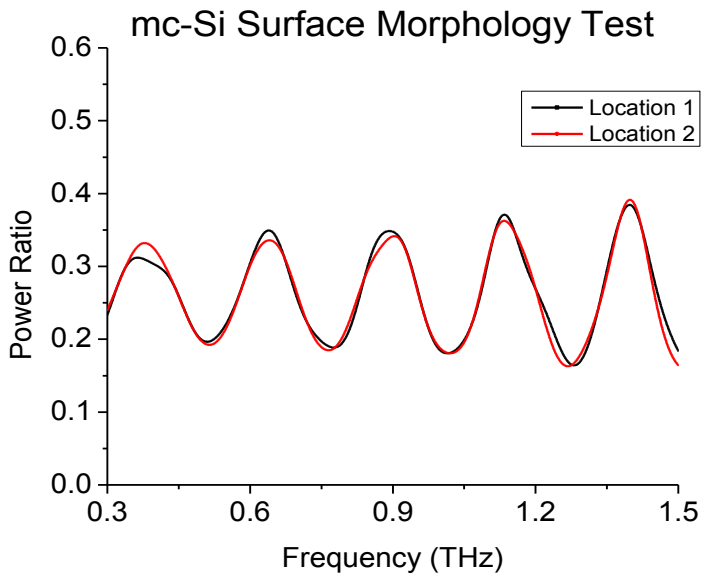

Figure 4.9 Power ratios at two different locations on the same textured mc-Si solar cell.

4.5 Conclusions

We demonstrated that THz-TDS can be used to monitor and detect differences or process deviations in doping profiles dosages. A less predictable capability also demonstrated here for the first time is the ability to distinguish between doping profile shapes even when the total dopant amount (dopant dosage) within the different profiles are the same. We also showed that the free carrier distribution (or activated dopant distribution) can be monitored in both n-type and p-type emitters using THz-TDS measurements. We demonstrated day-to-day measurement deviations (repeatability) that are 10 times smaller than the difference in signal between the smallest doping profile differences studied. Finally, we demonstrated that none of the features of commercial silicon solar cell wafers significantly interfere or impede the application of this technique. In particular it is demonstrated that standard solar cell wafer texturing does not present a major challenge to long wavelength terahertz light. In conclusion we showed an

example of THz measurements on two mc-Si samples with virtually identical sheet resistances but with two different doping profiles. We note that THz-TDS can reliably distinguish the doping profile differences between these wafers but the standard four-point probe technique, used most often in industry to monitor emitter profile compliance, cannot. Based on the experimental results presented, and the low cost turn-key options for THz generation and detection that came to market in recent years, THz-TDS based approaches show promise for use in manufacturing and quality control metrology in the PV and related industries.

5 TERAHERTZ REFRACTIVE INDEX OF PHOSPHORUS DOPED SILICON

To predict an accurate THz transmission and reflection in the transfer matrix, an empirical refractive index library is the key component. It was a challenge in the past to generate this library because no THz radiation can survive after penetrating heavily doped and thick silicon. Now, using SOI wafers solves this problem by having a change to create a thin and flat doped region in the top silicon layer. In this chapter, the detail process of generating a P_{31} refractive index library from carrier concentrations 1.2×10^{15} atoms/cm^3 to 1.8×10^{20} atoms/cm^3 is displayed. Surprisingly, the refractive index from 0.2 – 8 THz obeys the prediction in the simple Drude model and the slightly offset can be interpreted by heavier effective masses in the impurity bands and THz emissions. The same analytical procedure can be applied to study the refractive index in materials using other dopants. In this chapter, we only focus on the detail introduction of the library generation. The revised content, which contains physical interpretations and data fitting using theories of impurity bands and THz emissions, is scheduled to submit to the journal "*Science*" in 2014.

5.1 Introduction

Doped silicon is one of the technologically most important materials that ever made it from a physics laboratory into everyday applications. Within science doped silicon serves as a widely studied prototype system for exploring "arguably the most important model in condensed-matter physics" [137, 138] – models that describe the free carrier gas or Fermi liquid formed by free electrons in solids. The optical spectrum of doped silicon in the terahertz region

below 8 THz is determined almost exclusively by a very strong light-free carrier interaction. In the century since Paul Drude formulated his well-known theory for conductivity in metals [60, 139], many physicists, particularly after quantum mechanics refined our understanding of solids, suggested that such a simple "classical" theory is useful only as a rough first approximation or intuitive picture of the free carrier response in metals and semiconductors [46, 140-142]. In the case of silicon the complexity that quantum mechanics reveal is indeed considerable; the conduction band minimum consists of six degenerate valleys with ellipsoidal Fermi surfaces (see Figure 5.1 (b)). In each valley conductivity is anisotropic with very different transverse and longitudinal effective masses (m_t = 0.19 vs m_l = 0.91). Free carrier scattering at room temperature is a combination of phonon scattering (both acoustic intravalley and nonpolar-optical & acoustic intervalley) and ionized & neutral impurity scattering [143, 144].

Over the last two decades optical experiments in the terahertz and microwave proved that the relatively simple Drude model can indeed accurately describe the bulk response of free electrons to light in many materials (in particular lightly doped semiconductors [38, 61, 62, 130, 144-146] and superconductors [139, 147]). However the main prediction of Drude's model, namely the bulk free carrier optical spectrum in a metallic system, has to date never been tested by direct measurement (without for instance Kramers-Kronig extrapolation) [49, 139, 148, 149]. There are two reasons why the free carrier spectrum of a metal has not been measured to date. Firstly, techniques capable of the direct simultaneous measurement of both the real and imaginary refractive index in the terahertz region matured only in the last few decades. The broadband plasma generation technique used here are state of the art [41]. Secondly, even Drude himself anticipated that the inherent high reflectivity of metals would pose a major experimental challenge to measuring the bulk free carrier response in metals [139, 150], a fundamental

obstacle that modern terahertz reflection techniques do not escape [101]. In this work these challenges are overcome by fabricating uniformly doped samples as in Figure 5.1 (a). The doped region is fabricated thin enough to not be subject to bulk Fresnel reflection yet is thick enough so that the transmitted terahertz light predominantly probes the bulk free carrier response. By mapping out the electric field vs. time of broadband terahertz pulses transmitted through samples with various doping densities the real and imaginary refractive index in Si:P is measured directly.

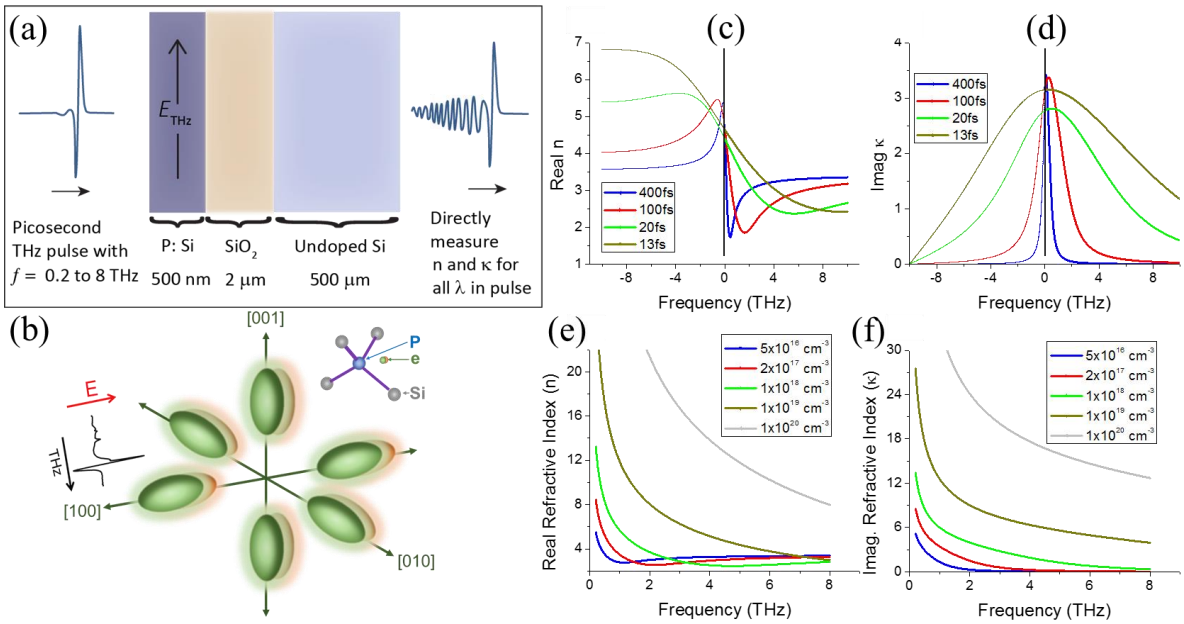

Figure 5.1 (a) Typical sample structure: A thin uniformly doped layer on top of an insulating oxide blocking layer on an undoped (THz transparent) substrate. (b) An illustration of the ellipsoidal Fermi surfaces of the silicon conduction band and conductivity by displacement (in k-space) of the six 'carrier pockets' by an electric field (in our experiment the E-field of a pulse of terahertz light). (c-d) Illustration showing the Drude prediction of the evolution of the optical spectrum of a free carrier plasma with scattering time. At large τ the spectrum has the familiar Lorentz line shape centered at DC. As τ approaches values typical of metals (τ~ 10 fs or less) a much broader free carrier response spanning the THz is predicted. (e-f) The Drude prediction of the evolution of the free carrier spectrum with carrier density.

The minimum difference of complex THz transmission between the measurement and simulation from the transfer matrix is utilized to achieve an electrical doping profile prediction in

silicon. To just get a rough idea, of course the simple Drude model can be directly used to theoretically calculate how the difference of complex transmission changes with various doping profiles in the fitting process. However, it won't be better than having an experimental library to estimate the actual difference of complex transmission. A refractive index library in THz regions, which covers the overall free carrier range of predicting a doping profile, therefore becomes an essential information to have. On the other hand, exploring whether a heavily doped silicon really acts as a metallic system through its optical spectrum is also a meaningful research from the fundamental science point of view. These two reasons lead us to work on this topic in detail and the information is expected to be beneficial for the estimation of the electrical performance of device in THz regions.

5.2 Materials and Methods

The specialty of this topic is not only the designed method to extract the refractive index, but also the effort to prove its accuracy. The reported information in later sections is only about the Si:P library since the doping profile prediction is initialized on the phosphorus doping profile in silicon. The generation of the Si:B library is now on the way by another master student through a similar procedure.

5.2.1 Terahertz System Setup

THz measurements were done in two different THz systems from two different labs. In our RIT lab, THz radiation is generated by the photoconductive antennas method, which is well described in Chapter 1. Its frequency covers the range from 0.2 – 2 THz. In the UR lab, THz radiation is generated by the state-of-the-art THz-ABCD technique, covering the range up to 8THz. A detailed description of generation and detection using the ABCD plasma generation can be found elsewhere [41, 107, 151]. System particulars are: A regenerative Ti:Sapphire amplifier

(Coherent Inc., Legend, Gottingen, Germany) with 8 mJ pulse energy, 800 nm central wavelength, 35 fs pulse duration, and 1 kHz repetition rate is utilized for the optical source. A fraction of the source beam is frequency doubled to produce a co-propagating 400 nm beam. Both the 800 and 400 nm beams are tightly focused in air to induce ionization. Frequency mixing of the plasma currents driven by 800 and 400 nm femtosecond pulses result in the radiation of short broadband terahertz pulses that is focused and used for spectroscopy. The references pulses and pulses transmitted through the samples are mapped out using free based electro-optic sampling based on the inverse of the generation process (THz light + 800 nm light mix to produce 400 nm light). The complex refractive index of the multilayer samples were obtained directly from the measured data using same standard THz-TDS methodologies.

5.2.2 Flat Doping Profile Formation using SOI Wafers

High quality SOI wafers was purchased from Soitec with the structure being nominally 500 nm intrinsic top Si / 3μm SiO_2 / 500μm Si substrate. The SOI wafers were fabricated with Smart Cut™ technology to transfer and bond a thin layer of high quality single crystalline silicon from a donor substrate to a SOI stack. This approach provides high quality single crystal silicon at submicron thickness without strain and with minimal damage (The silicon crystals used in our report has a (100) orientation). To fabricate the sample sets with the seven high doping levels ($>10^{17}$ atoms/cm^3) the following cleanroom process flow, shown in Figure 5.2, was followed at the SMFL cleanroom at RIT (10 000 sq. ft. SMFL class 1000/100/10). A similar sample fabrication has been described using bulk silicon wafers in Chapter 4. Firstly, ~17 nm sacrificial dry SiO_2 was grown on the top Si in a dedicated Bruce tube furnace. Then phosphorous ion implantation was done with a Varian 350D Ion Implanter (30 KeV implantation energy with dosage adjusted to achieve the various doping levels). Dopant activation and drive-in was

achieved by annealing at 1000 ºC for 12 hours in a dedicated Bruce tube furnace. Finally HF chemical etching was used to remove the sacrificial oxide. The samples doped at lower (< 10^{17} atoms/cm^3) doping densities consisted of high quality single crystal uniformly doped wafers (~200 µm and ~ 600 µm) purchased from commercial vendors, characterized and used as is.

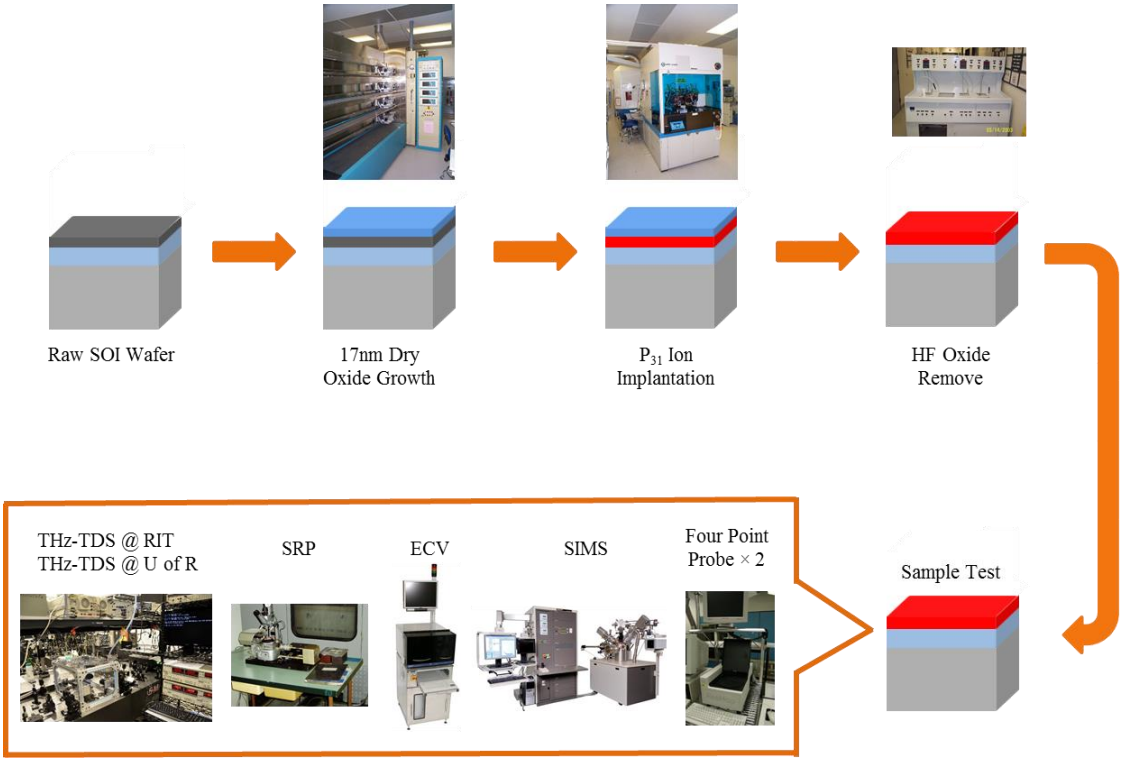

Figure 5.2 Fabrication procedure of various doping levels in SOI wafers and metrologies used to determine carrier concentrations.

5.2.3 Doping Level Determination in SOI Wafers

The uniformity (flatness) and concentration level of the doping profile was determined using SIMS, ECV, four point probe Rs and SRP measurements and a summary table is provided below. All three techniques confirmed a uniform fully activated doping profiles for all samples within the top silicon layer. The SIMS analysis was performed by Evans Analytical Group (EAG) using a PHI Adept 1010 Quad system. The results for the samples with phosphorus dopant levels 4.3×10^{18} cm^{-3} and 9.6×10^{19} cm^{-3} is shown in Figure 5.3. Uniform doping levels are observed in

the 500nm top Si layer validating the straightforward multilayer transfer matrix procedure used to extract the complex $\tilde{n}(\omega)$ of the doped top silicon layers from the measured terahertz transmission data ($\tilde{t}(\omega)$ for $\omega/2\pi$ = 0.2 to 8 THz).

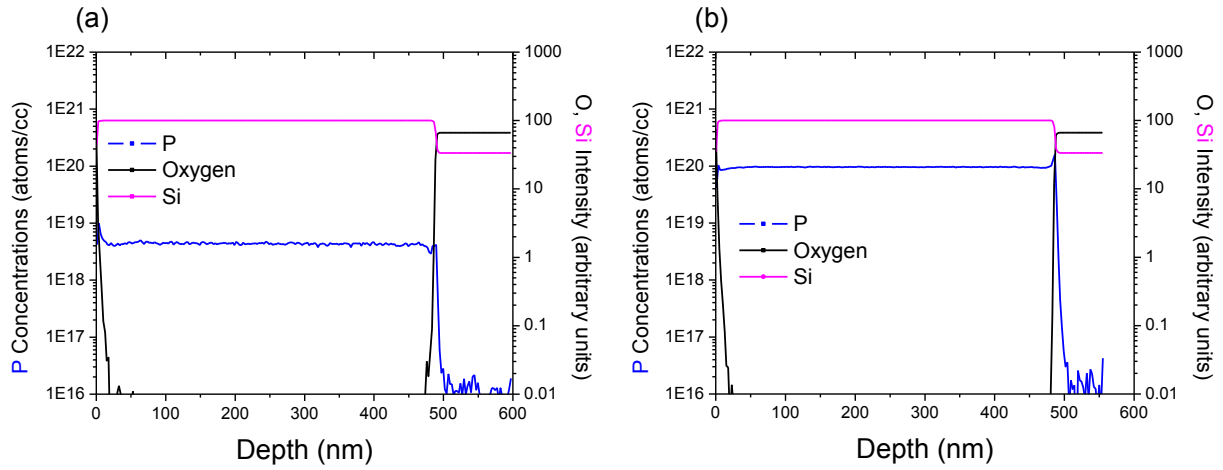

Figure 5.3 SIMS measured doping profiles in samples: (a) $4.3 \cdot 10^{18}$ atoms/cm^3 (b) $9.6 \cdot 10^{19}$ atoms/cm^3. The first ~ 500 nm is the top silicon layer followed by the box oxide to the right.

The sheet resistance and DC conductivity was measured for the benchmark. The sheet resistance of every sample was measured using a commercial Four Point Probe Resistivity Mapping Systems (ResMap 273, Creative Design Engineering) and cross-checked with a second custom four point probe system. The resultant average values for every sample from each measurement system are given in Table 5.1. The conversion from sheet resistance to bulk resistivity was then computed using the accurate top layer thickness data (see section 5.2.4) and a calibrated conversion algorithm for each of the two systems used (used daily for research and commercial work).

From Table 5.1, all four measurement techniques showed reasonable agreement. The agreement between the technique measuring the chemical dopant density (SIMS) and the techniques measuring the free carrier density (ECV (WEP CVP21)), SRP (SSM 100B SRP system by Solecon Laboratories (Reno

NV)), 4pt Probe) suggest that all dopants were activated as is expected for the dopant levels (N_D < 1.8×10^{20} atoms/cm^3) and drive-in conditions (12 hr 1000 ºC) used. With regard to dopant activation, also note that the offset between the measured and predicted optical spectra in Figures 5.6 cannot be the result of incomplete dopant activation.

Dopant/Carrier Concetration								
Ion Implantation Dosage (atoms/cm^2)	4 Point Probe ResMap (Ω/□)	N - 4 Point Probe (atoms/cm^3)	4 Point Probe RIT (Ω/□)	N - 4 Point Probe (atoms/cm^3)	N - SRP (atoms/cm^3)	N - ECV (atoms/cm^3)	N - SIMS (atoms/cm^3)	N in Drude Prediction (atoms/cm^3)
1.20E+16	9.80	1.78E+20	9.98	1.75E+20				**1.77E+20**
5.00E+15	17.32	9.88E+19	18.20	9.29E+19	9.09E+19	1.02E+20	9.63E+19	**9.62E+19**
3.00E+15	26.85	6.27E+19	27.90	6.04E+19				**6.16E+19**
1.00E+15	72.76	2.38E+19	76.90	2.24E+19		2.37E+19		**2.24E+19**
2.00E+14	234.40	4.76E+18	245.60	4.39E+18		4.56E+18	4.35E+18	**4.34E+18**
4.00E+13	511.60	1.24E+18	542.60	1.12E+18				**1.18E+18**
1.00E+13	1098.00	3.70E+17	1155.90	3.43E+17		2.06E+17		**3.56E+17**

3) Table 5.1 The carrier concentration comparison of all characterization techniques.

5.2.4 Layer Thickness Determination in SOI Wafers

Accurate extraction of the complex refraction index of the doped top silicon layer requires accurate knowledge of the precise thickness of the various layers in the samples. The thickness of the ~500 nm top silicon layers of the various wafers were measured using high-resolution scanning electron microscopy (HR-SEM) and the results were cross-checked using the commercial SIMS analysis. The HRSEM and the SIMS results matched closely. To prepare the wafers for reliable HR-SEM imaging the wafers were diced with a diamond blade and the exposed edges polished using a standard chemical mechanical wafer polishing tool (CMP). Exact thickness and uniformity of the various samples was then determined using side-on imaging of the wafers with a high resolution SEM (Zeiss Auriga). Figure 5.4 is an example of an SEM image at a magnification such that both the top silicon and box oxide are in view.

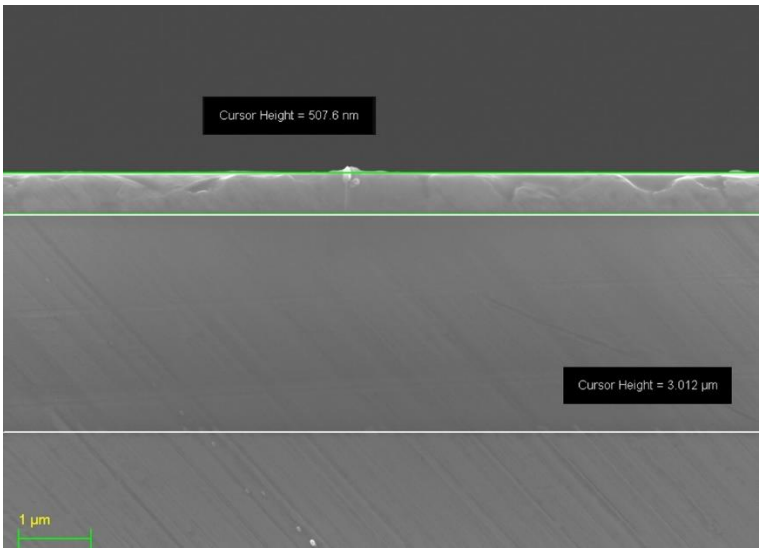

Figure 5.4 Example of the thickness determination of the top Si and box SiO_2 layers in the SOI wafers used. This particular sample had a top oxide layer 508 nm (± 10) and a box oxide 3.0 µm (± 0.1).

5.2.5 Single Peak Equation for Complex Refractive Index ($\tilde{n}$) Extraction

To eliminate resonances induced from the Fabry-Pérot cavity, the equation using just the information from the main peak was derived for the extraction of the refractive index library from SOI wafers. The basic concept in the derived equation is to exclude the internal THz reflection. Two steps process is required in the data analysis and a selected region in the THz measurement containing just the main peak is required while doing the DFT. In step 1, the term $(1-\tilde{r}^2)$ is utilized to exclude all internal reflections from the THz measured $\frac{E_{Si\_Sub}}{E_{Air}}$ and reversely calculate the refractive index $\tilde{n}$ in the silicon substrate. Air scan is defined in step 1 as the reference and the extracted $\tilde{n}$ is employed as $\tilde{n}_{Si\_Sub}$ in the next step. In step 2, $M_1 M_2 \ldots M_n$ represents a multiple layers structure to form the transfer matrix with terms A, B, C and D. In this SOI case, three layers structure $M_1 M_2 M_3$ is defined and only the top Si layer is the unknown factor to solve. The complex transmission $\frac{E_T}{E_0}$ is obtained from the measured $\frac{E_{sam}}{E_{Ref}}$ to

extract the complex $\tilde{n}$ in the top Si layer. In step 2, the silicon substrate without the top Si and box SiO_2 layers, is measured as the reference E_{ref}.

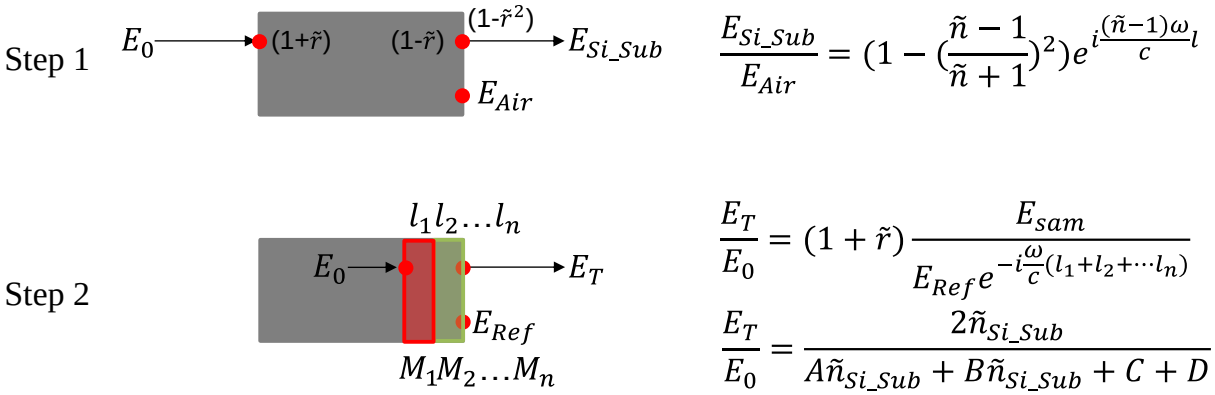

Figure 5.5 Two steps calculation of the THz refractive index from the main absorption peak.

5.3 Results and Discussion

5.3.1 Extraction of Complex Refractive Index

These measurements allow us to report here, for the first time, the results of the experiment Drude envisioned 114 years ago: The measurement of the bulk free carrier spectrum of a metallic material by measuring the complex refractive index ($\tilde{n}(\omega)$ = n(ω)+iκ(ω)) of highly doped silicon from 0.2 to 8 THz. By accurately measuring (cross-checked with four different non-optical methods) the free carrier density (N) and DC conductivity (σ_0), Drude's prediction of the optical spectra of phosphorous doped silicon is obtained completely independent of the optical measurements. Figure 5.1(c-f) shows the Drude prediction of how the optical spectrum evolves as a function of doping density and scattering time. Figure 5.6 shows the measured $\tilde{n}(\omega)$ across seven doping levels, including show a direct comparison of the pure Drude prediction of $\tilde{n}(\omega)$ with the measured $\tilde{n}(\omega)$ at two representative doping levels.

Except Drude model, another two approaches are utilized to predict σ_0 for the estimation of the complex refractive index. One is to measure the sheet resistance, convert the resistance to

$\rho(n)$ (bulk resistivity) and then $\sigma_0(n)$. Another one is to measure *N* and use one of the many widely used and validated tables listing for $\rho(n)$ vs *N* for single crystal Si:P (e.g ASTM, NIST etc. [152, 153]). In this work we calculated the predicted optical spectrum using all three approaches. Using approaches 1 and 2 the predicted spectra for all samples are as close as 0.9% and never more than 4.8% (for all samples at all frequencies within the reported range). Approaches 2 and 3 agree even more closely as is illustrated by the results for the 1.77×10^{20} cm^{-3} doping level (The result for all other doping levels is similar). Approach 2 has been used in Figure 5.6 to plot the Drude prediction.

To date the complex terahertz refractive index of doped silicon has been measured up to only the lightly doped level of 5×10^{16} atoms/cm^3 (within a full physically achievable range from ~ 10^{14} to 5×10^{20} cm^{-3} [143]) with the later measurement over the very limited spectral range of just 0.2 THz to 1.1 THz [145]. As a familiar point of reference note that the peak doping level in most integrated circuit and silicon solar cell diodes exceed 10^{20} atoms/cm^3. In all previously reported room temperature measurements ($N_D \leq 5\times10^{16}$ atoms/cm^3) both the electrons and holes (boron doped) in lightly doped silicon had Drude spectra [38, 61, 62, 130, 144, 145]. Notwithstanding these experimental results in the low doping region all (we could not find any counter example) explicit predictions or models in the literature [49, 142, 144, 154-159] of the free carrier spectra of highly doped silicon predict notable deviation from the Drude model.

Contrary to these expectations, the first direct experimental data in Figure 5.6 show that the Drude prediction does perform remarkably well in describing the line shape of $\tilde{n}(\omega)$ across all doping levels. Although the Drude model (with no fitting parameters) does predict the line shape correctly, it clearly also consistently overestimates the magnitude in highly doped silicon (> 10^{19} cm^{-3}) of both *n* and κ. In samples with ~10^{18} cm^{-3} doping levels, the Drude model

underestimates the magnitude of *n* but still overestimates the magnitude of κ. The last sample with the doping level ~10^{17} cm^{-3} then displays a better agreement of both *n* and κ between the measurement and the Drude model estimation. Note that the difference between the measured and predicted spectra itself has a Drude-like shape. These extracted information is already adequate for our research purpose.

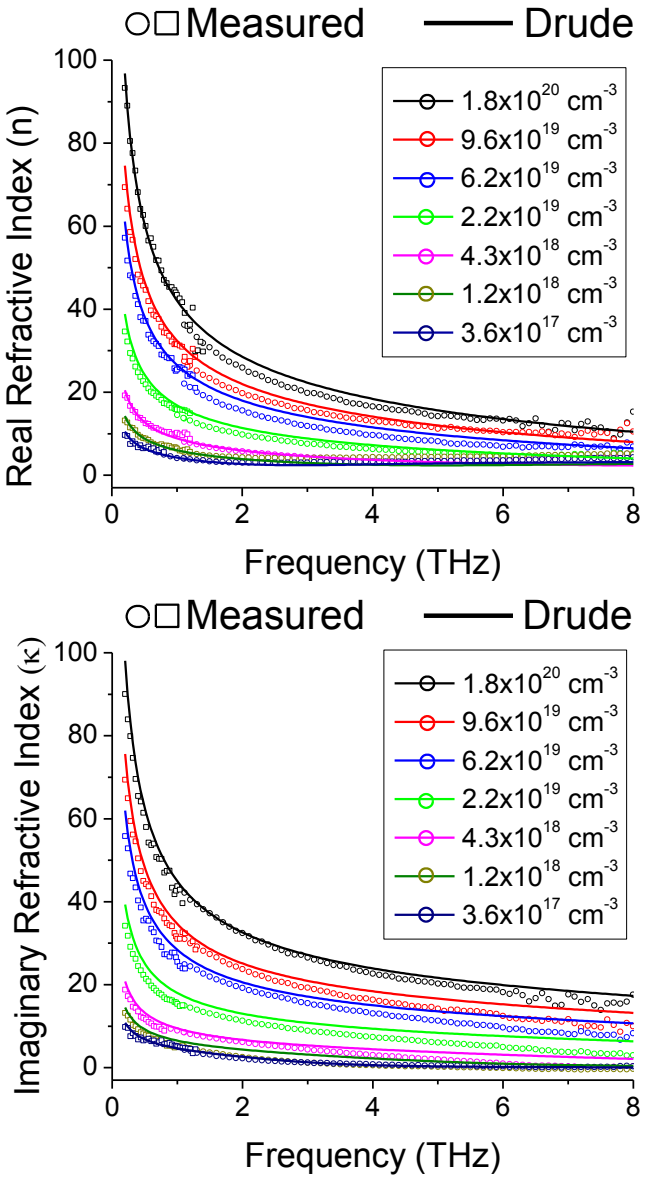

Figure 5.6 The measured terahertz complex refractive index for seven doping levels. The squares and circles are data points measured with photo-conductive antennas and circles are measured with plasma generation.

5.3.2 The Evolution of the Refractive Index Offset

The detail interpretation and data fitting regarding the resources of the observed offset will be discussed in the future submission in detail. Over here the evolution of relative mechanisms in different doping levels are introduced briefly. Two major theories participate the observed offset. Highly doped Si:P has an impurity band (IB) that starts emerging around N_D = 2×10^{17} atoms/cm^3 [138, 160-162]. This IB is responsible for the metal-insulator transition (MIT) that occurs at N_D = 3.5×10^{18} atoms/cm^3 [138, 161, 162]. Electrons in impurity bands with various effective masses as a function of doping level dominate the overestimation in highly doped samples, shown in Figure 5.7 (a). The overestimation reaches its peak at ~2×10^{19} cm^{-3} doping level and decreases as a function of the distribution change of impurity bands. In ~10^{18} cm^{-3} doping levels, impurity bands decompose to island type distributions. The major mechanism is gradually switched to another effect called THz emissions and induces the observed underestimation of the magnitude of *n*. The illustration in Figure 5.7 (b) indicates the peak of THz emissions at ~1×10^{18} cm^{-3} doping level. The combination of these two effects is observed at ~4×10^{18} cm^{-3} doping level. In ~10^{17} cm^{-3} doping levels, these two effects disappear and a close to zero offset is observed. The fitted curves (red) in Figure 5.7 (c) take these two effects into the consideration and show a perfect agreement with the extraction from the THz measurement on two selected doping levels (6×10^{19} cm^{-3} and 1×10^{18} cm^{-3}). In the 6×10^{19} cm^{-3} sample, the underestimation (lower than Drude model (green curve)) comes from the different effective mass, where the overestimation (higher than Drude model (green curve)) in the 1×10^{18} cm^{-3} sample results from THz emissions.

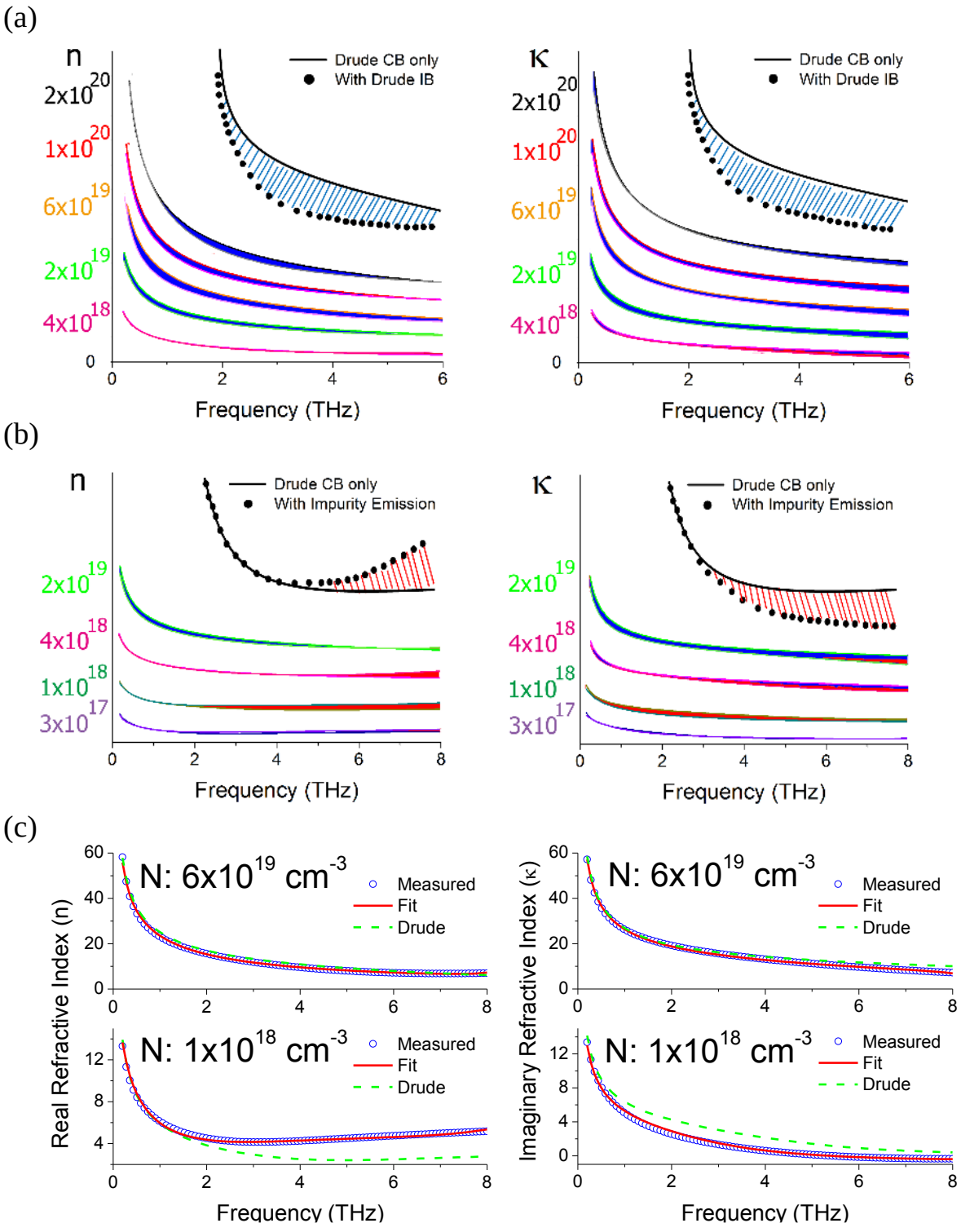

Figure 5.7 (a) The impurity band induced evolution of the refractive index offset in doping levels > 10^{18} cm^{-3}. (b) The THz emission induced evolution of the refractive index offset in doping levels between 10^{17} to 10^{19} cm^{-3}. (c) The measured data, the Drude prediction and the fitted data containing proposed mechanisms at two doping levels as examples.

5.4 Conclusions

For the first time, phosphorus refractive index in THz regions between carrier concentrations 1.2×10^{15} cm^{-3} and 1.8×10^{20} cm^{-3} is directly measured using THz techniques at room temperature and utilized in the transfer matrix to predict the complex transmission for the later doping profile prediction. Two THz systems from two different labs reach an acceptable agreement of extracted refractive index up to 8 THz and various characterization techniques are utilized to confirm relative doping levels. The shapes of extracted refractive index and its offset in all samples pretty much follow the prediction from the simple Durde model. Therefore, the doped silicon behaves like a metallic material in THz regimes. The offset to the Drude model prediction continuously brought us the attention of digging behind mechanisms from the fundamental science point of view and it is well fitted by the gradual change of electrons in impurity bands with various effective masses and THz emissions. This finding also opens the door of the solid state study in the use of a typical transmission mode THz-TDS at room temperature. The relative result has been reported in this chapter in brief and the detail interpretation will be covered in the future journal submission. The same analytical procedure has been repeated on the study of boron refractive index in THz regions to broaden the future application.

6 NUMERICAL MODELING OF DOPING PROFILE PREDICTION USING TERAHERTZ TIME DOMAIN SPECTROSCOPY

In previous chapters, essential information, including the impact from the bulk material thickness to a transmission mode THz measurement, the ability of silicon doping profile recognition and the generation of a phosphorus refractive index library, has been reported systematically to lead the potential application of *in-situ* doping profile prediction. Prior to the experimental demonstration, a mathematical modeling process using MathCad is done in this chapter to estimate the prediction performance in liquid diffusion profiles with kink-and-tail features. This study covers the practical window in the PV industry and the conjecture is applied to doping profiles with various features. One manuscript (Part III) based on the revised content is under preparation and the submission is scheduled to the journal "*Terahertz Science and Technology, IEEE Transactions on*" in 2014.

6.1 Introduction

Using a transmission mode THz-TDS to implement the non-destructive doping profile prediction is a new approach and has not many direct literatures to reference. From previous chapters, essential information required for this topic has been collected for a physical demonstration in the next chapter. Prior to that, a modeling process is reported in this chapter to pinpoint potential stumbling stones and lower the future experimental expense. The modeling aims at liquid diffusion profiles with kink-and-tail distributions as an example and utilizes mathematical models proposed by Wirbeleit *et al.* [163] to reduce the simulation complexity.

The same analytical procedure can be applied by having mathematical models for specific shapes (for example ion implanted profiles). During the profile prediction, multiple profiles owing very close complex transmissions is expected to lead a wrong profile estimation. This issue drives us to study the so-called "multiple degeneracy" problem through the modeling process, too. Degenerate is the situation that a limiting case in which a class of object changes its nature so as to belong to another, usually simpler [164]. In this research, degenerate (degeneracy) represents the same THz measurement result from multiple doping profiles, called theoretical degeneracy. Therefore, the question to us is: do we face the theoretical degeneracy problem? Another degeneracy problem, called practical degeneracy, is also frequently observed due to measurement uncertainties. The practical window of the liquid diffusion profile used in silicon based solar cells is applied to study their existences and the influence to the profile prediction. Strategies are then proposed to break the practical degeneracy and improve the accuracy of profile prediction.

6.2 Material and Methods

Theories and models applied to evaluate the performance of profile prediction are introduced in this section, along with the description of sample preparation for the physical demonstration of practical degeneracy.

6.2.1 Drude Model and Empirical ASTM Equation

To estimate the accurate change of complex transmission under various doping profiles, three vital notions are employed during the modeling process. First, equation 6.1 [165, 166] is adopted to empirically describe mobility and scattering time as a function of carrier concentration, where effective mass m_0 ($0.28\times m_e$) is applied in the equation to calculate the scattering time. Another empirical ASTM correction [152] (equation 6.2) is also applied to

calculate DC conductivity as a function of carrier concentration instead of the typically used formula $\sigma = \frac{Ne_c^2\tau(N)}{m_0}$. The empirical DC conductivity is proven to be close to the theoretical estimation. Drude model, shown in equation 6.3 – 6.6 [167], is applied to simulate complex refractive index (n+iκ) as a function of carrier concentration under THz frequencies. Refractive indices from profile segments are employed in the transfer matrix to simulate the complex transmission and refraction. The detail introduction regarding Drude model and transfer matrix can be found in Chapter 2.

$$\mu(N) = 65 + \frac{1265}{1+\frac{N}{8.5\times10^{16}\frac{1}{cm^3}}^{0.72}}\frac{cm^2}{V\cdot s} \tag{6.1}$$

$$\sigma_{ASTM}(N) = \frac{N}{6.242\times10^{18+z(N)}}\cdot S\cdot cm^2$$

$$z(N) = \frac{A_0+A_1y(N)+A_2y(N)^2+A_3y(N)^3}{1+B_1y(N)+B_2y(N)^2+B_3y(N)^3} \tag{6.2}$$

$$\varepsilon_1(\omega,N) = \varepsilon_{opt} - \sigma_0(N)\frac{\tau(N)}{\varepsilon_0\omega[1+(\omega\tau(N))^2]} \tag{6.3}$$

$$\varepsilon_2(\omega,N) = \varepsilon_{opt2} + \sigma_0(N)\frac{1}{\varepsilon_0\omega[1+(\omega\tau(N))^2]} \tag{6.4}$$

$$n(\omega,N) = \sqrt{\frac{\varepsilon_1(\omega,N)+\sqrt{\varepsilon_1(\omega,N)^2+\varepsilon_2(\omega,N)^2}}{2}} \tag{6.5}$$

$$\kappa(\omega,N) = \sqrt{\frac{-\varepsilon_1(\omega,N)+\sqrt{\varepsilon_1(\omega,N)^2+\varepsilon_2(\omega,N)^2}}{2}} \tag{6.6}$$

6.2.2 Enhanced Diffusion in Liquid Diffusion Profiles

Liquid diffusion process, interpreted by the Fick's law [168], is widely used in semiconductor (especially PV) industries to manipulate the device performance. In IC circuit field, steep diffusion profiles in heavily doped deep-source drain and ultra-shallow junctions are

required in advanced microelectronic technologies. In PV industry, solar cell efficiency is controlled by the shape of the diode junction. The enhanced diffusion induced kink-and-tail features is generally seen while activated phosphorous dopants are driven into the bulk material under an adequate thermal budget. The relative study has been mentioned extensively in many semiconductor devices such as MOSFETs [169], a-Si:H / poly-silicon thin film transistors [170], InAlAs / InGaAs HEMT's [171], isolated-gate InAs / AlSb transistors [172] and so on to prove its importance to the electrical performance. Profiles without kink-and-tail distributions are generally modeled by an easier Gaussian distribution [173] and is not covered in this chapter.

A phosphorus liquid diffusion profile in silicon and the enhanced mechanism is well explained by Jones *et al.* [174], shown in Figure 6.1. In brief, the diffusivity of phosphorus acts as a vacancy dominated diffusion from the lattice mismatch between phosphorus and silicon, where enough thermal energy enables phosphorus atoms to jump between vacancies. In heavily doped ($X < X_0$) region, $(PV)^-$ pairs (P^+ ions pair with $V^=$ vacancies) are suppressed and proportional to the surface electron concentrations n. When $X > X_0$ ($n < 10^{20}$ cm^{-3}, the Fermi level is ~0.11eV from the conduction band), the dissociated $V^=$ vacancies from $(PV)^-$ pairs change their state with a decreased binding energy and enhance the vacancy flux to form the tail, mentioned by Fair and Tsai *et al.* [175]. The observed junction depth is therefore pushed deeper into the bulk material than people expect.

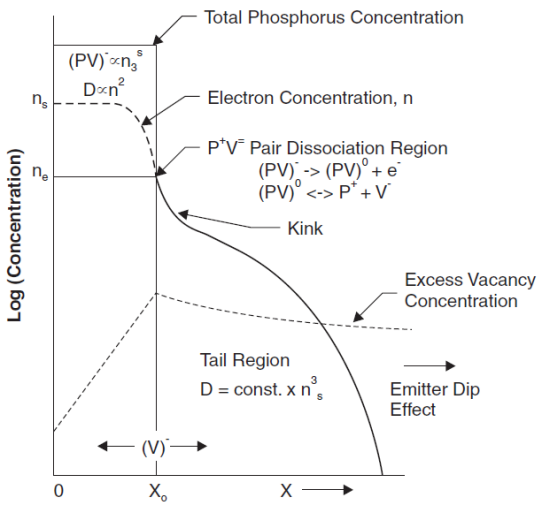

Figure 6.1 The example of a typical liquid diffusion profile in silicon [175].

6.2.3 Mathematical Models for Liquid Diffusion Profiles

In the transfer matrix, a doping profile is sliced into several segments to form a joint matrix and calculate a complex THz transmission. The finer profile mesh can enhance the modeling accuracy but also represents a bigger complexity in data fitting process. Therefore, using proper models to reduce the fitting complexity is beneficial. Either process or mathematical models can be utilized in reverse algorithms. Process models utilize instinctive process conditions as inputs, where mathematical models generally re-write relative equations and perform them with mathematical outlooks. For the entire study of liquid diffusion profiles, the mathematical model, proposed by Wirbeleit *et al.* [163], is chosen in this chapter. To study the degeneracy problem in other profile shapes, different mathematical models are necessary.

In Wirbeleit's paper [163], logarithmic function diffusion (LFD, equation 6.7) model, which is a solution of Fick's Law, is applied in the heavily doped region to depict the behavior of $(PV)^-$ pairs. In low- and medium-dopant concentration regions, rational function diffusion (RFD, equation 6.8) model is employed to represent self-diffusion and kick-out diffusion processes. A superposition of these two models (LFD+RFD) is proven in the paper [163] to

successfully describe various liquid diffusion profiles with kink-and-tail features. The beauty of using mathematical models is to represent infinite data points by limited parameters. Four parameters (a_1 (peak concentration) and x_1 (kink location) in LFD model and a_2 (kink concentration) and x_2 (junction depth) in RFD model) are utilized to construct liquid diffusion profiles for the study of the degeneracy problem in the following sections.

$$N_{heavy} = a * (b - \ln[e + x]) + d \tag{6.7}$$

$$N_{medium,low} = a * z^n + d; with\ z = \frac{b-x}{n-1}\ for\ n \neq 1 \tag{6.8}$$

6.2.4 Sample Fabrication for Experimental Demonstration

Although liquid diffusion profiles are studied in the entire modeling process, five distinct ion-implanted profiles are fabricated to experimentally display the existence of practical degeneracy under various profile features. The similar procedure, described in section 5.2.2, is applied here to produce these phosphorus profiles in bulk silicon wafers ($N \sim 10^{15}$cm^{-3}) instead of SOI wafers using 30keV implant energy, dosages 1×10^{15} / 2×10^{15} / 5×10^{15} / 1×10^{16}cm^{-2} and drive-in time RTP (rapid thermal annealing, 1.5min) / 60 min. 50-70nm sacrificial SiO_2 was grown to avoid the channel effect. Their SIMS (an upgraded Cameca IMS-4F from Qspec Inc.) profiles, shown in Figure 6.2, indicate much shallower junction depths (~300-400 nm) with only slightly kink-and-tail distributions in RTP samples and ~900 nm junction depth with a Gaussian distribution in the 60min sample. The kink-and-tail feature is expected to happen in certain amount thermal budget.

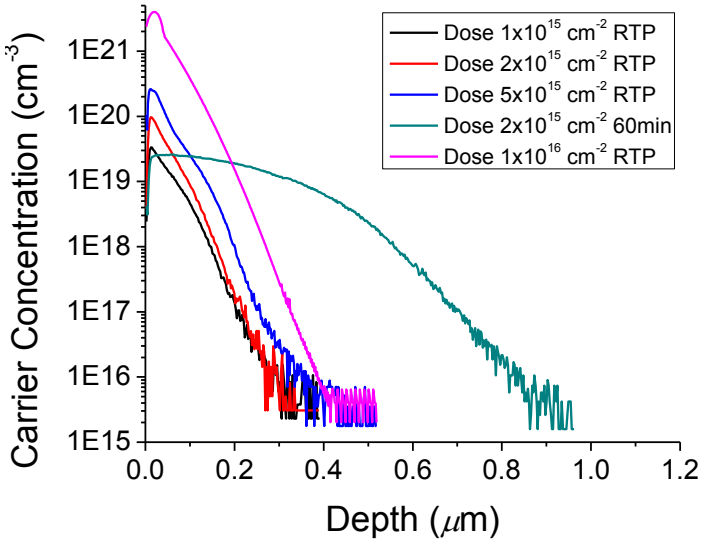

Figure 6.2 SIMS measured P_{31} profiles from five distinct samples using bulk silicon substrates.

6.3 Results and Discussion

The modeling of the multiple degeneracy is limited in the reasonable profile window formed by the LFD+RFD model to aim at the practical application in the PV industry. In Figure 6.3 (a), the feasibility of the LFD+RFD model is successfully tested by the ECV measured diffusion profile in a commercial mc-Si solar cell. In this reference profile, a_1, x_1, a_2 and x_2 are 20.2, 0.04, 19.4 and 0.18, respectively. To explain the multiple degeneracy, 4 distinct profiles with individual change in model parameters is set up to observe the impact to the complex THz transmission. The multiple degeneracy occurs when the transmission difference between two arbitrary profiles reaches zero. Figure 6.3 (b) indicate the possibility of the multiple degeneracy by seeing a close complex transmission to the reference profile (profiles with changes in a_2 and x_2). The modeling frequency here is from 0 to 8 THz, covering regions from photoconductive antennas and air plasma techniques. Sometimes the complex transmission can also be performed as the power ratio and phase shift, shown in Figure 6.3 (c), to amplify its difference. The

advanced study of the multiple degeneracy is started from the evaluation of the theoretical degeneracy. The transmission error is used in the entire modeling process through the equation 6.9.

$$T_{error} = \sum\left|Re(t_i) - Re(t_{ref,i})\right| + \sum\left|Im(t_i) - Im(t_{ref,i})\right| \quad (6.9)$$

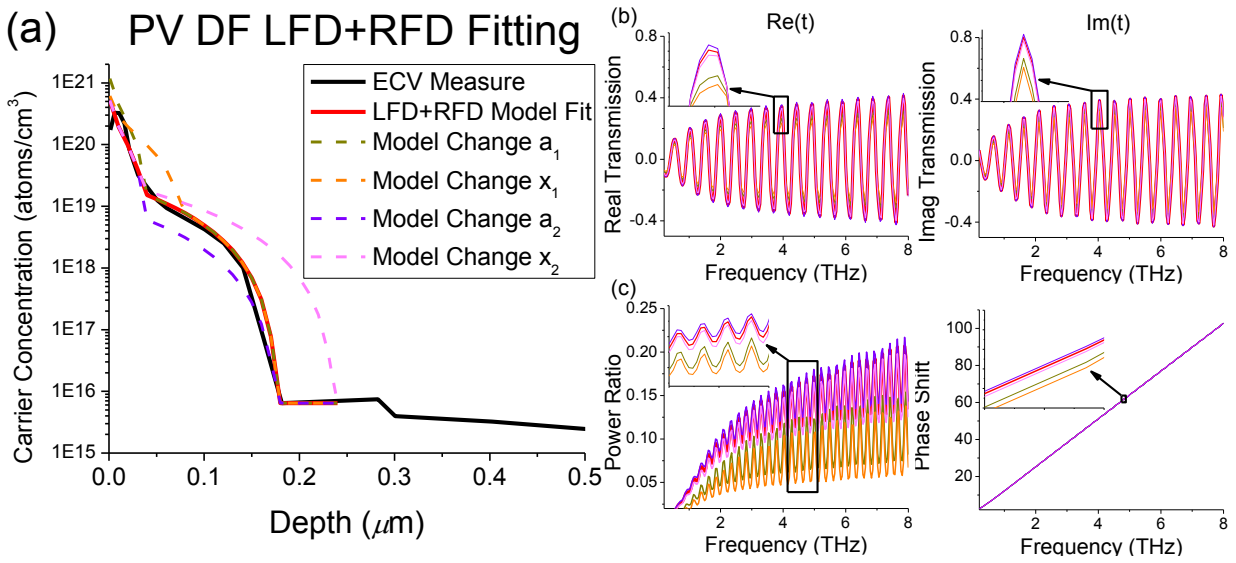

Figure 6.3 Schematic of the fitting of liquid diffusion profiles using LFD+RFD model. In (a), the black curve is the ECV measured profile from a commercial mc-Si solar cell and the red curve is the fitting result using LFD+RFD model. In the reference profile, a_1, x_1, a_2 and x_2 are 20.2, 0.04, 19.4 and 0.18. Four other profiles (green, orange, purple and pink curves) are example profiles with changes in a_1, x_1, a_2 and x_2. (b) compares simulated complex transmissions between the reference profile (red curve) and profiles with model parameter changes (green, orange, purple and pink curves). (c) shows the difference in power ratio and phase shift.

6.3.1 Evaluation of Theoretical Degeneracy

To not study just one example, another reference profile in the given window (a_1=19.6 a_2=18.8 x_1=0.08, x_2=0.18) is utilized to study the theoretical degeneracy in the free space, coving individual parameter (1-D) to combined parameters (4-D) in sequence.

6.3.1.1 Study in One Dimension

a_1 between 18.6 to 20.6, x_1 between 0.05 to 0.15, a_2 between 17.5 to 19.5 and a_2 between 0.13 to 0.23 are defined as the parameter window of the LFD+RFD model in the whole modeling

process. While simulating the transmission difference in individual parameter, other parameters are defined as the same value to the reference profile. In Figure 6.4 (a), a_1 is swept in the given window to calculate the transmission difference to the reference point. The same procedure is applied to complete Figure 6.4 (b-d). The practical mesh size has been defined to guarantee the modeling accuracy, where 2.5nm is used in x_1 and x_2 and twenty segments are utilized in each order of a_1 and a_2. The mission is to not only verify the existence of the theoretical degeneracy, but also understand the sensitivity of individual parameter in a doping profile prediction. All four parameters indicate only one zero transmission difference at the reference point and the difference keeps increasing at both sides from the reference profile in the given window. Figures in the right column show how profiles change individually in the given window. The exclusion of the theoretical degeneracy is therefore confirmed from above observation. On the other hand, magnitudes of transmission differences (Y-axis) in a_1, x_1, a_2 and x_2 are 0→55, 0→16, 0→2.8 and 0→0.9, respectively. Therefore the parameter sensitivity is expected to be $a_1 > x_1 > a_2 > x_2$.

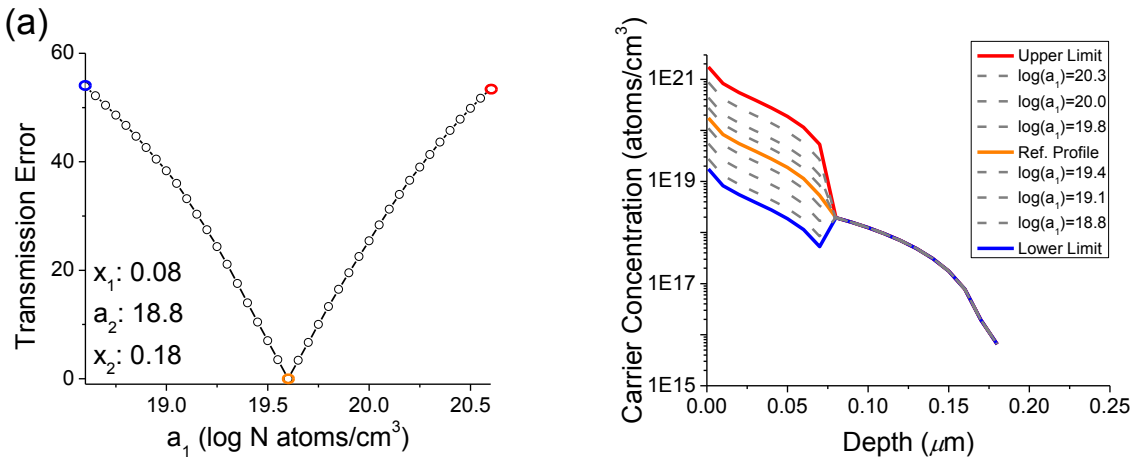

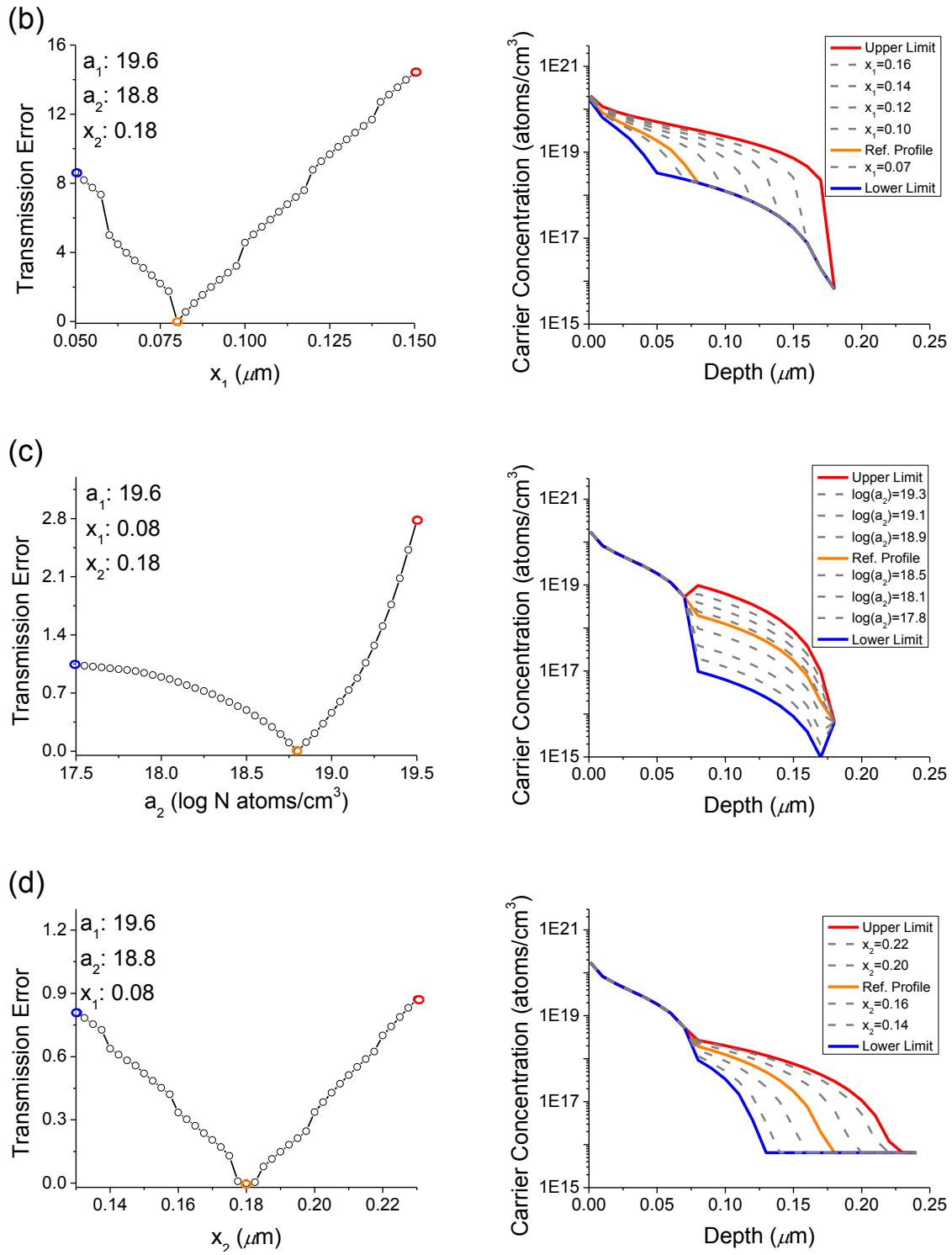

Figure 6.4 Complex transmission error (the superposition of the difference of complex transmission to the reference point) vs a) surface concentration a_1 in log b) penetration depth x_1 c) kink point concentration a_2 in log and d) junction depth individually. At the reference point, x_2. a_1, x_1, a_2 and x_2 are 19.6, 0.08, 18.8 and 0.18, respectively.

6.3.1.2 Study in Other Dimensions

The continuous study starts from two dimensions and ends at four dimensions, covering the possibility from all four parameters. In two dimensions, six combinations (a_1-x_1, a_1-a_2, a_1-x_2, x_1-a_2, x_1-x_2, a_2-x_2) can be generated to study. The example investigation using a_1-x_1 (a_2 and x_2 are assumed to be 18.8 and 0.18) is performed in Figure 6.5 (a), where results in other combinations are similar. The theoretical degeneracy exists only by seeing another zero transmission difference other than the reference point in the given matrix. a_1 from 18.3-20.3 as well as x_1 from 0.05 to 0.15 are defined to generate a transmission difference matrix with proper intervals (a_1 interval 0.1 and x_1 interval 0.01 (10 nm)). Within this matrix, two locations with smallest but not zero transmission differences (a_1-x_1: 19.7-0.06 with difference 1.323, 19.5-0.11 with difference 0.731) are found and zero difference is expected somewhere around these locations by searching in advanced. While zoom-in the area surrounding the point (a_1-x_1: 19.5-0.11) and varying x_1 with 0.1 to 1 nm as well as a_1 with 0.01 to 0.0001 intervals, the difference keeps decreasing and the location with the smallest difference 0.163 is found eventually (see Figure 6.5 (a), Number 1 to 5). The potential of finding zero difference is displayed through this sequence and there is no way to get a smaller value nearby that location. Therefore the conjecture is the exclusion of the theoretical degeneracy in two dimensions.

Three dimensions involve the searching of zero transmission difference through the change of three parameters at the same time. In is observed that the location (a_1: 19.5, x_1: 0.11445, a_2: 18.79), which is nearby the last location in the two dimensions case, still give us a smallest but not zero difference (0.162) to exclude the theoretical degeneracy and the same result (0.156) is found at four dimensions case. Since the location (a_1: 19.5, x_1: 0.11445, a_2: 18.79, x_2: 0.1799) already gives us the smallest difference at that area, we conjecture that the theoretical

degeneracy doesn't exist in given space through above study. The relative profiles from parameters listed in Figure 6.5 (a) are shown in Figure 6.5 (b) for the reference. Two distinct profiles can potentially have a very close complex transmission but won't be exact the same.

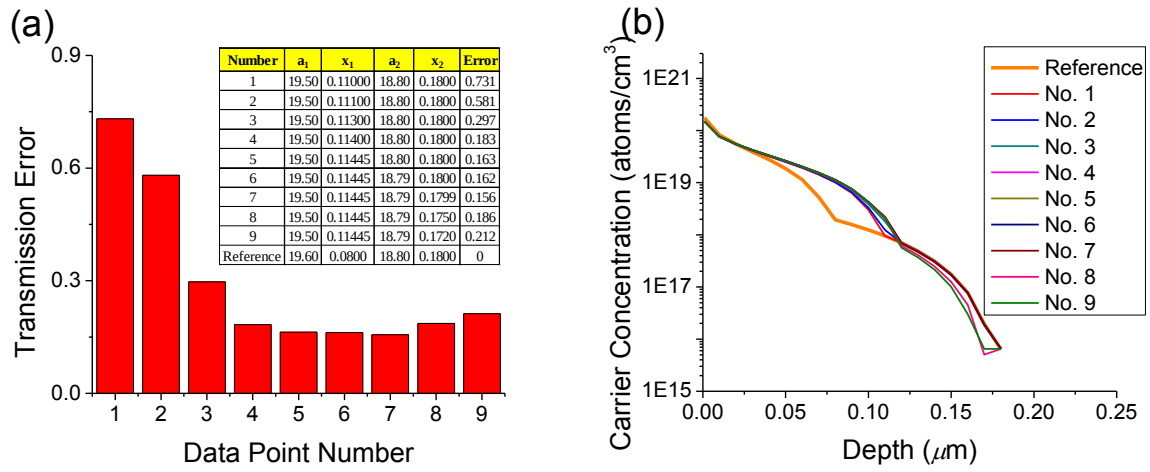

Number	a_1	x_1	a_2	x_2	Error
1	19.50	0.11000	18.80	0.1800	0.731
2	19.50	0.11100	18.80	0.1800	0.581
3	19.50	0.11300	18.80	0.1800	0.297
4	19.50	0.11400	18.80	0.1800	0.183
5	19.50	0.11445	18.80	0.1800	0.163
6	19.50	0.11445	18.79	0.1800	0.162
7	19.50	0.11445	18.79	0.1799	0.156
8	19.50	0.11445	18.79	0.1750	0.186
9	19.50	0.11445	18.79	0.1720	0.212
Reference	19.60	0.0800	18.80	0.1800	0

Figure 6.5 Complex transmission error vs all four variables. At the reference point, x_2. a_1, x_1, a_2 and x_2 are 19.6, 0.08, 18.8 and 0.18, respectively. (a) Example data points to indicate the sequence of finding another "zero error" point. The minimum error point is found at number 7 but still not zero. The theoretical degeneracy is therefore excluded. (b) All doping profiles generated from parameters in figure (a).

6.3.2 Evaluation of Practical Degeneracy

Although the theoretical degeneracy is excluded in the previous section, measurement noise always happens in the real life to mess up the accuracy of the prediction, called "Practical Degeneracy". To deal with this uncertainty, the elimination of the measurement noise through THz-TDS optimizations and system developments is essential. The average measurement uncertainty between 0.3 – 1.3 THz through the repeated measurements gave us an idea to define the threshold value for the practical degeneracy. Laser type and daily condition, THz-TDS alignment, sample placement, humidity and so on are all possible reasons to cause this uncertainty. While considering a broader frequency bandwidth from 0 to 10 THz through the air plasma THz system, the threshold value is assumed around 3.7 in the later study.

6.3.2.1 Study in One Dimension

How the measurement uncertainty impacts the model parameter individually can be studied by scaling the area above the threshold value 3.7 in Figure 6.4. Parameter a_1 shows the smallest impact by having most of the area above this value. For x_1, the influence is bigger because the bigger area is already below this threshold value. Parameters a_2 and x_2 perform devastating impacts by not having areas survived from this value. This result tells us that the profile prediction is only feasible at heavily doped regions under current threshold value. Technology breakthrough and careful system maintenance are vital to extend the profile prediction to lightly doped regions.

6.3.2.2 Study in Two Dimensions

In two dimensions case, the value 3.7 is applied in all matrices of section 6.3.1.2 and four selected combinations are displayed in Figure 6.6 as representatives. Blue to green regions disclose profiles with transmission differences smaller than the threshold value, where red dot is the same reference profile. Parameters in orange regions, on the other hand, present detectable profiles under current threshold value. The slope of the band in the contour plot indicates the domination of the parameter in different combination and the slope of the valley shows the resolution of profile prediction. In a_1 relative combinations (see Figure 6.6 (a)(b)), steeper valleys are observed in the a_2, and x_1 directions to confirm a higher resolution from the change in a_1, compared to other two parameters. The narrow the band is, the better the resolution of profile prediction is. Each combination contains four figures to deliver the message. The bottom two figures identify the detectable profile boundaries under current threshold value in both axes. In the a_1-x_1 group, which represents the heavily doped regions, profiles outside the small enclosed area are detectable. In contrast, much bigger enclosed area in a_2 (see Figure 6.6 (b)) shows a poor system resolution in the lightly doped regions. The same conclusion can be made by looking at

x_1-a_2 and a_2-x_2 groups, shown in Figure 6.6 (c-d). These two combinations also display the relatively poor resolution in the lightly doped regions. Therefore, the threshold value can determine the number of parameters to use and the lower concentration limit of the profile to distinguish in the inverse fitting process. Smart fitting algorithms, system breakthrough and optimizations are all essential helpers to eliminate the practical degeneracy.

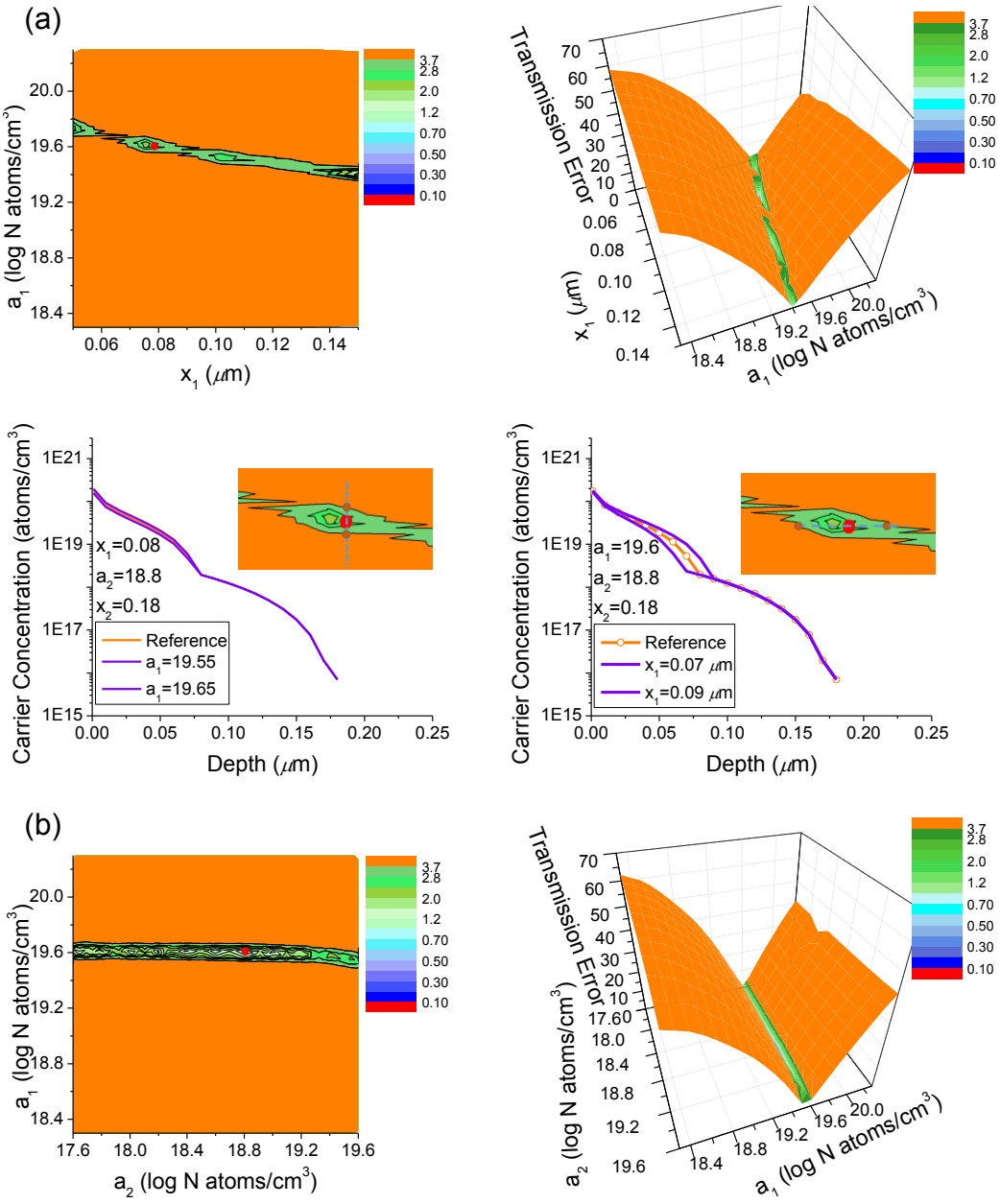

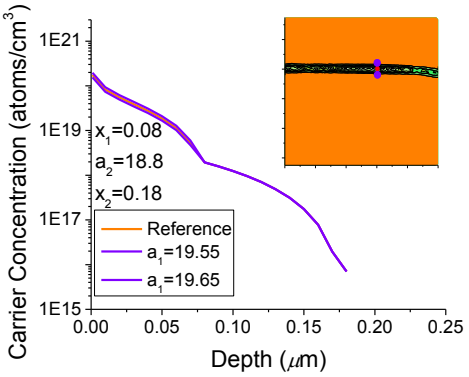
Carrier Concentration (atoms/cm^3)
1E21
1E19
1E17
1E15
0.00
0.05
0.10
0.15
0.20
0.25
Depth (μm)
x_1=0.08
a_2=18.8
x_2=0.18
Reference
a_1=19.55
a_1=19.65

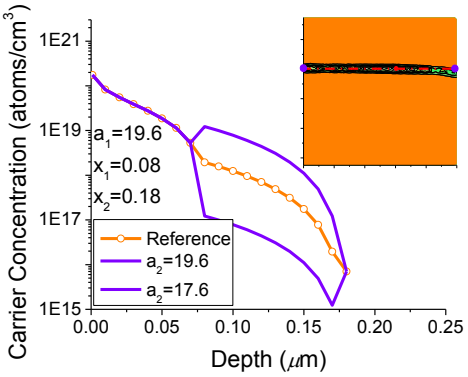
Carrier Concentration (atoms/cm^3)
1E21
1E19
1E17
1E15
0.00
0.05
0.10
0.15
0.20
0.25
Depth (μm)
a_1=19.6
x_1=0.08
x_2=0.18
Reference
a_2=19.6
a_2=17.6

(c)

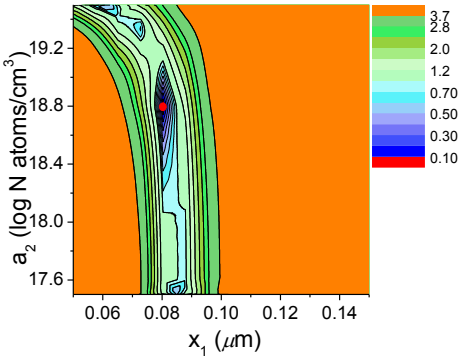
a_2 (log N atoms/cm^3)
19.2
18.8
18.4
18.0
17.6
0.06
0.08
0.10
0.12
0.14
x_1 (μm)
3.7
2.8
2.0
1.2
0.70
0.50
0.30
0.10

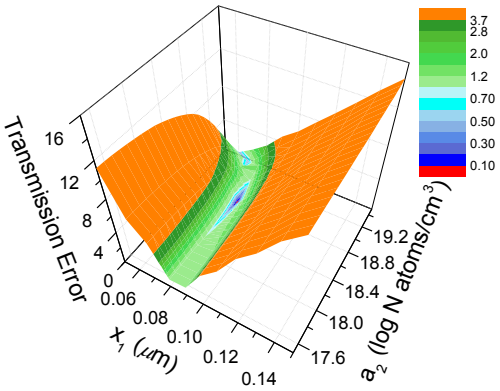
Transmission Error
16
12
8
4
0
0.06
0.08
0.10
0.12
0.14
x_1 (μm)
17.6
18.0
18.4
18.8
19.2
a_2 (log N atoms/cm^3)
3.7
2.8
2.0
1.2
0.70
0.50
0.30
0.10

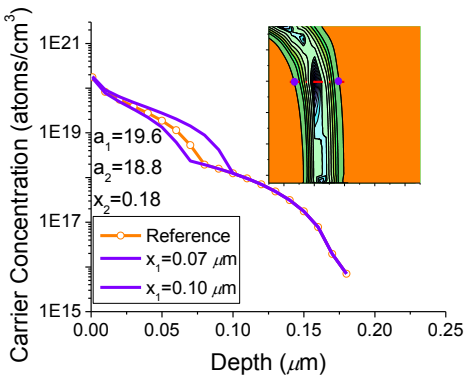
Carrier Concentration (atoms/cm^3)
1E21
1E19
1E17
1E15
0.00
0.05
0.10
0.15
0.20
0.25
Depth (μm)
a_1=19.6
a_2=18.8
x_2=0.18
Reference
x_1=0.07 μm
x_1=0.10 μm

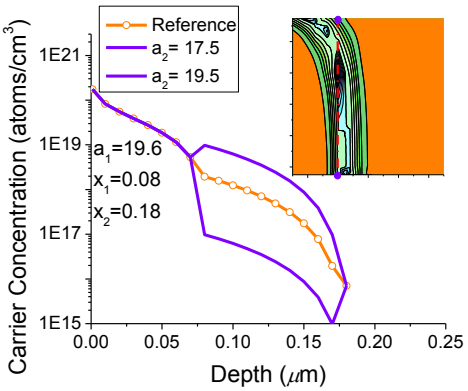
Carrier Concentration (atoms/cm^3)
1E21
1E19
1E17
1E15
0.00
0.05
0.10
0.15
0.20
0.25
Depth (μm)
Reference
a_2= 17.5
a_2= 19.5
a_1=19.6
x_1=0.08
x_2=0.18

(d)

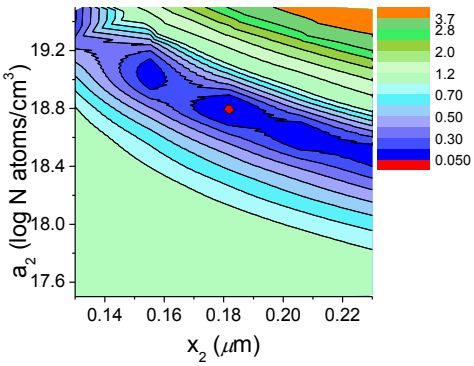
a_2 (log N atoms/cm^3)
19.2
18.8
18.4
18.0
17.6
0.14
0.16
0.18
0.20
0.22
x_2 (μm)
3.7
2.8
2.0
1.2
0.70
0.50
0.30
0.050

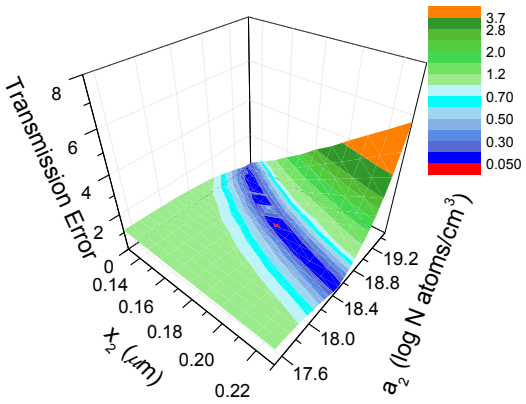
Transmission Error
8
6
4
2
0
0.14
0.16
0.18
0.20
0.22
x_2 (μm)
17.6
18.0
18.4
18.8
19.2
a_2 (log N atoms/cm^3)
3.7
2.8
2.0
1.2
0.70
0.50
0.30
0.050

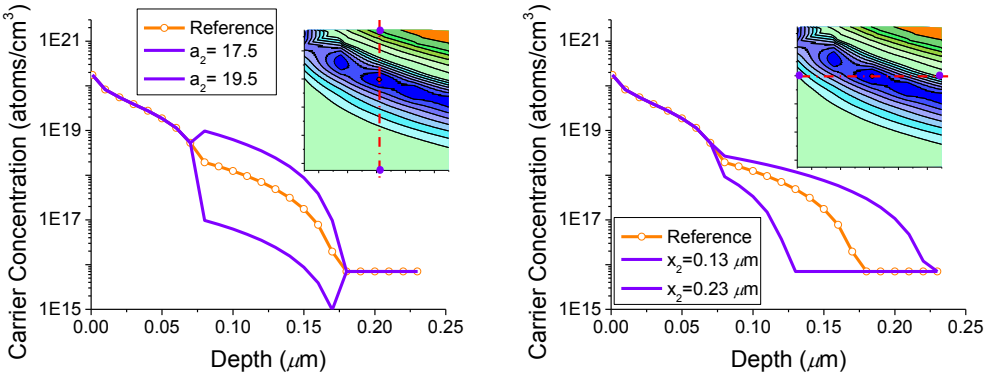

Figure 6.6 Complex transmission error vs group variables. Four groups, a_1-x_1 (a), a_1-a_2 (b), x_1-a_2 (c) and a_2-x_2 (d), are chosen to represent and each group contains four figures. The threshold value (red circles) is determined as 3.7 based on the repeated measurement and errors above this value are defined as orange color. The upper two figures are contour and 3D plots, which indicate trends between transmission errors and group variables. The bottom-left figures show non-detectable profiles along with the change in the x-axis parameter and bottom-right figures are based on the change in the y-axis parameter.

6.4 Experimental Demonstration of Practical Degeneracy

Since the practical degeneracy is expected to exist in all kinds of profile shapes, five distinct ion-implanted profiles are used to experimentally demonstrate the practical degeneracy and its existence in various profile shapes. Figure 6.7 (a) displays the schematic of the experimental design and all profiles measured by SIMS are shown again in Figure 6.7 (b). Among these five profiles, the 5×10^{15} RTP is chosen sample as the reference profile (red dot) and 2×10^{15} 60 min sample is expected to cause the practical degeneracy based on the TCAD simulation. Other three profiles should have transmission differences in the orange region. Figure 6.7 (c) describes measured complex transmissions from all five samples up to 1.2 THz. Four RTP samples indicate that higher implanted dosages increase the THz absorption to reduce the complex transmission. On the other hand, the complex transmission from the 2×10^{15} 60min sample performs a very close behavior (dark cyan curve) between 0.2 – 1.2 THz to the reference profile (black curve). The existence of the practical degeneracy is therefore proven. In Figure 6.7 (d), successful predictions of complex transmissions on two selected samples are demonstrated

through the comparison to THz measurements up to 1.2 THz. The same empirical refractive index library from Chapter 5 applied in the whole modeling process conjectures the accuracy of the simulation result to 8 THz. In 0.2 – 1.2 THz regions, the practical degeneracy exists on 5×10^{15} RTP and 2×10^{15} 60min samples (see Figure 6.7 (c)). Is it possible to break the practical degeneracy by just having broader bandwidth information? Figure 6.7 (e) shows simulated complex transmissions of all five profiles up to 8 THz. There is no significant shape change observed at higher frequency regions to break the practical degeneracy. The major difference still come from the magnitude change of resonant peaks.

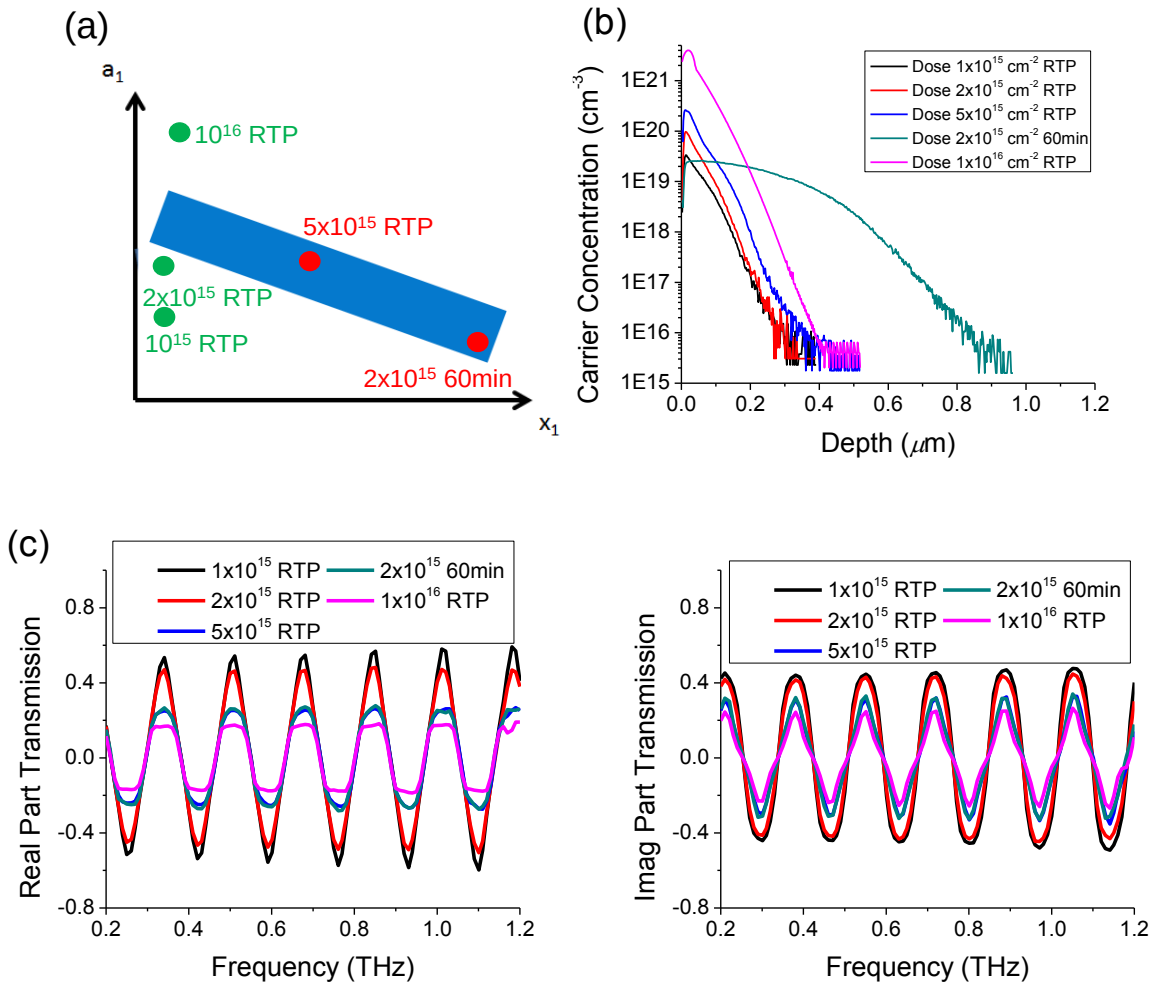

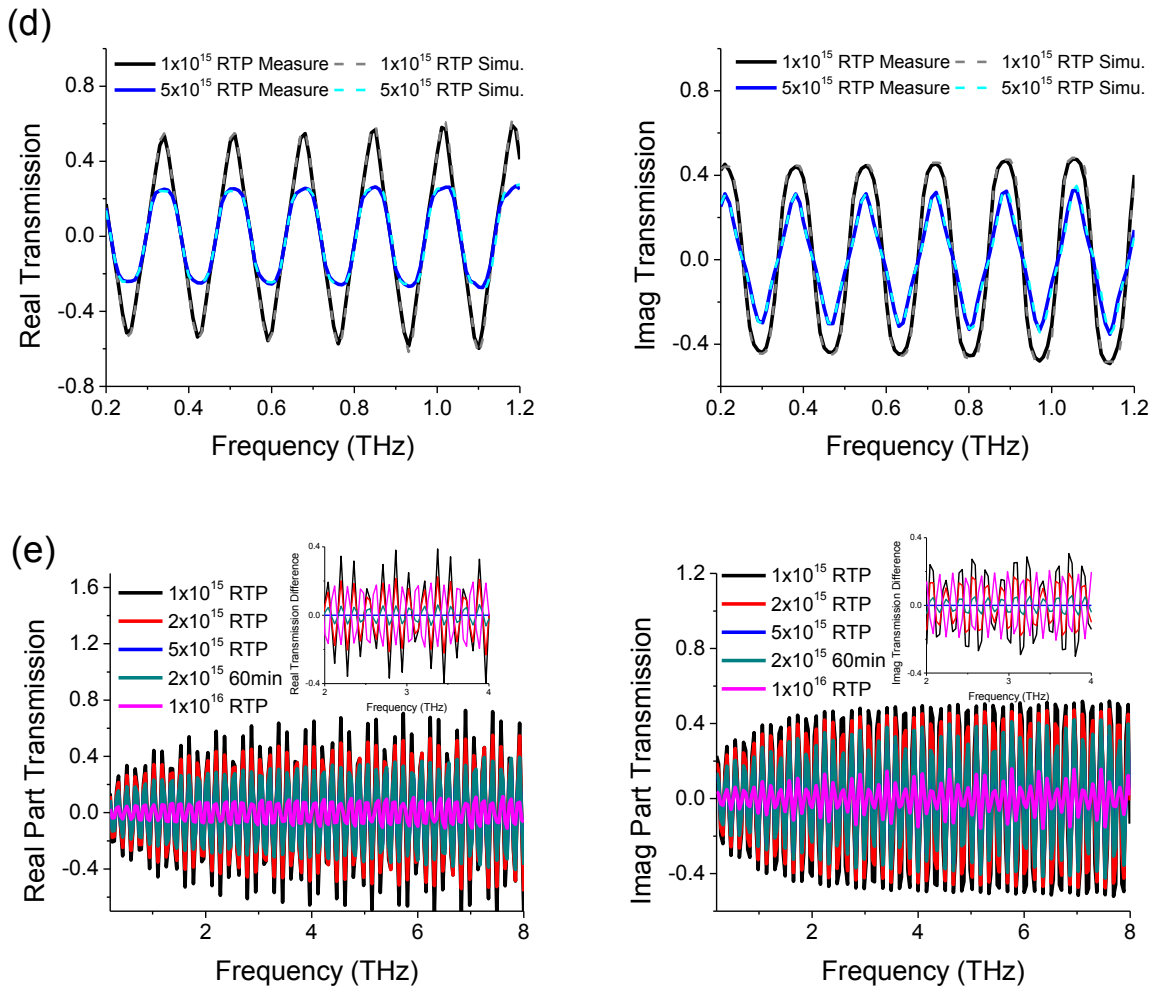

Figure 6.7 (a) The design of experiment of the demonstration of practical degeneracy using 5 distinct profiles (b) SIMS measured profiles of all designed samples. (c) Measured complex THz transmission of all samples with frequencies up to 1.5 THz (d) Benchmark of THz measurements (solid lines) and Drude Model simulations (dash lines) on selected 1×10^{15} RTP and 5×10^{15} RTP samples. Drude model predictions agree with THz measurements well. (e) Simulated complex THz transmission of 5 samples with frequencies up to 8 THz. Measured and simulated complex THz transmissions agree to each other in the beginning 1.5 THz region. The small insets indicate the difference of complex transmissions from all samples to the reference sample 5×10^{15} RTP in 2 to 4 THz regions. The difference between 5×10^{15} RTP and 2×10^{15} 60min samples are much smaller than ones from other samples.

6.5 Methods to Shrink or Break Practical Degeneracy

After proving the existence of the practical degeneracy, the next step is to break or shrink the practical degeneracy. Except using just a transmission mode THz-TDS, the information from reflected THz measurements is taken into the consideration. In Fig. 6.8, simulated complex

reflections indicate a significant difference on 5×10^{15} RTP and 2×10^{15} 60min samples. The zoom-in information in Fig. 6.8 (b) clearly displays this bigger difference, compared to a much smaller one in Fig. 6.7 (c). Although the major difference still come from the magnitude change, this preliminary simulation already brings us the attention to consider it as the way to break the practical degeneracy. This could be an important topic to study once a reflection THz system is set up in our lab. For now, it is expected that the practical degeneracy in the fitting process can be shrunk or broken by utilizing both complex transmission and reflection information at the same time.

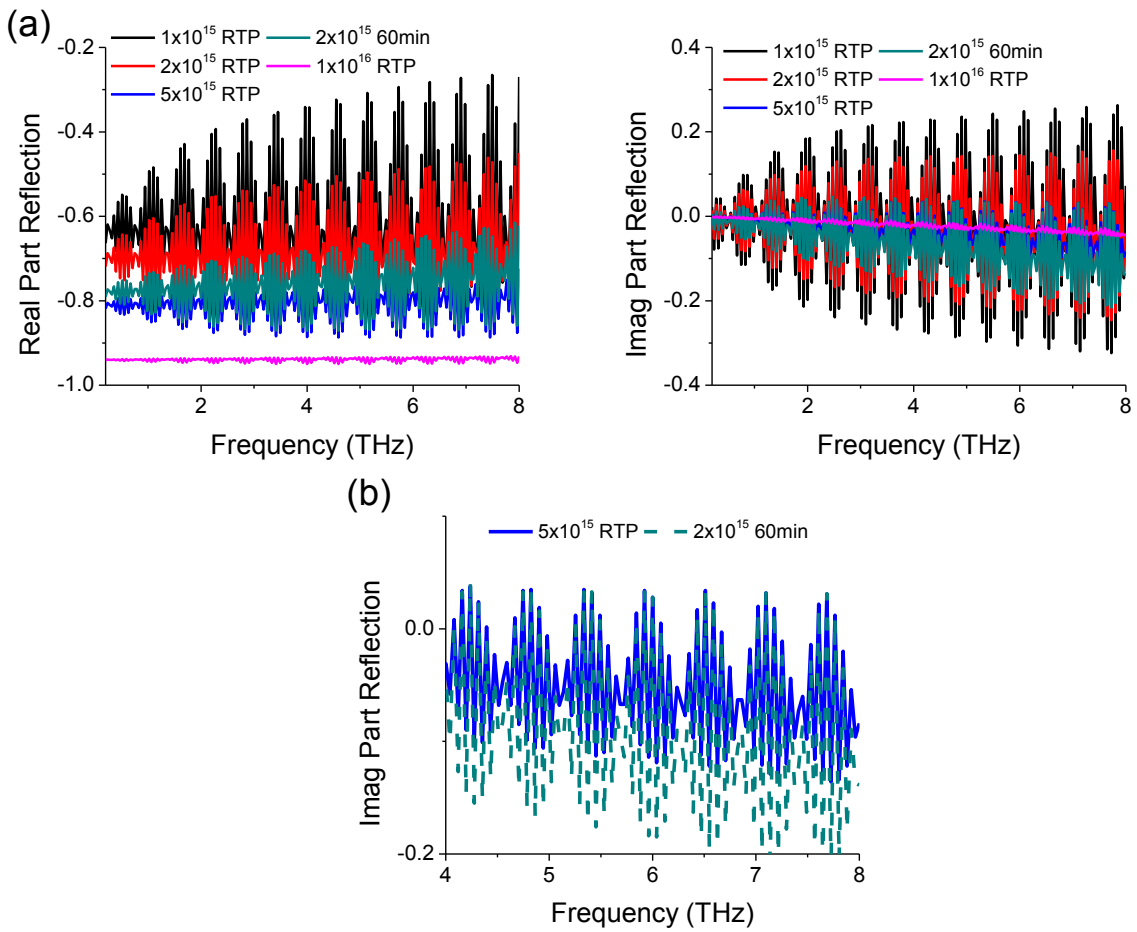

Figure 6.8 (a) Simulated complex reflection of five samples to 8 THz. Complex reflections between samples are unique. (b) Benchmark of zoom-in imaginary reflections between 5×10^{15} RTP and 2×10^{15} 60min samples at 6 to 8 THz regions. A detectable reflection difference can be observed.

6.6 Conclusions

In this chapter, liquid diffusion profiles with kink-an-tail features are mathematically modeled by the LFD+RFD model [163] to study the multiple degeneracy. Theoretical degeneracy happens to lead a wrong profile prediction when multiple profiles share the same complex transmission. Drude model [60], empirical ASTM [152], carrier mobility [165, 166] as well as the LFD+RFD model [163] are utilized to exclude the theoretical degeneracy but indicate the existence of the practical degeneracy from measurement noise. To prove its existence experimentally in different profile shapes, THz measurements were done on five distinct ion implanted profiles and a less than measurement uncertainty difference was found on 5×10^{15} RTP and 2×10^{15} 60min samples. While using the LFD+RFD model, the sensitivity sequence of parameters is determined to be $a_1 > x_1 > a_2 > x_2$. Less sensitive parameters increase the difficulty to break the practical degeneracy. The repeated measurement indicate ~3.7 measurement uncertainty between 0-10 THz regions. Except the technology breakthrough and system optimization, the reflection mode system setup is simulated to create a detectable difference on 5×10^{15} RTP and 2×10^{15} 60min samples. Utilizing both transmission and reflection THz information could be the potential solution to break or shrink the practical degeneracy.

7 EXPERIMENTAL DEMONSTRATION OF DOPING PROFILE PREDICTION USING TERAHERTZ TIME DOMAIN SPECTROSCOPY

After collecting all essential information and excluding the theoretical degeneracy, two conceptual demonstrations of the doping profile prediction are performed experimentally. In this chapter, the accuracy of the empirical refractive index library from Chapter 5 is firstly calibrated using various SIMS profiles, followed by the demonstration of the doping profile prediction in both destructive and non-contact manners, targeting the design of the stand-alone system and the *in-situ* process monitor. Two manuscripts (Part I & II) based on the revised content are under preparation and submissions are scheduled to the journal "*Terahertz Science and Technology, IEEE Transactions on*" in 2014.

7.1 Introduction

The original goal in this research is to achieve just a non-contact doping profile prediction using THz-TDS. Then the operation procedure from ECV motivated us to research the possibility of a destructive doping profile prediction, which might be an easier way to carry out the research goal using THz techniques. In the destructive measurement, both the carrier concentration and junction depth is determined with a potentially higher resolution than other existing techniques of measuring the same electrical profiles. The key component to succeed the destructive profile measurement is to own the capability of a controllable material removal. The anodic oxidation was incorporated in this chapter to perform the silicon removal layer by layer with a proven thickness control. Other competing techniques such as CMP can be alternative

options to consider. Since SIMS does such a good job in the destructive doping profile measurement, a cheaper system cost might be the only chance of using THz-TDS. However, the mainstream technique for a non-contact profile measurement is not solid yet. Currently in the industry the test key designed for the resistance measurement is used to monitor the diffusion and implant process electrically and people don't really look at the real profile change in detail when a process variation happens. The profile estimation in the real time process monitor can greatly help engineers employ the process compensation in later stages, which motivates us to start-up this novel research using THz techniques.

In previous chapters, we collected all essential information and excluded the existence of the theoretical degeneracy. The main task now becomes the conceptual demonstration of the final goal. Prior to that, the accuracy of the phosphorus refractive index library from Chapter 5 is cross checked and proven by various SIMS profiles. The new derived equation of modeling the complex transmission from the first two peaks is selected in the following demonstration since our real THz measurement only contains information from the first two peaks. The first experimental demonstration is done in a destructive manner. The promising result indicates that the anodic oxidation technique did a good job to remove silicon uniformly and the electrical doping profile was reversely constructed through the repeated determination of profile segments. In the non-contact profile prediction, the proposed fitting strategy was practiced using distinct SIMS profiles and close prediction results were successfully achieved on one chosen profile, no matter what initial guess profiles were used. Many following researches can be done to improve the fitting performance. The programming work as well as the development of commercial systems are left as future work and a patent (RIT ID: 2013-016) is filed to cover the whole research.

7.2 Material and Methods

7.2.1 Sample Preparation and Anodic Oxidation

The detail information regarding the sample preparation for the non-contact profile prediction has been described in Chapter 6. The doping profile for the destructive measurement was made in a regular silicon wafer (CZ, 475-575 μm, boron-doped, (100), 10-25 Ω-cm) with similar processes described in the section 4.3.1. The dosage 5×10^{15} atoms/cm^2, energy 60keV and 1000 ºC RTP were adopted to create the unique profile feature. The resulting doping profile was confirmed by SIMS from Qspec Inc. as the black curve with ±5% measurement uncertainty, shown in Figure 7.1 (a). The schematic of the anodic oxidation system can be found in the work of Tiwald *et al.* [176] as well as Panagopoulos *et al.* [177] and the experimental setup is summarized below. The electrolysis cell consisted of a 500 ml electrolyte solution (90 % ethylene glycol (EG), 10 % deionized water (DI) and a salt, potassium nitrate of 0.5M) and two alligator clips. One clip from positive output of the constant voltage source was attached to the silicon (anode) sample, whereas another one was attached to platinum foil (cathode). Both electrodes were then immersed in the electrolyte to process the oxide growth. The solution was agitated during the whole process to increase the film uniformity. The oxide growth was determined by time, current and voltage applied. In the experiment, we controlled the power supply at constant voltage 120V and varied the time to achieve targeted oxide thickness. The result indicated that time spanning from 5-10 minutes resulted in oxide thickness from 50 nm – 90 nm (~10 nm/min). To protect the back side of the specimen from oxidation, the sample was wrapped by another silicon sample with ~1.2 μm oxide during the whole process. Total thirteen cycles (20, 40, 60, 80, 100, 130, 160, 170, 200, 220, 240, 260 and 320 nm Si removal thickness) were done in separated samples, covering the thickness range from 20 to 320 nm with ~±2-8 nm thickness variation, detected by Rudolph IV Ellipsometer. The successful oxidation was

confirmed by seeing the sheet resistance change between samples, measured by CDRES MAP (see Figure 7.1 (a)). Oxide films was then removed by the buffer oxide etch (BOE) solution (ammonium fluoride, hydrofluoric acid in 10:1) to start the THz measurement. The schematic of achieving a cycle etched THz measurement is described in Figure 7.1 (b).

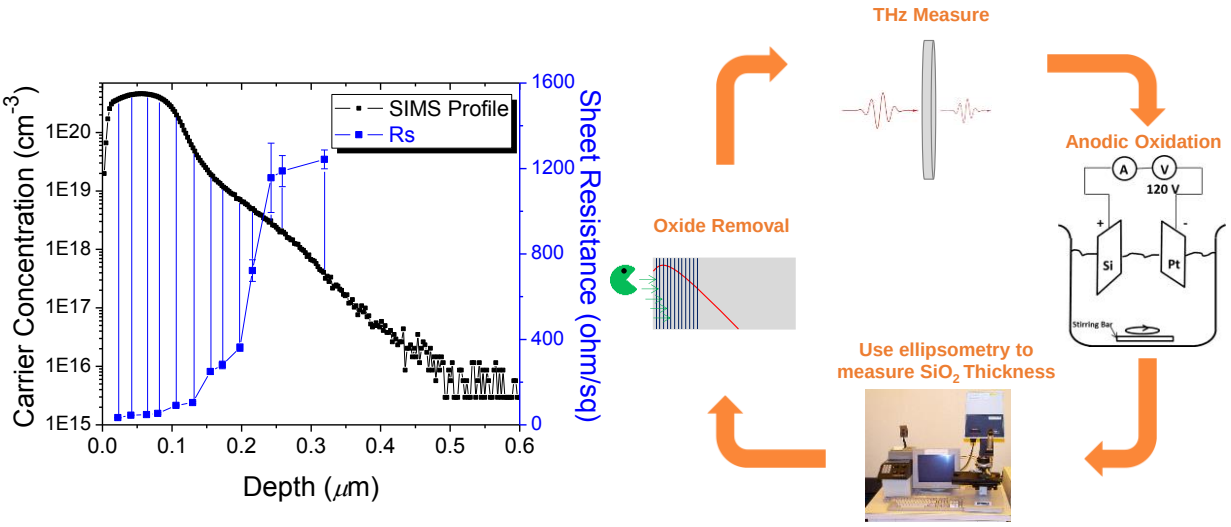

Figure 7.1 (a) Anodic oxidation thicknesses vs Rs (Ω/sq) of all 13 cycles with ~±2-8 nm thickness uncertainty. Black curve indicates the as-implanted profile measured by SIMS. (b) Schematic of the destructive doping profile construction.

7.2.2 Equation for the Accurate Estimation of Complex THz Transmission

In our THz measurement, the typical time region is selected from -10 to 35 ps, covering the main absorption peak and 1st internal reflection peak. The introduced equation in section 2.3.3 calculates the THz transmission by assuming the information from an infinite time region. To precisely describe the information from a real measurement, a new equation to simulate the THz transmission from the first two peaks was derived based on the equation for the infinite peaks and is displayed in Figure 7.2. Its mathematical derivation in detail is summarized in the appendices. In the new equation, the formula for THz transmission in individual peak is derived and the overall transmission is obtained from the superposition of the first two peaks ($\frac{\widetilde{E_T}}{\widetilde{E_0}} = \frac{\widetilde{E_{T_1}}}{\widetilde{E_0}} +$

$\frac{\widetilde{E_{T_2}}}{\widetilde{E_0}}$). $\frac{\widetilde{E_{T_1}}}{\widetilde{E_0}}$ is the transmission from the main peak, where $\frac{\widetilde{E_{T_2}}}{\widetilde{E_0}}$ represents the transmission from the 1st internal reflection peak. Air scan is adopted as the reference $\widetilde{E_0}$ in this equation to calculate the transmission ratio. While working on the DFT, a time region containing only two peaks needs to be defined carefully. Similar like the single peak equation in section 5.2.5, two steps process is required in the whole calculation. n_{sub} needs to be determined firstly in the step 1 and then applied as the known component in the step 2. The same derivation for $\frac{\widetilde{E_{T_2}}}{\widetilde{E_0}}$ can be employed to obtain the following 2nd, 3rd …to infinite transmissions by adding terms to represent extra traveling paths. There is only a necessity for this if more peaks are collected in a THz measurement.

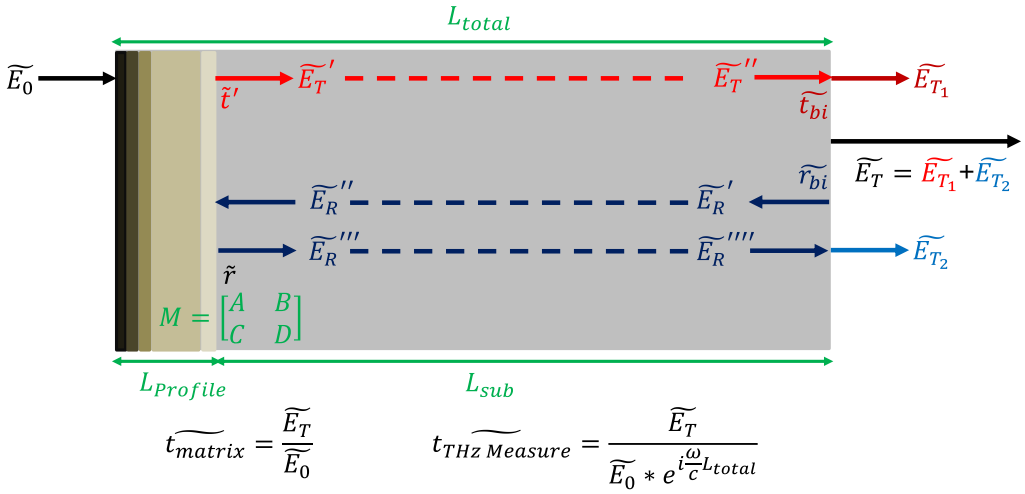

$$\frac{\widetilde{E_{T_1}}}{\widetilde{E_0}} = \frac{2}{A + Bn_{sub} + C + Dn_{sub}} \frac{2n_{sub}}{n_{sub} + 1} e^{i\frac{n_{sub}\omega}{c}L_{sub}}$$

$$\frac{\widetilde{E_{T_2}}}{\widetilde{E_0}} = \frac{2n_{sub}}{n_{sub} + 1} \frac{An_{sub} + Bn_{sub} - C - D}{An_{sub} + Bn_{sub} + C + D} \frac{n_{sub} - 1}{n_{sub} + 1} \frac{2}{A + Bn_{sub} + C + Dn_{sub}} e^{i\frac{3n_{sub}\omega}{c}L_{sub}}$$

$$\frac{\widetilde{E_T}}{\widetilde{E_0}} = \frac{\widetilde{E_{T_1}}}{\widetilde{E_0}} + \frac{\widetilde{E_{T_2}}}{\widetilde{E_0}}$$

Figure 7.2 The new derived equation to calculate the THz transmission from a THz measurement containing just the first two peaks in the time domain.

7.3 Results and Discussion

The accuracy of the empirical refractive library is firstly calibrated through the new derived equation and then used in the entire demonstration to estimate the performance of the doping profile prediction.

7.3.1 Calibration of Empirical Refractive Index Library

An accurate refractive index library directly determines the profile prediction performance and its resolution. To process the library calibration, various SIMS measured doping profiles and the empirical library are utilized to calculate the complex THz transmission from the transfer matrix through the forward simulation and resulted transmissions are benchmarked with their THz measurements to evaluate offset levels. Figure 7.3 sketches complex transmissions and power ratios between the THz measurement and library prediction from four different samples. Compared to the measurement uncertainty studied in Chapter 6, offsets between library predictions and THz measurements in Figure 7.3 (e) are all acceptable in four profiles. One interesting observation is that complex transmissions in lighter THz absorption profiles switch their shapes in heavier THz absorption profiles (the shape of the real part transmission in Figure 7.3 (a) and the imaginary part transmission in Figure 7.3 (c) are alike) but the behind theory is not clear yet. On the other hand, the power ratio difference between 5×10^{15} RTP and 2×10^{15} 60min samples looks bigger than that in Figure 6.12. This offset can be reasonably interpreted by the measurement uncertainty. Since the library predicted complex transmission is so close to the THz measurement, we conclude that the accuracy of the generated refractive index library is acceptable.

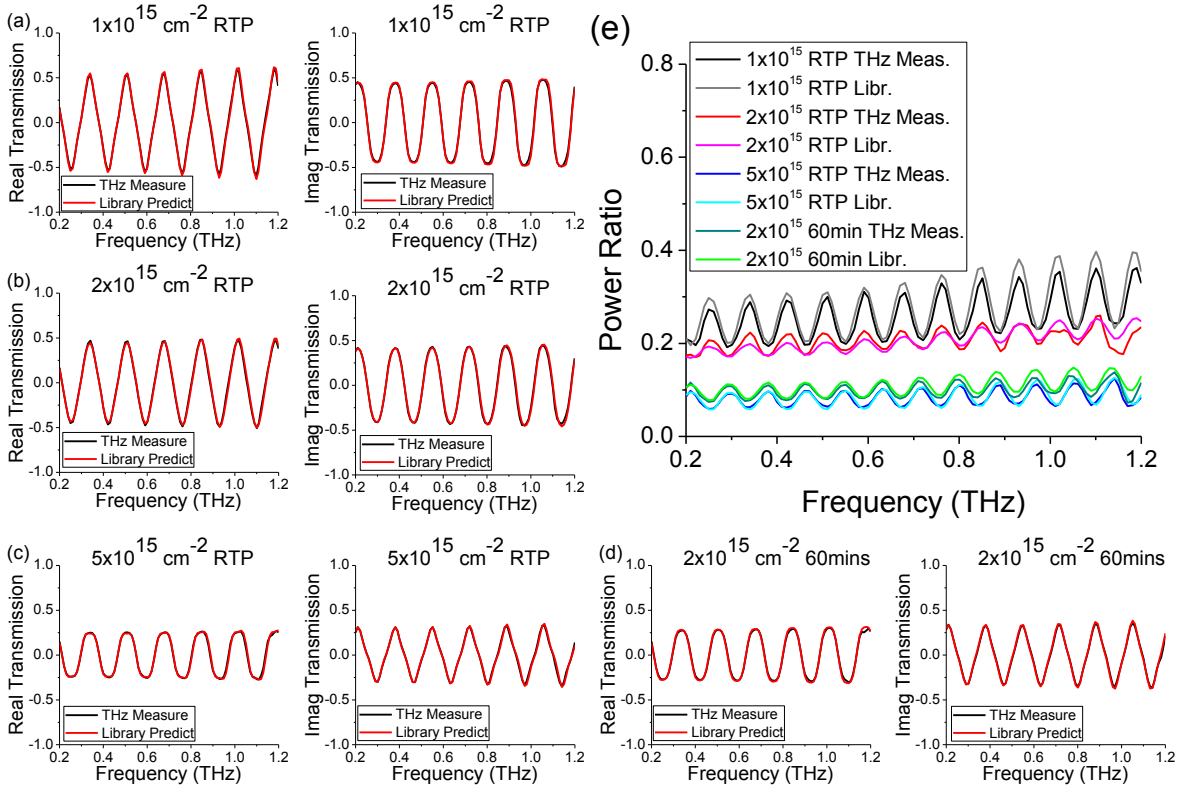

Figure 7.3 (a-d) THz complex transmissions from four distinct profiles chosen in Figure 6.2. Black curves are from THz measurements and red curves are from the library predictions (e) Power ratios from the same profiles by taking superposition of the square of the complex transmission.

7.3.2 Experimental Demonstration of Destructive Profile Measurement

For the destructive profile construction, the utilized frequency bandwidth is limited to around 1.2 THz in our photoconductive system and can potentially be extended to 8 THz using the plasma system. The THz measurement and data analysis were done on all thirteen samples to construct the profile but only selected six samples with 20, 60, 100, 160, 220 and 320 nm Si removal thicknesses to clearly deliver the main message. In the as-implant profile, the peak concentration and junction depth are about 4×10^{20} cm^{-3} and 0.45 μm, respectively. The 60keV implant energy drove phosphorus atoms into a deeper location and caused the bump shape in the heavily doped region during the annealing process. After 320 nm Si removal, the peak concentration is reduced to ~3×10^{17} cm^{-3}. The SIMS measurement performs a higher substrate concentration at 3×10^{15} cm^{-3} due to the detection limit and sheet resistance measurement gave us

~1.2×10^{15} cm^{-3} estimated substrate concentration. We finally decided 1.2×10^{15} cm^{-3} as the substrate concentration in the following data analysis process.

Figure 7.4 shows the THz radiation change in the time domain from six chosen samples, which demonstrate again the profile recognition ability reported in our previous work [178]. Along with the removal of heavily doped regions, the amplitude of THz radiation increases as a function of oxidation thickness. Compared to the silicon substrate, the as-implant profile (black curve) absorbs 75.35% THz radiation by calculating the amplitude change from the main absorption peak. The amplitude increasing in the main absorption peak compared to the as-implant profile are 7%, 52%, 96%, 322%, 365%, and 376% in all six samples, which were corresponding to the Si removal thickness of 20 nm, 60 nm, 100 nm, 160 nm, 220 nm, and 320 nm, respectively. The 1st internal reflection peak is observed to have a bigger shape distortion but smaller amplitude change, which results from the ×3 traveling patch inside the sample. The peak amplitude not only increases with the Si removal but also shifts its location to the right while removal thickness is > 160 nm. Data in the time domain helps us recognize the profile change to the as-implant one and abundant information in the frequency domain is required to map the entire profile.

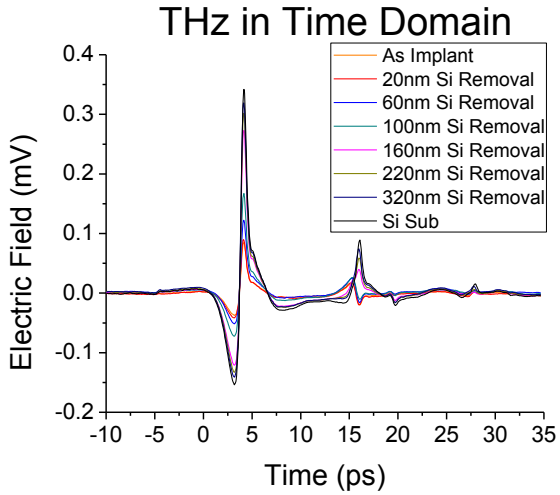

Figure 7.4 THz measurements in time domain from six chosen samples.

The previous work [178] indicates that each doping profile has an unique dispersion (different phase shift between different frequencies) and also unique patterns of internal reflection for different frequencies. These factors together result in a unique transmission spectrum in some ways similar to fingerprint. It is these considerations that make the power transmission ratio in the frequency domain a very sensitive indicator of doping profile change. This specialty motivates us to predict a doping profile using frequency domain information. Two strategies, reverse mapping and weighted average, are given as examples to demonstrate a destructive doping profile construction. The detail analysis procedure is illustrated in Figure 7.5. In this particular demonstration, air scan is defined as the reference for the calculation of complex transmission (also power ratio and phase shift). The detailed interpretation of above two strategies is discussed in the following sections.

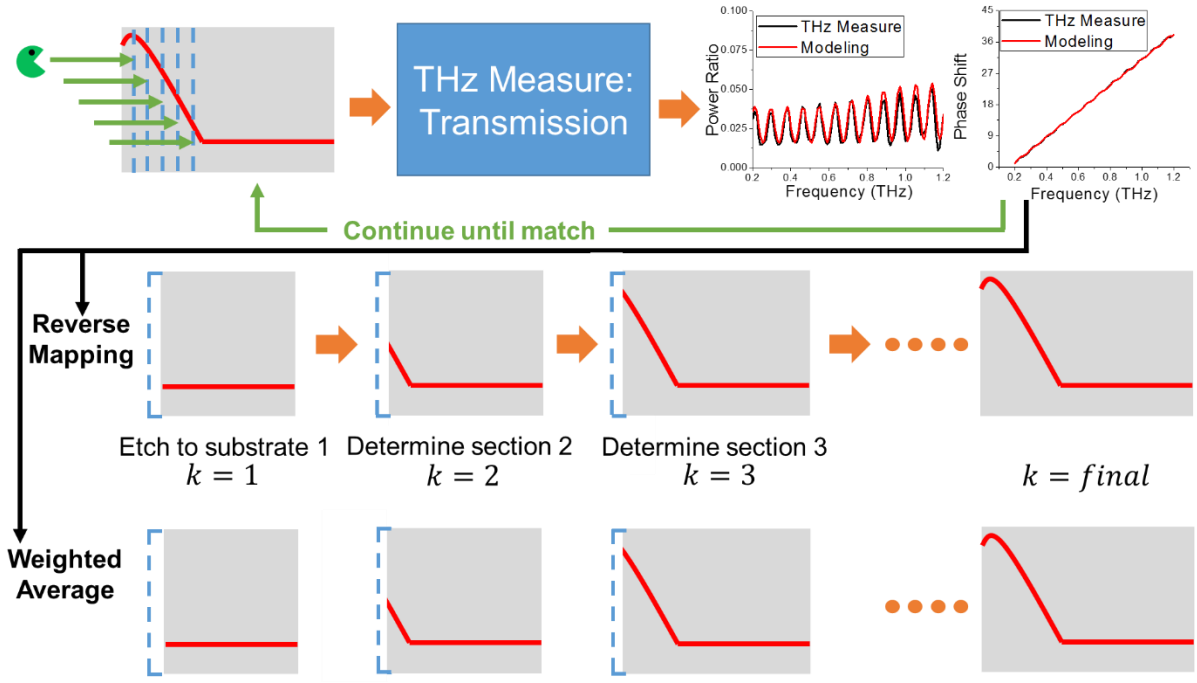

Figure 7.5 Diagram of destructive doping profile mapping, including the sequence of reverse mapping and weighted average.

While receiving samples with unknown doping profiles, the anodic oxidation technique can be applied either on the same sample location with fixed thickness removal or different wafer places with individual thicknesses targeted. A better thickness control and less THz measurement uncertainty are expected using the 1st option but in this conceptual demonstration the 2nd option was adopted to save the time for the sample preparation. The THz measurement usually consists of an air, Si substrate and sample scan. The air and sample scan are used for the doping profile construction in each cycle and the Si substrate scan is used as a reference to detect the junction depth. The profile junction is determined when there is no obvious difference found in THz measurements between the sample and the Si substrate. The residual doping profile is considered to be optically invisible and treated as the substrate area. Based on the empirical refractive index information, the residual profile induced THz absorption should be negligible. The etched silicon thickness is typically estimated from the measured SiO_2 thickness with a fixed ratio 0.46 multiplied and its accuracy is essential to the concentration determination of profile segments. The information of the bulk substrate concentration and thickness is vital to know prior to the profile concentration and relative study can be found in the previous work [179]. The profile construction process starts from the last etched sample and ends up with the as-implant sample. This is where the name "*Reverse Mapping*" comes from. In the backward prediction process, the profile segment predicted in the "(n+1) th" cycle sample is used as the basis to estimate the concentration of the next segment in the "n th" cycle sample. Concentrations of all profile segments are determined by approaching a minimum complex transmission difference (also power ratio and phase shift) between the THz measurement and the prediction from the transfer matrix.

In below conceptual demonstration, the substrate concentration is ~1.26×10^{15} cm^{-3} from CDRES MAP, the substrate thickness is 523 μm and the modeling region is 0.5 μm, covering the profile junction depth from SIMS. 25 segments with 20 nm width in each slice are used in the modeling process. Figure 7.6 shows that power ratio differences in all six samples are close enough and smaller than the measurement uncertainty [178] by adjusting additional profile segments. By repeating the same procedure, the destructive doping profile is constructed eventually.

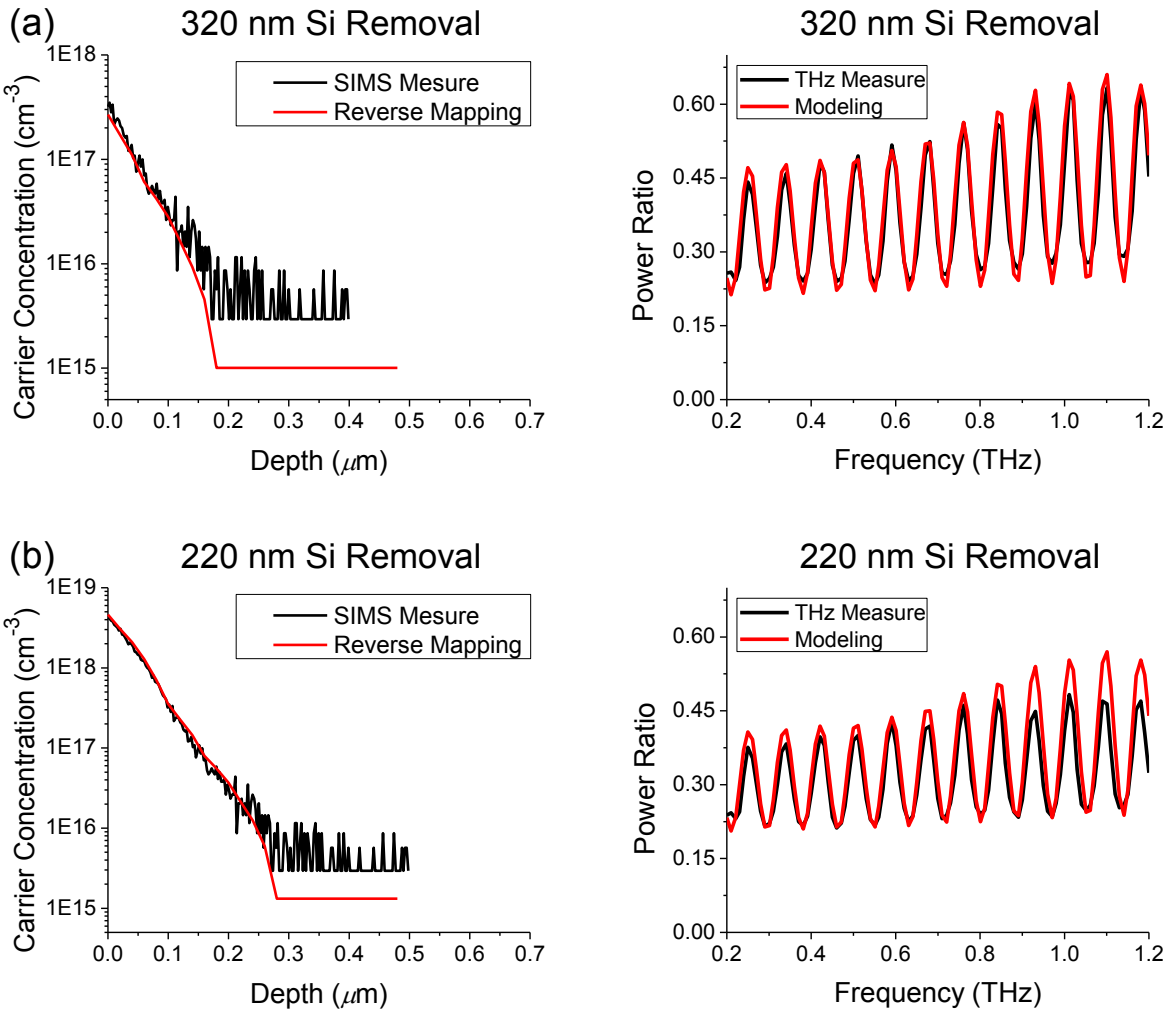

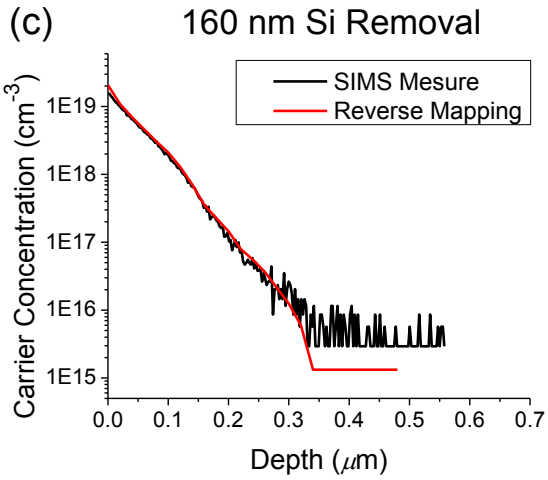
(c)
160 nm Si Removal
SIMS Mesure
Reverse Mapping
Carrier Concentration (cm-3)
1E19
1E18
1E17
1E16
1E15
0.0 0.1 0.2 0.3 0.4 0.5 0.6 0.7
Depth (μm)

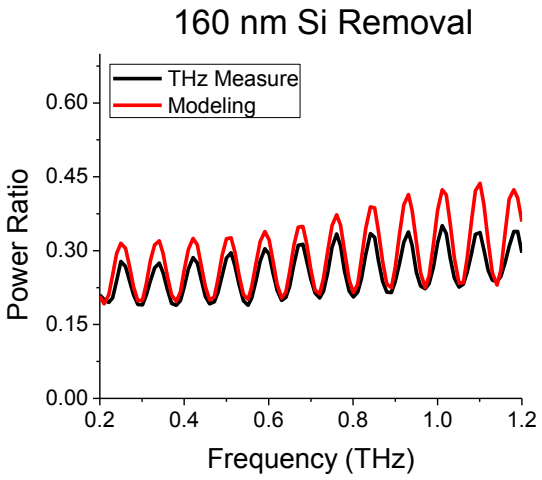
160 nm Si Removal
THz Measure
Modeling
Power Ratio
0.60
0.45
0.30
0.15
0.00
0.2 0.4 0.6 0.8 1.0 1.2
Frequency (THz)

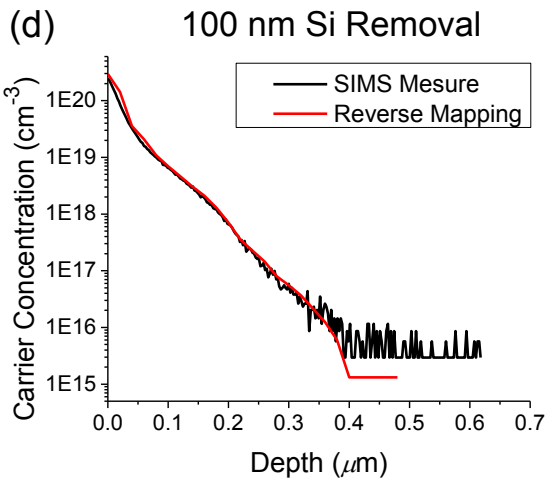
(d)
100 nm Si Removal
SIMS Mesure
Reverse Mapping
Carrier Concentration (cm-3)
1E20
1E19
1E18
1E17
1E16
1E15
0.0 0.1 0.2 0.3 0.4 0.5 0.6 0.7
Depth (μm)

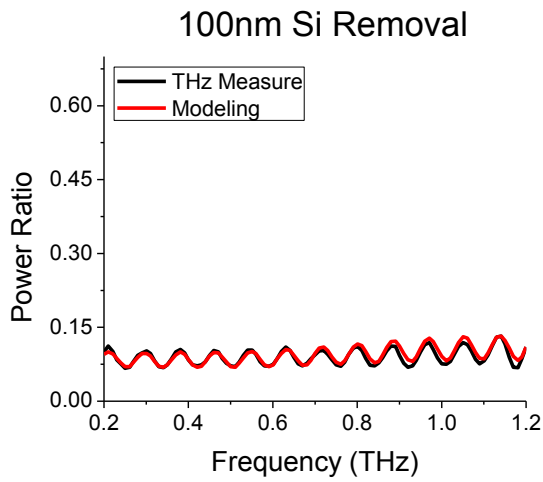
100nm Si Removal
THz Measure
Modeling
Power Ratio
0.60
0.45
0.30
0.15
0.00
0.2 0.4 0.6 0.8 1.0 1.2
Frequency (THz)

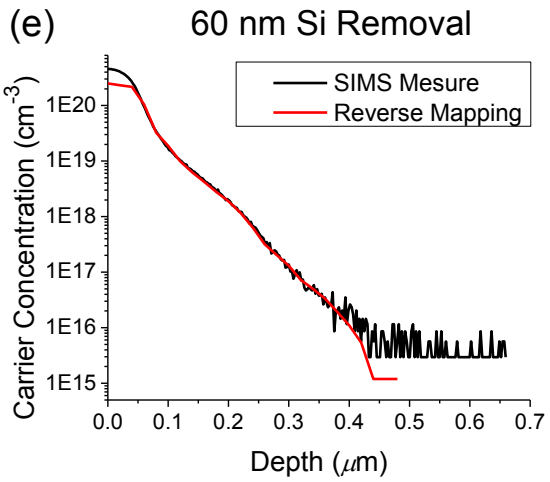
(e)
60 nm Si Removal
SIMS Mesure
Reverse Mapping
Carrier Concentration (cm-3)
1E20
1E19
1E18
1E17
1E16
1E15
0.0 0.1 0.2 0.3 0.4 0.5 0.6 0.7
Depth (μm)

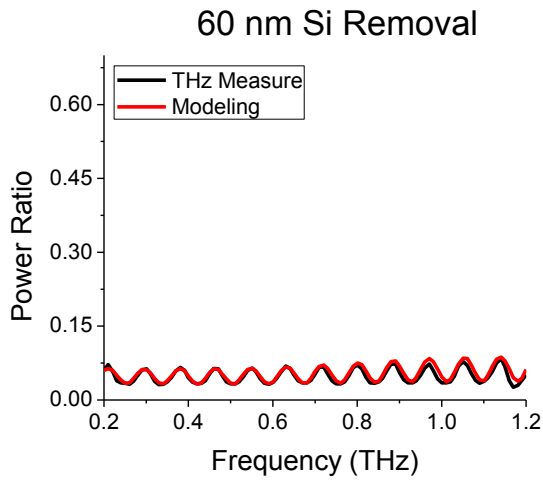
60 nm Si Removal
THz Measure
Modeling
Power Ratio
0.60
0.45
0.30
0.15
0.00
0.2 0.4 0.6 0.8 1.0 1.2
Frequency (THz)

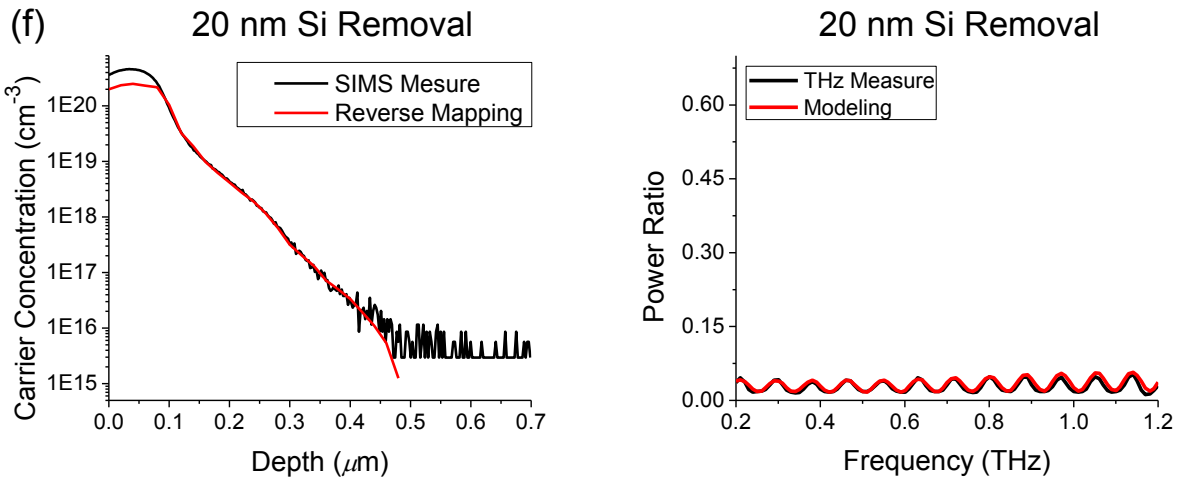

Figure 7.6 The step-by-step demonstration of the reverse mapping method using six chosen samples. Differences between power transmission ratios and THz measurements are smaller than the measurement uncertainty.

Reverse doping profile mapping is a straight forward method to construct a doping profile but the result might be greatly impacted by accuracies from initial cycles. Since the detection resolution in a THz-TDS is relatively poorer in the lightly doped region than the heavily doped one, the weighted average idea is an alternative option to potentially smooth such effect with only slightly change in the profile fitting process.

In the weighted average process, it doesn't matter we process the profile fitting process in a forward or revere sequence. Each case experiences its own profile fitting process and the final profile is achieved through a data average by the use of a weighted table. Since the most etched sample should experience the maximum number of THz measurements (if the 1st option is adopted), a heavier weighting value is assigned during the average process (see appendices). In the below demonstration, the generalized triangular number series is applied to generate weighted values $w_{i,j}$ (see equation 7.1) in the weighted table. This series is tried as an example and other mathematical series are alternative options. Depend on the THz scan number and the segment number in a profile, weighted values can be varied.

$$w_{i,j} = \frac{x_{i,j}}{\sum_j x_{i,j}} \tag{7.1}$$

The weighted average method requires an initial guess profile to start the process. This guess profile can either come from process simulators or previously known profiles under the same process conditions from other characterization techniques. Different from the reverse mapping method, all profile segments are allowed to vary in the weighted average process. People can either fit all sample profiles in parallel using the same initial guess profile or fit next sample profile by utilizing the initial guess profile from the previous fitting result. We took the SIMS measured profile as the initial guess profile to approach THz measurements from all cycles. Over here the modeling region, substrate thickness and concentration are the same to the previous reverse mapping demonstration. In Figure 7.7, initial guess profiles in six demo samples are moved up and down to achieve minimum power ratio differences by multiplying various ratios. The substrate is kept constant in all samples during the modeling process. These fitted profiles are then multiplied by weighted values and averaged to construct the final profile prediction.

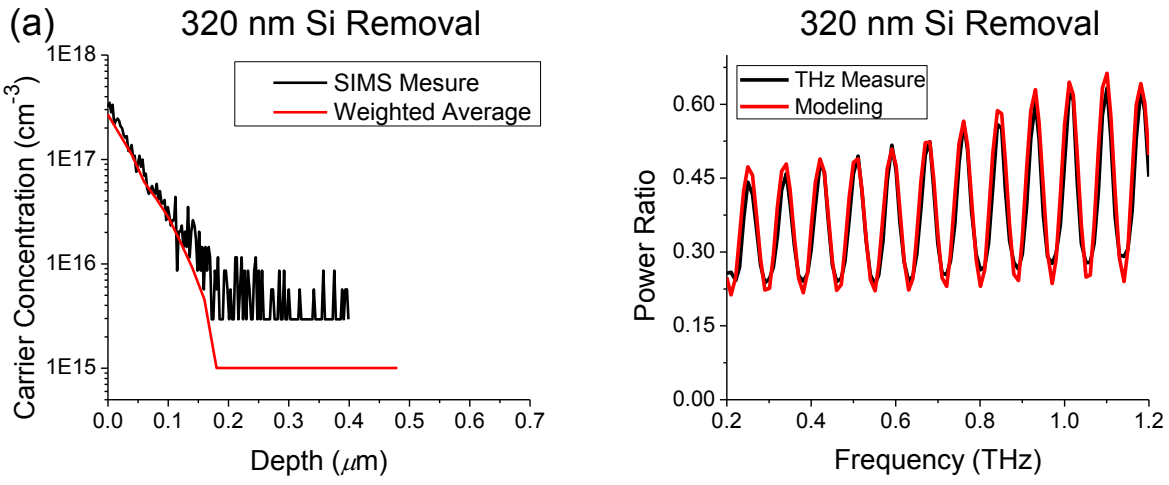

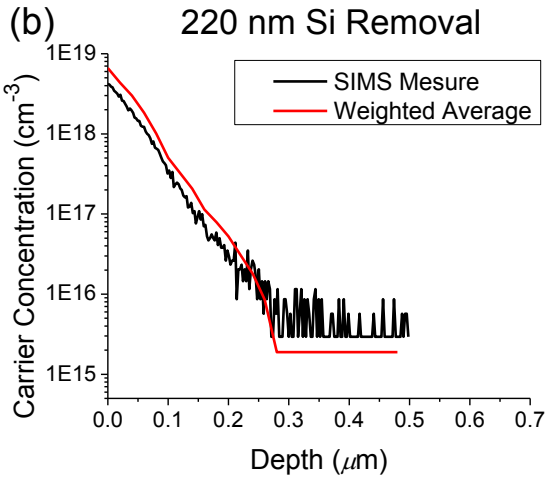
(b)
220 nm Si Removal
SIMS Mesure
Weighted Average
Carrier Concentration (cm-3)
1E19
1E18
1E17
1E16
1E15
0.0 0.1 0.2 0.3 0.4 0.5 0.6 0.7
Depth (μm)

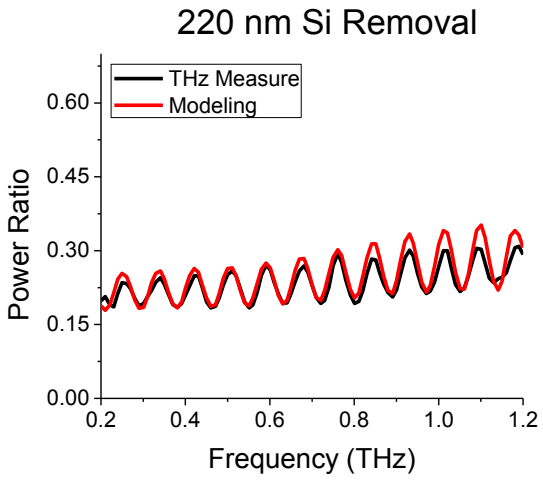
220 nm Si Removal
THz Measure
Modeling
Power Ratio
0.60
0.45
0.30
0.15
0.00
0.2 0.4 0.6 0.8 1.0 1.2
Frequency (THz)

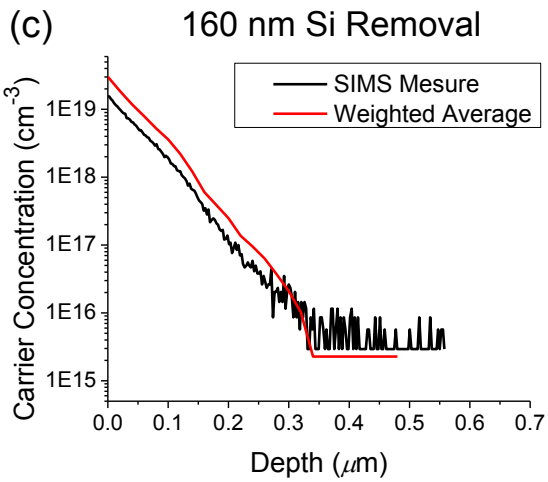
(c)
160 nm Si Removal
SIMS Mesure
Weighted Average
Carrier Concentration (cm-3)
1E19
1E18
1E17
1E16
1E15
0.0 0.1 0.2 0.3 0.4 0.5 0.6 0.7
Depth (μm)

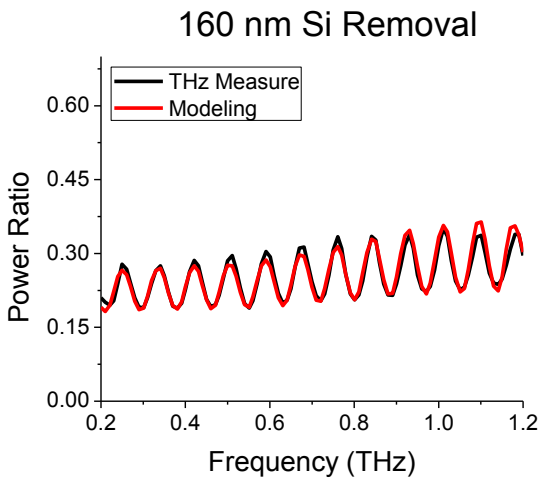
160 nm Si Removal
THz Measure
Modeling
Power Ratio
0.60
0.45
0.30
0.15
0.00
0.2 0.4 0.6 0.8 1.0 1.2
Frequency (THz)

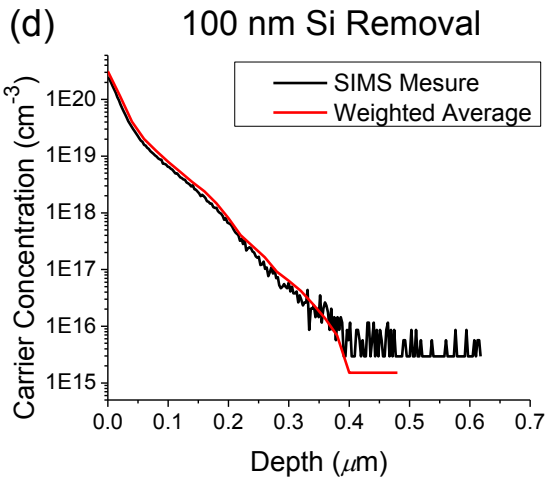
(d)
100 nm Si Removal
SIMS Mesure
Weighted Average
Carrier Concentration (cm-3)
1E20
1E19
1E18
1E17
1E16
1E15
0.0 0.1 0.2 0.3 0.4 0.5 0.6 0.7
Depth (μm)

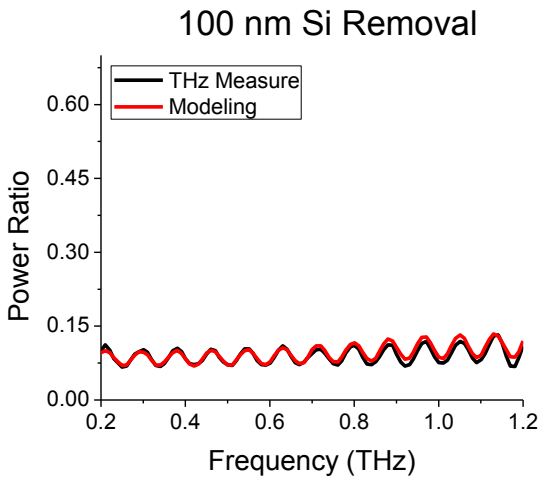
100 nm Si Removal
THz Measure
Modeling
Power Ratio
0.60
0.45
0.30
0.15
0.00
0.2 0.4 0.6 0.8 1.0 1.2
Frequency (THz)

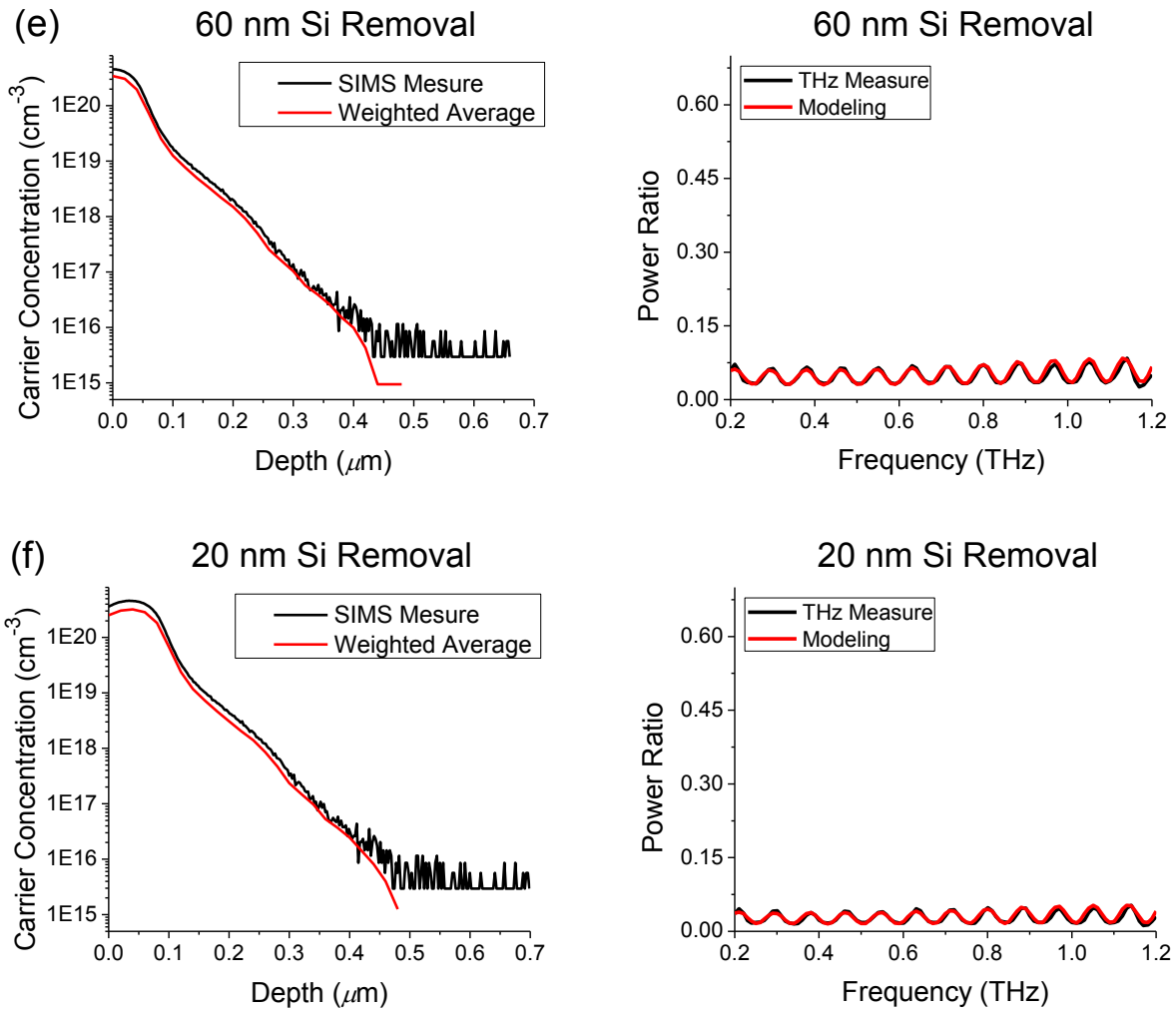

Figure 7.7 The step-by-step demonstration of the weighted average method using six chosen samples. Power transmission ratio differences to THz measurements are smaller than the measurement uncertainty.

For simple doping profiles, following Gaussian or complementary error function (erfc) distributions, peak concentrations can be readily calculated from sheet resistances (Rs) by the well-known Irvin's curves [180]. In Figure 7.1 (a), we observed that Rs increases with the Si removal. What would be the result if the sheet resistance measurement is combined with the cycling Si removal process to reversely predict a doping profile? In the practice, the n-type Gaussian Irvine's curve with substrate concentration of 10^{15} cm^{-3} is selected to determine peak concentrations from all cycle samples through their Rs measurements. Multiplying Rs with

corresponding junction depth gives us the RsXj value to estimate the surface concentration. Finally, plotting these surface concentrations to junction depth yields the approximated doping profile, shown in Figure 7.8.

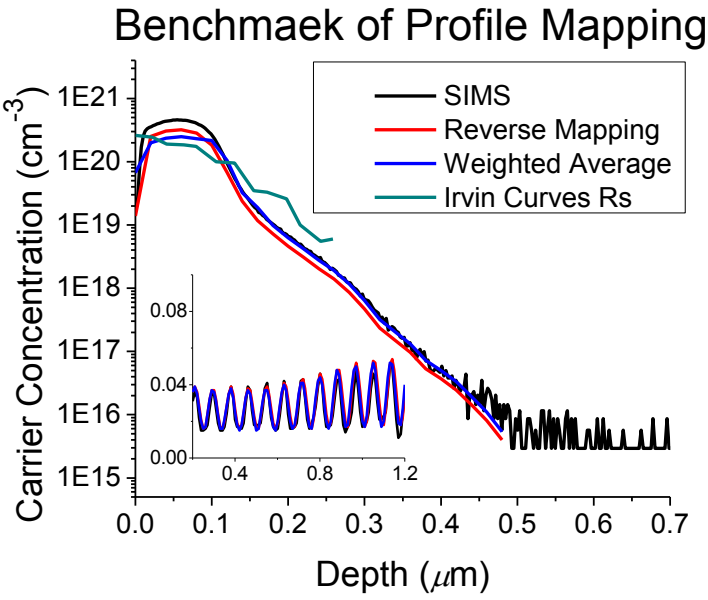

Figure 7.8 Benchmark of destructive doping profile construction: Reverse Mapping vs Weighting Average vs Irvin Curves Rs.

Constructed doping profiles from reverse mapping, weighted average and Irvin Curves methods are benchmarked with the SIMS measured profile in Figure 7.8. It is clear to see that profiles from reverse mapping and weighted average methods are in an acceptable agreement. Compared to the SIMS profile, their profile concentrations are lighter in heavily doped regions but much closer in moderate and lightly doped regions. This phenomenon is pretty reasonable by considering the difference between a chemical doping profile and an electrical doping profile. Many literatures indicate that inactive dopants are typically created in a diffusion process or an ion implanted process with inserted dosage higher than the solubility limit and the induced profile difference was studied using ECV and SIMS [2, 181]. The profile difference in Figure 7.8 pinpoints the same mechanism since THz-TDS is doing an electrical doping profile prediction. In

the small inset of Figure 7.8, the black curve represents the sample THz measurement, not the model prediction from the SIMS profile. Therefore, these profile predictions are proven to be reasonable from the THz spectrum point of view, which represents the electrical performance in THz regions.

As we expect, the profile prediction from Irvine's curves doesn't give us a good profile agreement. The technique is typically applicable if junctions are reasonably deep and not easy to deal with profiles with shallow junctions. Furthermore, if the concentration profile is non-ideal (i.e., it is not of either Gaussian or complementary error function form), incorrect or inconclusive results will be obtained. In the current industry applications, which work on shallow junction profiles most of the time, the profile prediction using Irvine's curves might not be in the top of the selecting list.

7.3.3 Experimental Demonstration of Non-Contact Profile Prediction

In this section, we continue the conceptual demonstration in a non-contact manner and the process flow of the prediction procedure is shown in Figure 7.9. Once the power ratio and phase shift from complex transmission are obtained from a THz measurement, the reverse fitting process comes into the play to predict a doping profile. In Chapter 6, we already know that different profile shapes might give similar frequency behaviors (profile degeneracy) to mess up the profile prediction. Therefore, an initial guess profile is a key component in the reverse fitting process to tell where to start. During the reverse fitting process, the initial guess profile is input into the transfer matrix to generate the 1^{st} run complex transmission and then calculates the complex transmission difference through the subtraction to the THz measurement. The complex transmission difference is then brought to zero through the repeated profile changing process. Process simulator, mathematical model and known SIMS profile from past process condition are

proposed choices to get the initial guess profile. A rough idea of the profile shape is then given for the later fitting process. During the reverse fitting process, either doping profile or mathematical parameter can be selected to approach. Different ways to generate the initial guess and targets in the reverse fitting create six combinations to predict a doping profile. Two examples, process simulation and SIMS profile combined with directly profile fit, are demonstrated in later sections.

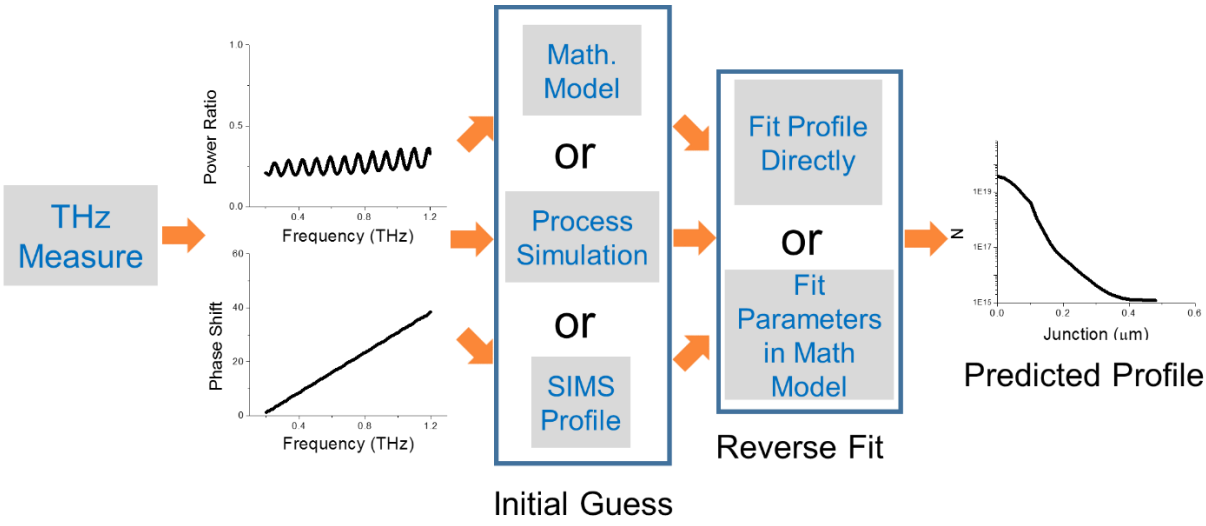

Figure 7.9 Diagram flow of a non-contact doping profile prediction.

Four distinct profiles from Chapter 6 (1×10^{15} cm^{-3} RTP, 2×10^{15} cm^{-3} RTP, 5×10^{15} cm^{-3} RTP, 2×10^{15} cm^{-3} 60mins) are utilized and the demonstration starts from the generation of an initial guess profile using mathematical models. Algebras are used in mathematical models to determine the profile feature and interpret physical mechanisms. One example is the LFD+RFD model [163], proposed by Frank Wirbeleit *et. al*, to depict liquid diffusion profiles with kink-and-tail features. Four major parameters a_1, x_1, a_2 and x_2 represent peak concentration, kink position, kink concentration and junction depth, respectively. In Figure 7.10 (a), the same model is practiced on our mc-Si wafer with a commercial PV diffusion profile and achieves a good

fitting result. However this model is also proven to not adequately deal with ion implanted doping profiles in c-Si wafers (Figure 7.10 (b-d), red curves). The observed discrepancies can be interpreted by two major reasons. First, the enhanced diffusion induced kink-and-tail feature in single and multi-crystalline silicon (PV) could be different, where the feature can be promoted by grain boundaries and crystal dislocations. Second, the enhanced diffusion in ion implanted profiles comes from not only the thermal budget utilized in the liquid diffusion profiles, but also the ion implanted damage cluster. This practice indicates that different models are required to cope with different physical mechanisms induced profile features.

Different from the liquid diffusion process, enhanced diffusion in the ion implantation process mainly comes from an athermal generation of interstitials and vacancies through the collisional displacements of lattice atoms. Between the dosage levels 5×10^{12} cm^{-2} to 10^{14} cm^{-2}, interstitial clusters from the implantation damage form unstable (311) defects, containing excess Si interstitials. Above this threshold level, some (311) defects are reformed to stable Frank loops and perfect dislocations [182]. Upon annealing, clusters emit point defects (excess Si interstitials and vacancies) and couple with dopants to diffuse into the bulk. These point defects, called Frenkel pairs, can result in diffusivities several thousand times great greater than the normal diffusibility, depending on the annealing temperature. Stable Frank loops and perfect dislocations will change the interstitial injection. The “+1 model” indicates that the imbalance in interstitial and vacancy concentration from implanted dopants is approximately equal to the excess Si interstitial number. Shishiyanu rephrased the mechanism of enhanced diffusion form the energy point of view [183]. Clusters (deformed molecules) decrease the defect energy formation in the crystal lattice of semiconductors to achieve the enhanced diffusion.

Instead of having mathematical parameters to bridge equations to profile features, process simulator utilizes intuitive process parameters to provide the initial guess profile. Different models from past researches are built inside process simulators like TCAD to predict profile features under various process conditions. In Figure 7.10 (b-d), the example "Stanford Full Coupled Model" [182, 184] is tried and proven to give close profile features to the ion implanted profiles (blue curves) with close input process parameters, shown in Table 7.1, to the real process conditions. The major advantage of the process simulation is the convenience for the real-time process monitor from intuitive process parameters.

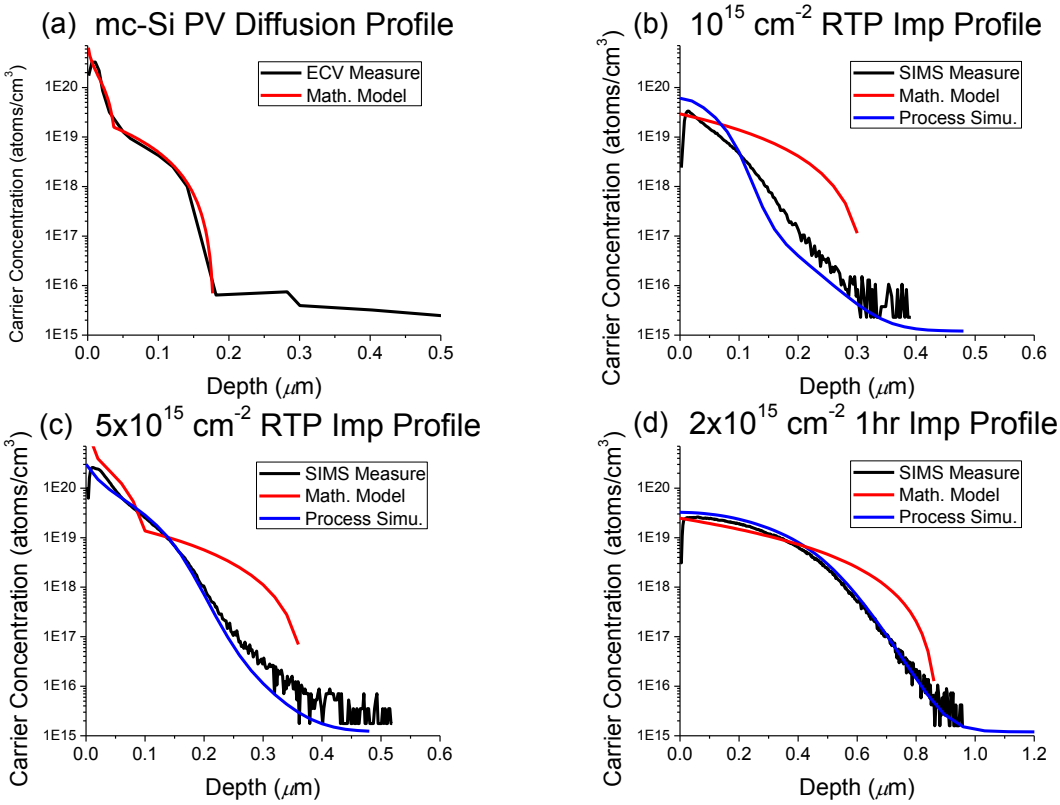

Figure 7.10 Profile fitting results from the mathematical LFD+RFD model (red curves) and the SILVACO built-in process model (blue curves) and the benchmark to the mc-Si diffusion profile and c-Si ion implanted profiles.

Sample Number		1	2	3	4
Parameters in Real Process	Oxide Thickness (nm)	~60			
	Implant Energy (keV)	30			
	Implant Dose (cm^{-2})	10^{15}	$2x10^{15}$	$5x10^{15}$	$2x10^{15}$
	Drive-in Time (min)	2			60
	Drive-in Temp (C)	1000			
Parameters in Simulator	Oxide Thickness (nm)	60	60	65	55
	Implant Energy (keV)	30	30	30	30
	Implant Dose (cm^{-2})	10^{15}	$2x10^{15}$	$5x10^{15}$	$2x10^{15}$
	Drive-in Time (min)	2.5	2	1.5	65
	Drive-in Temp (C)	1000	975	1000	1025

4) Table 7.1 Process parameters used in the process simulator and practical operation.

Except model predicted profiles, initial guess profiles under various process conditions can also be generated through existing metrologies such as ECV and SIMS. Using these measured profiles has two advantages. First, empirical features from measured profiles give better starting points to predict accurate doping profiles, even though the reverse fitting algorithm is not complicated. Second, different process tools usually perform slightly different process features as their own footprints under the same process condition. There is no way for model predicted profiles to contain such detail knowledge but measured profiles. Therefore, measured profiles are expected to achieve better profile predictions. However, the major advantage of this method is the requirement of the costly database. In the below demonstration, SIMS measured initial guess profiles are utilized as examples to benchmark the prediction performance from the process simulator. The effect between the chemical and electrical profile are also taken into the consideration.

As we described before, the reverse fitting process keeps changing the guess profile until detecting a minimum difference to the measured power ratio and phase shift. Under this logic, various advanced algorithms can be developed and one strategy is proposed here as an example.

No matter what initial guess profile we choose, either a smaller or bigger complex transmission to the one from the unknown profile can be achieved. In Figure 7.11, these two cases are listed in step 1 as the starting point of the fitting process. Initial guess profiles in each case can be either with or without intersections to the unknown profile. In step 2, these initial guess profiles are multiplied by constant ratios to shift up and down and roughly approach minimum transmission differences to THz-TDS measured complex transmissions. The goal over here is to make profile intersections without shape changes. Since refractive indices in heavily doped regions are much higher than moderately and lightly doped regions, shifted guess profiles with higher heavily doped regions than unknown profiles always own smaller complex transmissions. Then the proposed algorithm comes into play to drive the transmission difference as small as possible, shown in step 3. This fine tuning algorithm basically does the profile rotation to pursue a minimum complex transmission. Profile segments are divided into two groups and two segments from each group are selected in pairs to optimize with proper step sizes. When the segment from group one in moved either up or down or no change, the corresponding segment in group two is moved simultaneously to determine the combination with a smaller transmission difference. The profile rotation is then achieved by repeating above process from individual segment pairs. Unless the predicted profile has regions > $10^{20}cm^{-3}$, the final profile prediction is determined in step 3. The additional step 4 is used only to refine the profile with inactive dopants in heavily doped regions, which are typically seen in electrical profiles from the diffusion process and ion implantation process with highly inserted dosages. It is because that initial guess profiles we proposed above are all chemical profiles. In step 4, regions above the dopant solubility are assumed to be flat to form a new initial guess profile and

then the same fine tuning algorithm is repeated again to achieve a new profile prediction with a minimum transmission difference.

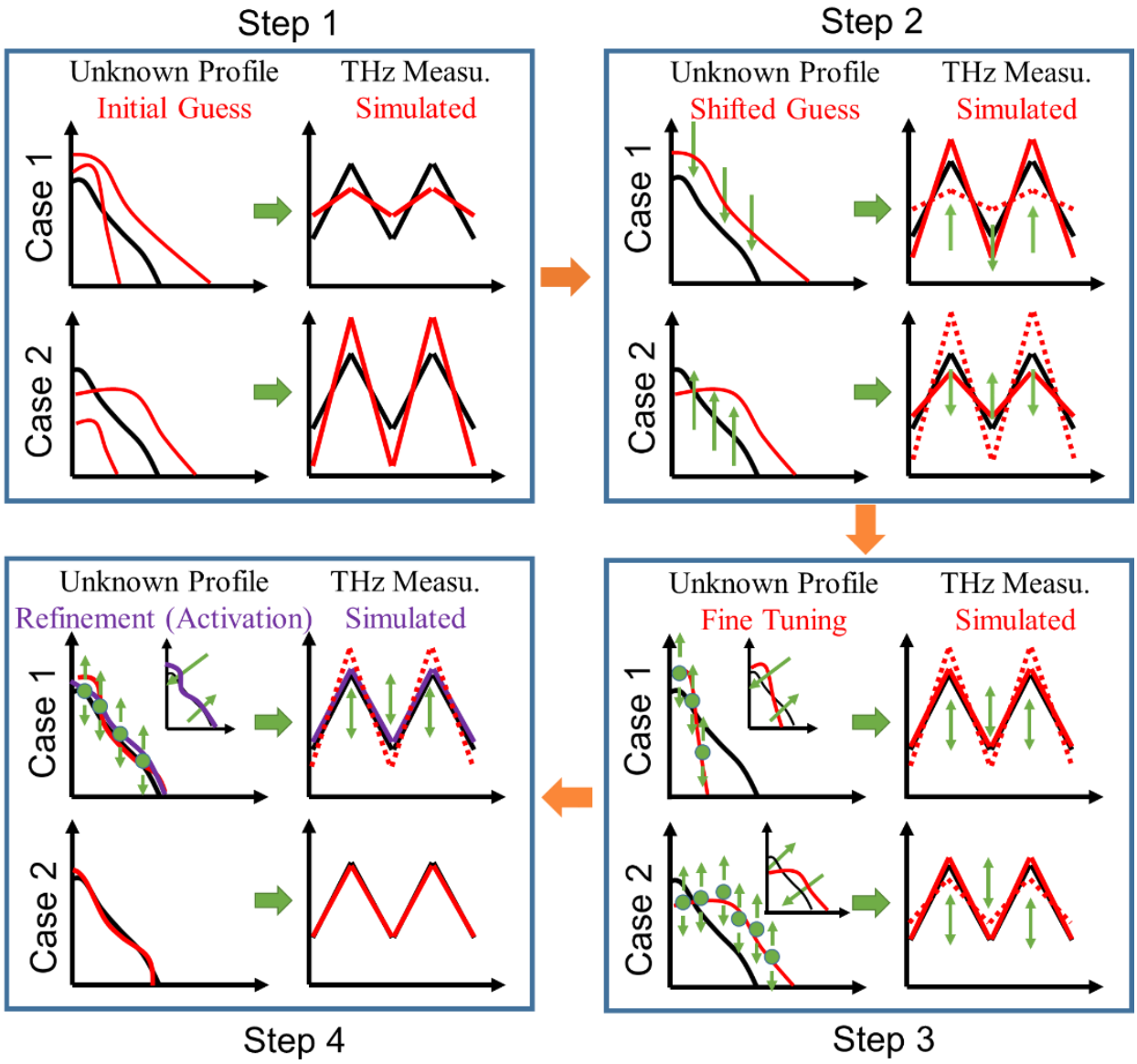

Figure 7.11 The proposed strategy to reversely predict a doping profile (red curve). The black curve is the targeted profile. In step 1, initial guess profiles are generated from above three methods. In step 2, a profile intersection is achieved by shooting a roughly minimum transmission difference. In step 3, the final prediction is achieved by approaching a smallest transmission difference. The step 4 is utilized with the consideration of inactive dopants.

Since we don't have a mathematical model to properly describe ion implanted profiles yet, initial guess profiles in the demonstration are based on the process simulation and known

SIMS profiles. The strategy in Figure 7.11 is implemented to approach profiles in Figure 7.10 with various initial guess profiles. In Figure 7.12, profile predictions (green curves) indicate that using TCAD simulated initial profiles can potentially achieve close predictions to the SIMS ones. With proper selections of process parameters and models, initial guess profiles can be somewhere close to the target (unknown) profile. In Figure 7.12 (a)(c), initial guess profiles in 1×10^{15} and 5×10^{15} RTP samples already have intersections to their SMIS profiles (assume to be unknown) before doing step 2. Even under this situation, there is no change in the fitting strategy and these guess profiles just provide better starting points. In Figure 7.12, black, red and green curves represent SIMS measured profiles, initial guess profiles and final fitting results, respectively. Their complex transmission changes are performed next to the profile figures. It is observed that power ratios from final predictions (green curves) are close to THz measurements (black curves) and less than the measurement uncertainties are achieved after the fitting process. The predicted profiles also change shapes to be closer to their SIMS ones. The Gaussian shape profile (2×10^{15} 1hr), which contains less features, is observed to be fitted easier. Profile mismatches in the moderate and lightly doped regions of 1×10^{15} and 5×10^{15} RTP samples are larger than those in heavily doped regions and can be improved in advanced by optimizing the fitting strategy. Based on the demonstration from three distinct profiles, the proposed strategy is proven to be conceptually feasible using initial profiles from the process simulation. In the 1×10^{15} RTP example, transmission ratios decrease to 0.841277, 0.416683 and 0.411793 in step 1, 2 and 3, respectively. In the fitting process, only profile segments > 10^{16} cm^{-3} are chosen to participate the modeling and two groups are defined at ~1/3 profile location. Three constraints, monotonic decrease, > 10^{16} cm^{-3} segment concentration and stopping point at 0.41 transmission difference, are defined to eliminate unwanted solutions. In 2×10^{15} and 5×10^{15} examples, stopping

points are lower (~0.22) due to their smaller transmission differences. The correlation between complex transmissions and stopping points requires more practical profiles to study. Among three studied cases, only the example of 5×10^{15} RTP involves the step 4 by taking inactive dopants into the consideration and the flat region above 10^{20} cm^{-3} is observed in the final prediction. Not only differences between chemical and electrical doping profiles, but also the effect of electrons in impurity bands could induce profile differences to SIMS ones. Therefore, predicted profiles from a THz-TDS should be treated as "THz" doping profiles, which will be very close but not be 100% the same to profiles from existing techniques.

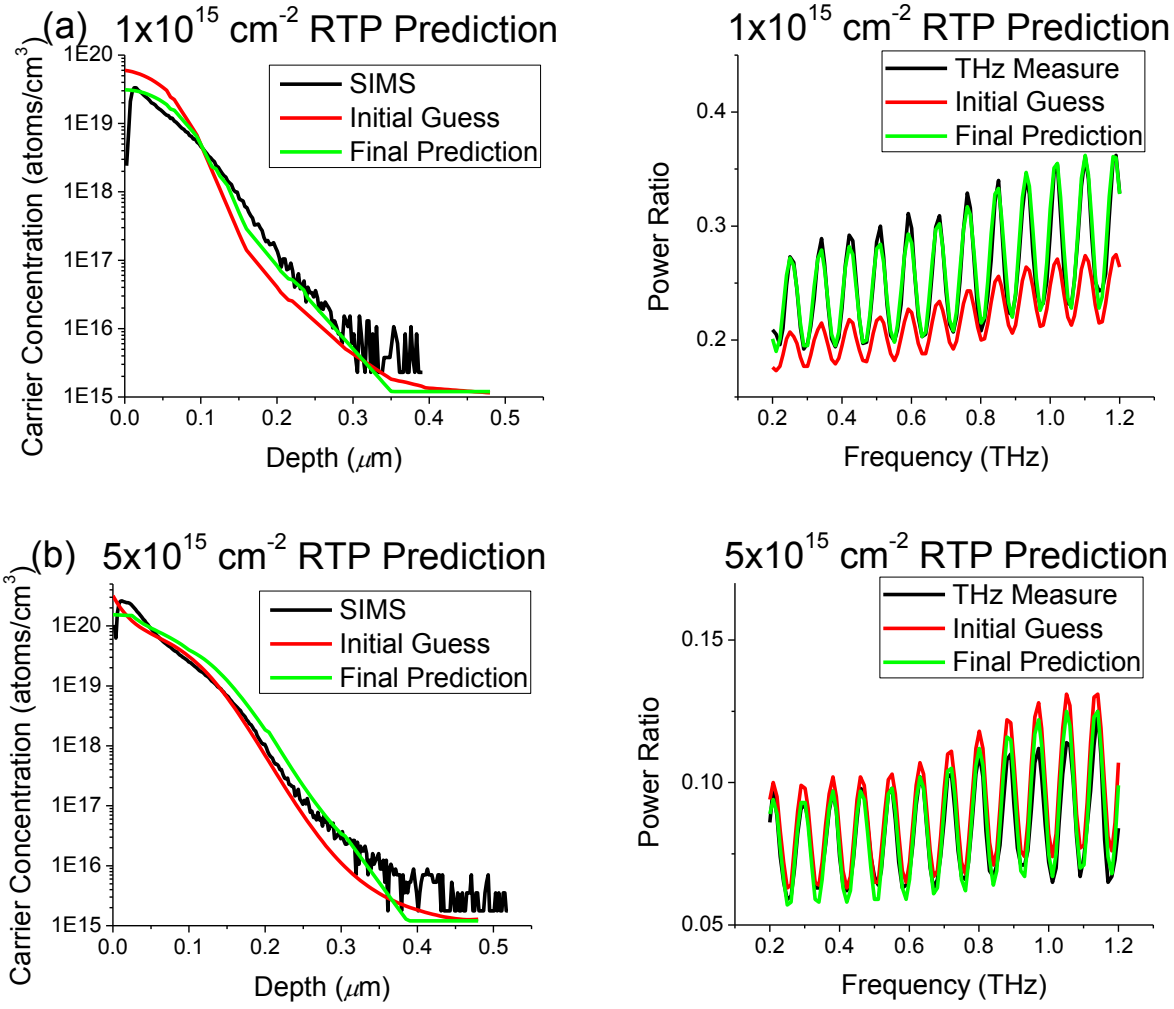

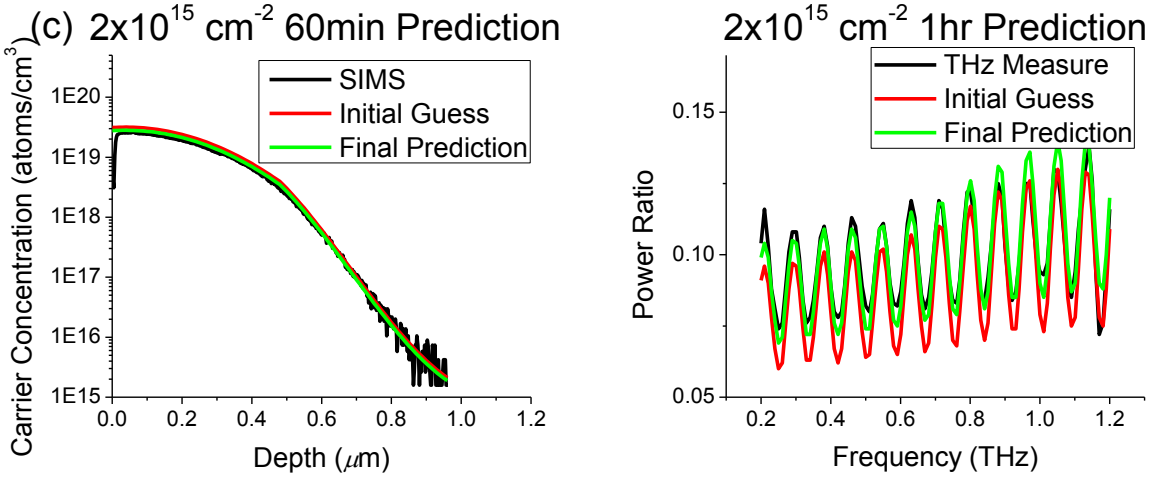

Figure 7.12 Demonstration of doping profile prediction using the strategy in Figure 7.11 and initial guess profiles from TCAD. The inactive dopant effect is only considered in the 5×10^{15} RTP example.

The same strategy described in above section is continuously applied using known SIMS profiles as initial guess profiles and results are shown in Figure 7.13 using 1×10^{15} and 5×10^{15} RTP samples. The common initial guess profile is given from the previous known SIMS measurement of the 2×10^{15} RTP sample. A similar observation to Figure 7.12 can be concluded over here. However, final predictions here are even closer to SIMS measurements under the same level power ratio differences, compared to ones in Figure 7.12. Subtle profile features are proven to be better predicted by utilizing known SIMS profiles as initial guess profiles.

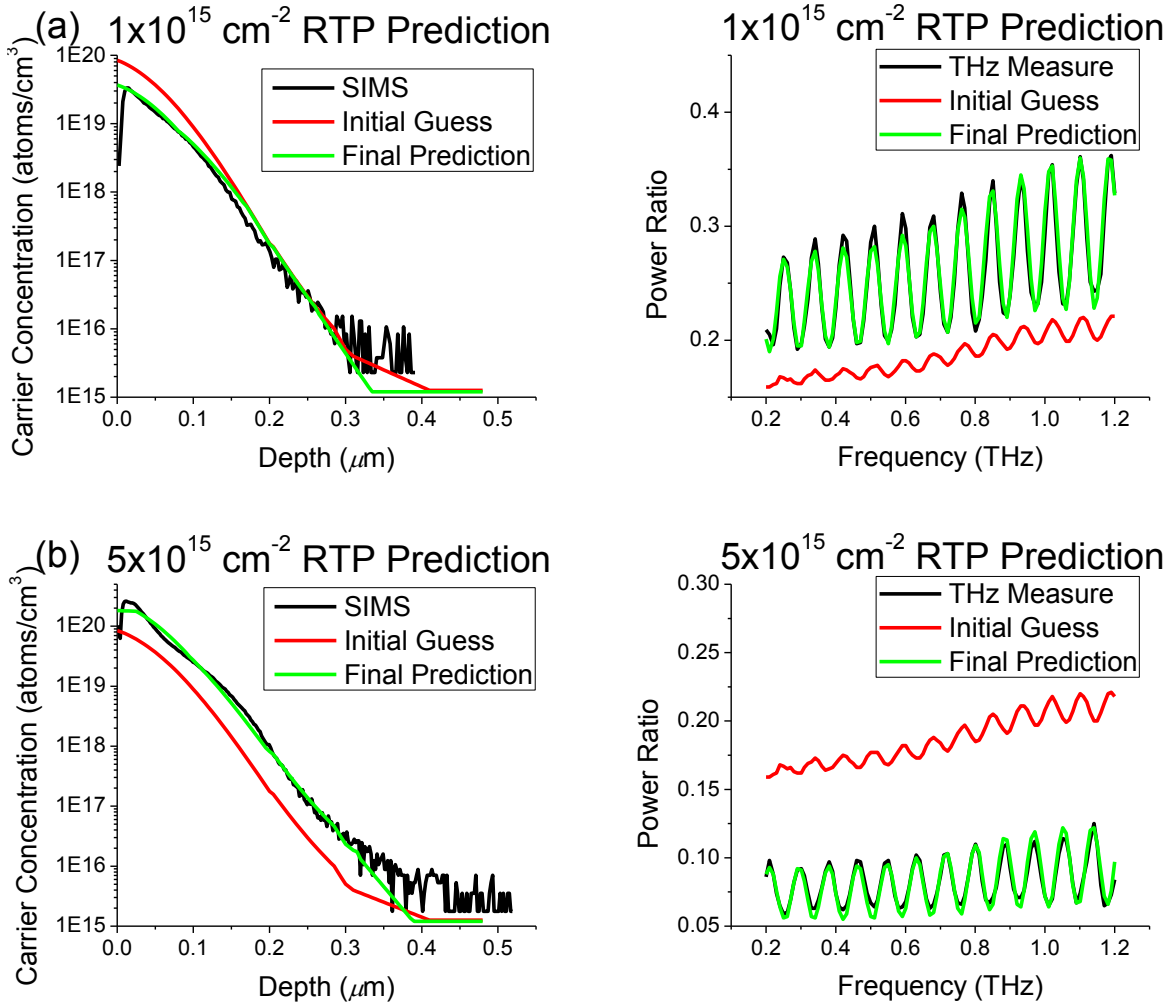

Figure 7.13 Demonstration of doping profile prediction using the strategy in Figure 7.11 and the initial guess profile from the SIMS profile of 2×10^{15} RTP sample. The inactive dopant effect is only considered in the 5×10^{15} RTP example.

As we described in the step 1 of Figure 7.11, initial guess profiles are generally divided into two cases. In the Figure 7.12 and 7.13, we have demonstrated two typical profiles in case 1 on the 1×10^{15} sample. Over here we continue the demonstration using typical profiles from case 2 on the same 1×10^{15} RTP sample to benchmark the prediction performance of the proposed strategy. Typical initial profiles from two cases are displayed in Figure 7.14 (a) and their final predictions are summarized in Figure 7.14 (b). In Figure 7.14 (a), initial guess 1 and 2 are the same as ones in Figure 7.12 (a) and Figure 7.13 (a). It is observed that final predictions from

various initial guess profiles could be close to each other with the same level transmission differences (0.411793, 0.413176, 0.414471 and 0.410429) under the same fitting process. On the other hand, four final predictions are slightly different but have a better overlapping in heavily doped regions to reflect a better resolution. In conclusion, the proposed strategy did a good job to process a non-contact doping profile prediction.

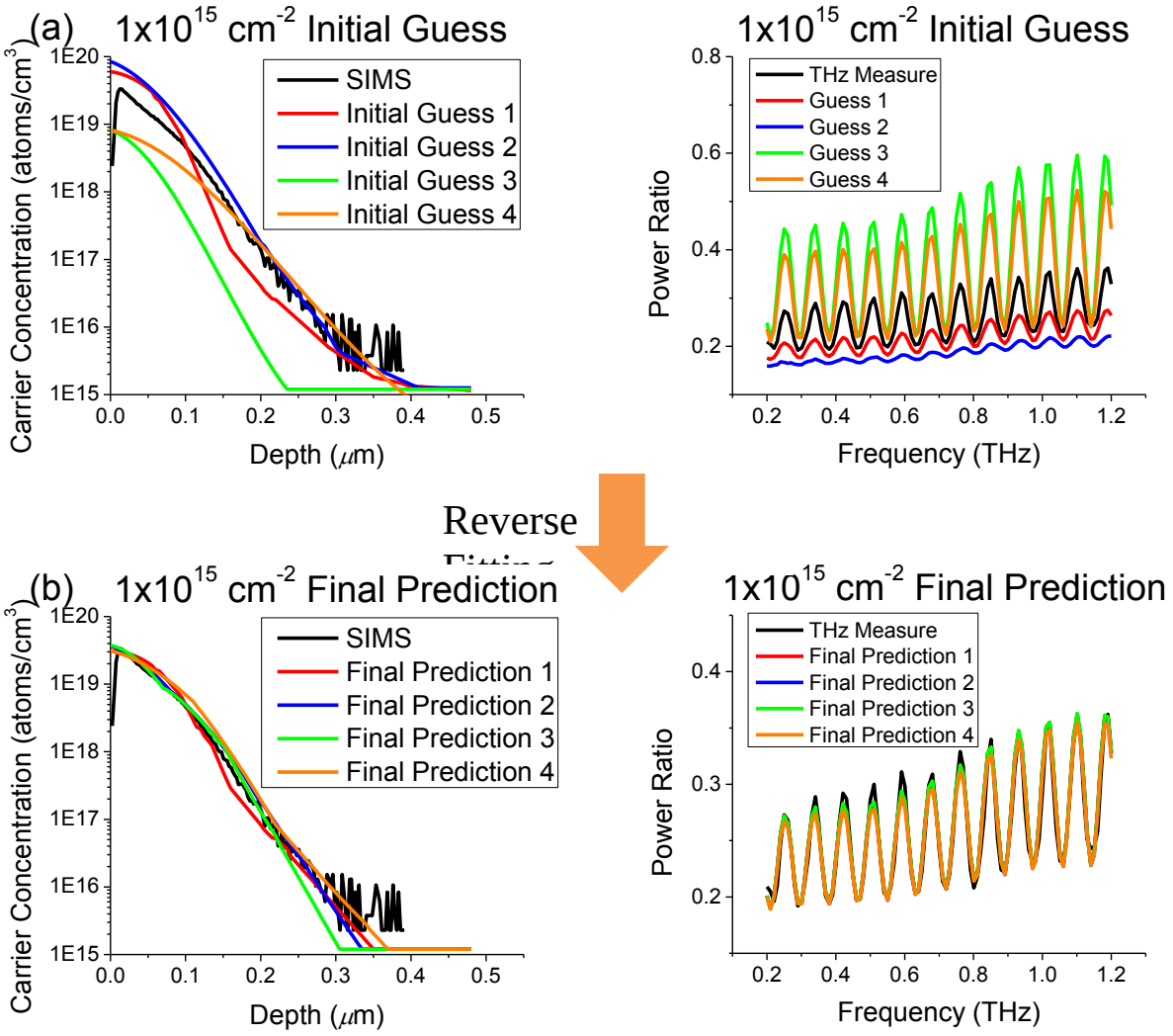

Figure 7.14 Reverse doping profile prediction on the 1×10^{15} cm^{-2} RTP sample using 4 guess profiles from two cases described in the step 1 of Figure 7.11. Two guess profiles in case 1 have been demonstrated in Figure 7.12 and 7.13. Another two guess profiles in case 2 are new made ones for the continuous demonstration.

7.4 Conclusions

We experimentally demonstrated that the transmission mode THz-TDS can be used to map the phosphorus doping profile electrically in a non-contact manner. Compared to other non-contact techniques, the profile we generated has the advantage of reflecting a more accurate electrical performance in THz regions. Using the new derived equation and empirical refractive index information, the estimated power transmission ratios match well to the THz measurements with acceptable measurement uncertainties. There is no omnipotent model to cover various initial guess profiles. To deal with the specific effect from the ion implantation process, the "Stanford Full Coupled Model" and known SIMS profiles are adopted as initial guess profiles in the reverse fitting process and prove a better feature prediction using known SIMS profiles. The strategy is Figure 7.11 is proposed to approach an unknown profile as close as possible and its feasibility is demonstrated using three various profiles. From the system design point of view, a THz-TDS can be designed as a monitor metrology right after the diffusion or ion implantation process stage and feedbacks the real-time measured change for the process parameter compensation.

We also demonstrated that the transmission mode THz-TDS combined with the anodic oxidation technique can be used to map the phosphorus doping profile electrically in a destructive manner. The experimental result indicates that estimated power transmission ratios match well with the THz measurements in all cycle samples. From the system design point of view, other techniques, which own the same or even better thickness resolution, can be considered as alternative options. Reverse mapping and weighted average are two proposed ideas demonstrate the doping profile construction. The reverse mapping uses a straight forward concept to construct a doping profile in a reverse sequence. The result indicates a significant

discrepancy in heavily doped regions, which can be interpreted by the effect from inactive atoms. The weighted average concept also achieves a closer profile prediction to the SIMS measurement. However, the profile construction from Irvine's curves doesn't show a comparable performance due to the improper assumption. The relative stand-alone system can be designed to measure the doping profile remotely like other destructive techniques. The transmission mode schematic will be only applicable for samples with THz survived after the penetration of THz radiation.

8 CONCLUSIONS

In this dissertation, the psychological journey of the silicon doping profile measurement using a typical terahertz time domain spectroscopy is lucidly displayed from the bottom-up. Compared to existing destructive and developing non-contact techniques, this new approach opens the doors of *in-situ* process monitor and stand-alone profile characterization, which are urgent to industries [104]. Chapter 1 and 2 principally describe a whole picture of this research by listing the pro's and con's of existing techniques, reviewing the historical development of THz technique as well as usages in semiconductor fields and introducing theories required for this research. Contributions and extensions from this research are summarized individually in Chapter 3 to 7, followed by the current research status and future work.

8.1 Silicon Thickness Determination using THz-TDS

Chapter 3 explored resolutions of all indices from a time-domain THz measurement to determine the thickness in a lightly doped silicon wafer. The research motivation of this fundamental study originated from the utilized transmission mode THz-TDS, the bulk silicon wafer and the transfer matrix method. To identify accurate resolutions, signal-to-noise ratio and measurement uncertainty of lab setup THz-TDS were characterized in detail to calculate relative standard variations. Resolutions were summarized in Table 3.2 and the frequency shift of Fabry-Pérot resonant peak is chosen in the following researches due to its sub-micron resolution.

Similar studies, which are close to this topic, are generally found regarding the measurement uncertainty, thickness determination on various materials or industrial implementation using cost-effective photo-mixing system. However, none of them performed the

same systematic study like us in lightly doped silicon. **The work in Chapter 3 establishes the standard procedure of studying the resolution limit of thickness determination for various materials.** Different resolutions are expected on other materials due to their intrinsic refractive indices. Chapter 3 limits the study using the transmission mode system and neglects the index dispersion. Studies on materials containing frequency-dependent index dispersion could be extensions to research.

8.2 Silicon Doping Profile Recognition using THz-TDS

The work presented in Chapter 4 concentrated on the demonstration of silicon profile recognition using THz-TDS. The definition of the word "recognition" indicates the necessity of a reference (golden) profile in the practical application. This conceptual study displayed the recognition ability in distinct n/p-type doping profiles and presented a detectable THz absorption under the slightly changed process condition. On the other hand, the ability to overcome the surface morphology and replace four-point probe technology were also presented physically. The immediate thought to this result is the application of an *in-situ* process monitor.

This topic was not investigated in deep since our main focus is the doping profile prediction. Therefore, the actual resolution of profile recognition, the way to utilize information in the 2nd peak and the absorption differences in other dopants were left as future work. Since the 2nd peak information results from the combination of both silicon wafer and GaAs chip in the THz emitter with a close thickness (~500μm), the pure information in the frequency domain can be obtained using a thinner silicon wafer (say 200-400μm). **Chapter 4 not only succeeds the fundamental study towards to the final research, but also achieves the practical industrial application: *in-situ* process monitor.** This promising result gave us the confidence to continuously research the final research goal.

8.3 Phosphorus Refractive Index Extraction using THz-TDS

The work presented in Chapter 5 focused on the strategy and display of phosphorus refractive index from 0.2 to 8 THz in carrier concentration levels 10^{15} cm^{-3} to 2×10^{20} cm^{-3} under a room temperature measurement. Until now, experimental phosphorus refractive index > 10^{19} cm^{-3} in regions has not been reported due to the survival of THz radiation in heavily doped and thick samples as well as the shortage of practical motivation. The SOI wafer builds up a paragon to study materials with high THz absorption in the transmission mode system. This analytical strategy can be applied to different dopants in various semiconductor materials.

The specialty of this topic was the effort we put to pursue the data accuracy. Data from two THz systems in two different labs showed a perfect agreement (overlap) to each other. On the other hand, carrier concentrations in all seven samples were checked carefully by four different characterization techniques (five tools) from four specific places. The extracted refractive index surprisingly follows the classic Drude Model prediction but has a small offset.

This offset motivated us to study the underground mechanism, which is beyond our original purpose, and found the reasonable interpretation from the impurity band theory (electrons in the impurity band have heavier effective masses) and THz emissions. Our data suggests the initial observation of this effect at room temperature and the change under a temperature cooling process could be future work to study.

Chapter 5 demonstrates an analytical strategy to collect phosphorus refractive index in THz regions. The result not only provides the key information to our final research, but also opens the door of the impurity band study using THz-TDS.

8.4 Non-Contact and Destructive Doping Profile Prediction using THz-TDS

Chapter 3-5 have collected vital information through intensively fundamental studies. Prior to the experimental demonstration in Chapter 7, the numerical simulation was done in Chapter 6 to study the problem of multiple degeneracy in detail.

In Chapter 6, all empirical equations other than theoretical models applied for the doping profile prediction were introduced, followed by the study of multiple degeneracy problem through the numerical simulation. Fortunately we don't have the theoretical degeneracy to totally destroy our final research goal but the practical degeneracy do cause the potential of fake solutions. The existence of the practical degeneracy was also experimentally demonstrated by five ion implanted profiles. **Chapter 6 mainly excludes the existence of the theoretical degeneracy, which leads the failure of the whole research. To shrink or break the practical degeneracy, complex THz reflection would be helpful information to use.**

In Chapter 7, two conceptual demonstrations were performed to achieve a non-contact and destructive doping profile prediction using THz-TDS. The calibration of the refractive index library from Chapter 5 was firstly proven using distinct SIMS profiles. Then this library and the "ML-Two Peaks" equation were applied in the transfer matrix to predict doping profiles experimentally. In the demonstration of the destructive profile prediction, the anodic oxidation process showed the ability of an uniform silicon removal and outstanding thickness control. Changes of THz radiation in all cycles were accurately predicted and the reversely constructed doping profile matched its SIMS measurement very well. From the system design point of view, any technique with an outstanding Si removal control can be incorporated. In the demonstration of the non-contact profile prediction, both known SIMS profile and process simulator are proven as good sources to generate the initial guess profile. By the use of the proposed fitting strategy,

predicted doping profiles are close to various SIMS measurements again. The profile discrepancy in heavily doped regions also indicates the effect of inactive dopants between chemical and electrical profiles. **Chapter 7 conceptually displays the doping profile prediction in both destructive and non-contact manners. In the non-contact profile prediction, the practical degeneracy problem is the bottleneck to find the right profile in the transmission mode system. Many efforts can be thought of eliminate this uncertain factor.**

In conclusion, all conceptual demonstrations in Chapter 7 have displayed the potential of competing existing commercial and developing techniques to achieve the doping profile measurement. The original motivation of the THz-TDS approach is designed for the purpose of an *in-situ* process monitor. From the commercialization point of view, maybe the destructive approach will be quicker to be implemented.

8.5 Future work

The work presented in this dissertation is concentrated on the four important applications using a typical THz-TDS, including material thickness determination, doping profile recognition, refractive index extraction in heavily doped materials and non-contact as well as destructive doping profile predictions. There is certainly a huge scope for further development on several aspects of the work. Below are some directions which could be followed up:

1. Conceptual demonstration of the non-contact profile prediction through the proposed strategy has been performed semi-automatically in Chapter 7. The next step would be the implementation of profile prediction using automatic algorithms. Many ideas can be investigated over here, including the selection of proper mathematical models for distinct

doping features, the trial of existing mathematical algorithms, the creation of new reverse algorithms, various constraints for different algorithms, and the programming efforts required for various algorithms.

2. The practical degeneracy has been pointed out as the major problem in the non-contact profile prediction. Strategies to break and shrink the practical degeneracy such as utilizing information from reflected THz system, reducing the measurement uncertainty, choosing constraints for different algorithms and innovating advanced reverse algorithms can be important future work to study.

3. The performance regarding the destructive doping profile measurement looks promising in the initial demonstration to compete with existing destructive techniques. The next step could be the study of the prediction resolution, the selection of the technique for Si removal, the overall system design and the future commercialization.

4. In this dissertation, several extensions, mentioned in Chapter 3-5, can be individualized as research topics. The analytical procedure in Chapter 3 can be applied to research the same thickness resolutions in various materials with different intrinsic doping levels. The profile recognition in Chapter 4 can be extended to other dopants and compare their resolutions to phosphorus and boron dopants. The strategy in Chapter 5 can be applied to extend libraries from other dopants. All these extensions will broaden practical applications in semiconductor industries using novel THz techniques.

9 PUBLICATIONS

9.A Peer reviewed journals:

1. **C. Jen**, and C. Richter, "Sample Thickness Measurement with THz-TDS: Resolution and Implications", *Journal of Infrared, Millimeter, and Terahertz Waves,* Vol. 35, Issue 10, 2014.

2. **C. Jen**, and C. Richter, "Doping Profile Recognition Applied to Silicon Photovoltaic Cells Using Terahertz Time-Domain Spectroscopy", *Terahertz Science and Technology, IEEE Transactions on,* Vol. 4, Issue 5, pp. 560-567, 2014.

3. **C. Jen**, and C. Richter, "Terahertz refractive Index of Doped Silicon", *Science,* **submission scheduled in Dec**.

4. **C. Jen**, and C. Richter, "Doping Profile Mapping in Silicon using Terahertz Time Domain Spectroscopy – Part I: Non-Contact Profile Prediction", *Terahertz Science and Technology, IEEE Transactions on,* **submission scheduled in Dec**.

5. Gaurav Tulsyan, **C. Jen**, and C. Richter, "Doping Profile Mapping in Silicon using Terahertz Time Domain Spectroscopy – Part II: Destructively Anodic Oxidation", *Terahertz Science and Technology, IEEE Transactions on,* **submission scheduled in Dec**.

6. **C. Jen**, and C. Richter, "Doping Profile Mapping in Silicon using Terahertz Time Domain Spectroscopy – Part III: Study of Multiple Degeneracy", *Terahertz Science and Technology, IEEE Transactions on,* **submission scheduled in Dec**.

9.B Conferences:

1. **C. Jen**, and C. Richter, “Silicon wafer thickness measurement using terahertz time domain spectroscopy”, Proc. SPIE, vol. 8984, Ultrafast Phenomena and Nanophotonics XVIII, 898414, 2014.
2. **C. Jen**, and C. Richter, “Doping profile recognition in silicon using terahertz time-domain spectroscopy”, Proc. SPIE, vol. 8985, Terahertz, RF, Millimeter, and Submillimeter-Wave Technology and Applications VII, 89850M, 2014.
3. **C. Jen**, and C. Richter, “Accurate simulation of terahertz transmission through doped silicon junctions”, SPIE Paper Number 9361-53, Ultrafast Phenomena and Nanophotonics XIX, 2015, **Oral presentation accepted**.
4. **C. Jen**, and C. Richter, “Demonstration of high-resolution doping profile mapping using terahertz time domain spectroscopy with electrochemical anodization”, SPIE Paper Number 9362-25, Terahertz, RF, Millimeter and sub-millimeter wave Technology and Application VIII, 2015, **Oral presentation accepted**.
5. B. McNamara, **C. Jen**, C. Richter, “The terahertz refractive index of p-type silicon”, OTST 2015, **Application in review**.
6. G. Tulsyan, **C. Jen**, J. Dai, X. –C. Zhang, C. Richter, “The terahertz refractive index of doped silicon”, OTST 2015, **Application in review**.
7. S. Kurinec, **C. Jen**, G. Tulsyan, C. Richer, “Terahertz time-domain spectroscopy for characterization of doping profiles in semiconductors”, NIST FCMN 2015, **Application in review**.

9.C Patents:

1 **C. Jen**, and C. Richter, "Doping profile measurement of semiconductor devices using Terahertz Time Domain Spectroscopy (THz-TDS)", USPTO, Application No. 62/079262.

9.D Posters:

1. C. W. McMurtry, J. L. Pipher, M. V. Bocko, Z. Ignjatovic, J. Dai, X.-C. Zhang, Z. Ninkov, K. D. Fourspring, C. Richter, **C. Jen**, J. D. Newman, Paul Lee, A. P. Sacco, T. Chamberlain, D. A. Willems, R. Fiete, "Preliminary Imaging Tests at THz Frequencies", 2013 CEIS
2. G. Tulsyan, **C. Jen**, C. Richter, "Doping profile mapping using Terahertz Spectroscopy (THz-TDS) via Anodization", 2014 MRS Fall.

10 REFERENCES

[1] M. Naruse, Y. Sekimoto, T. Suzuki, Y. Hibi, H. Matsuo, Y. Uzawa, *et al.*, "Design of SIS imaging array for terahertz astronomy," in *Infrared, Millimeter, and Terahertz Waves, 2009. IRMMW-THz 2009. 34th International Conference on*, 2009, pp. 1-2.

[2] E. Peiner, A. Schlachetzki, and D. Krüger, "Doping Profile Analysis in Si by Electrochemical Capacitance - Voltage Measurements," *J. Electrochem. Soc.*, vol. 142, pp. pp. 576-580, 1995.

[3] E. Pickwell-MacPherson, "Biomedical applications of terahertz pusled imaging and spectroscopy," in *Medical Devices and Biosensors, 2008. ISSS-MDBS 2008. 5th International Summer School and Symposium on*, 2008, pp. 15-15.

[4] A. J. Fitzgerald, E. Berry, N. N. Zinovev, G. C. Walker, M. A. Smith, and J. M. Chamberlain, "An introduction to medical imaging with coherent terahertz frequency radiation," *Physics in Medicine and Biology*, vol. 47, p. R67, 2002.

[5] K. Humphreys, J. P. Loughran, M. Gradziel, W. Lanigan, T. Ward, J. A. Murphy, *et al.*, "Medical applications of terahertz imaging: a review of current technology and potential applications in biomedical engineering," in *Engineering in Medicine and Biology Society, 2004. IEMBS '04. 26th Annual International Conference of the IEEE*, 2004, pp. 1302-1305.

[6] M. Schirmer, M. Fujio, M. Minami, J. Miura, T. Araki, and T. Yasui, "Biomedical applications of a real-time terahertz color scanner," *Biomedical Optics Express*, vol. 1, pp. 354-366, 2010/09/01 2010.

[7] J.-j. Luo, S.-x. Hou, J. Xu, and J.-j. Li, "Study on applications of terahertz technology," 2007, pp. 662203-662203-7.

[8] N. S. Kopeika, A. Abramovich, O. Yadid-Pecht, Y. Yitzhaky, A. Belenky, S. Lineykin, *et al.*, "Relatively inexpensive terahertz imaging," in *Electrical and Electronics Engineers in Israel, 2008. IEEEI 2008. IEEE 25th Convention of*, 2008, pp. 137-141.

[9] R. M. Woodward, "Terahertz technology in global homeland security (Invited Paper)," 2005, pp. 22-31.

[10] D. Etayo, J. C. Iriarte, I. Palacios, I. Maestrojuan, J. Teniente, I. Ederra, *et al.*, "THz imaging system for industrial quality control," in *Microwave Workshop Series on Millimeter Wave Integration Technologies (IMWS), 2011 IEEE MTT-S International*, 2011, pp. 172-175.

[11] F. Rutz, M. Koch, S. Khare, M. Moneke, H. Richter, and U. Ewert, "Tetahertz quality control of polymeric products," *International Journal of Infrared and Millimeter Waves*, vol. 27, pp. 547-556, 2006/04/01 2006.

[12] P. Dean, A. Valavanis, A. Scheuring, A. Stockhausen, P. Probst, M. Salih, *et al.*, "Ultra-fast sampling of terahertz pulses from a quantum cascade laser using superconducting antenna-coupled NbN and YBCO detectors," in *Infrared, Millimeter, and Terahertz Waves (IRMMW-THz), 2012 37th International Conference on*, 2012, pp. 1-2.

[13] T. Masayoshi, "Cutting-edge terahertz technology," *Nature Photonics*, vol. 1, pp. 97-105, 2007.

[14] P. U. Jepsen, D. G. Cooke, and M. Koch, "Terahertz spectroscopy and imaging – Modern techniques and applications," *Laser & Photonics Reviews,* vol. 5, pp. 124-166, 2011.
[15] M. Asada and S. Suzuki, "Terahertz oscillators using electron devices — an approach with Resonant tunneling diodes," *IEICE Electronics Express,* vol. 8, pp. 1110-1126, 2011.
[16] S. Komiyama, "Single-Photon Detectors in the Terahertz Range," *Selected Topics in Quantum Electronics, IEEE Journal of,* vol. 17, pp. 54-66, 2011.
[17] H. Ruonan, Z. Yaming, K. Youngwan, K. Dae Yeon, H. Shichijo, and K. O. Kenneth, "Terahertz image sensors using CMOS Schottky barrier diodes," in *SoC Design Conference (ISOCC), 2012 International*, 2012, pp. 254-257.
[18] F. Bradley and Z. Xi-Cheng, "Materials for terahertz science and technology," *Nature Materials,* vol. 1, pp. 26-33, 2002.
[19] P. H. Siegel, "Terahertz technology," *Microwave Theory and Techniques, IEEE Transactions on,* vol. 50, pp. 910-928, 2002.
[20] J. A. Eikelboom, *Microwave Detection of Minority Carriers in Solar Cell Silicon Wafers*: Netherlands Energy Research Foundation ECN, 1995.
[21] S. Belfer, R. Fainchtain, Y. Purinson, and O. Kedem, "Surface characterization by FTIR-ATR spectroscopy of polyethersulfone membranes-unmodified, modified and protein fouled," *Journal of Membrane Science,* vol. 172, pp. 113-124, 7/1/ 2000.
[22] G. L. Liu, H. Uchida, I. Aikawa, S. Kuroda, and N. Hirashita, "Accurate secondary ion mass spectrometry analysis of shallow doping profiles in Si based on the internal standard method," *Journal of Vacuum Science & Technology B: Microelectronics and Nanometer Structures,* vol. 14, pp. 324-328, 1996.
[23] R. Zelsacher, A. C. G. Wood, E. Bacher, E. Prax, K. Sorschag, J. Krumrey, *et al.*, "A novel SIMS based approach to the characterization of the channel doping profile of a trench MOSFET," *Microelectronics Reliability,* vol. 47, pp. 1585-1589, 9// 2007.
[24] R. Mathur, "Dopant profile extraction from spreading resistance measurements," *Journal of Vacuum Science & Technology B,* vol. 10, pp. 421-425, 1992.
[25] E. Ishida and S. B. Felch, "Study of electrical measurement techniques for ultra‐shallow dopant profiling," *Journal of Vacuum Science & Technology B: Microelectronics and Nanometer Structures,* vol. 14, pp. 397-403, 1996.
[26] W. Hui-Zhen, R. Guo-Ping, C. G. Jin, B. Mizuno, J. Yu-Long, Q. Xin-Ping, *et al.*, "ECV Profiling of Ultra-Shallow Junction Formed by Plasma Doping," in *Junction Technology, 2006. IWJT '06. International Workshop on*, 2006, pp. 120-122.
[27] A. Bentzen and A. Holt, "Correspondence between sheet resistance and emitter profile of phosphorus diffused emitters from a spray-on dopant," in *Photovoltaic Specialists Conference, 2005. Conference Record of the Thirty-first IEEE*, 2005, pp. 1153-1156.
[28] J. Hilibrand and R. D. Gold, "Determination of the Impurity Distribution in Junction Diodes From Capacitance-Voltage Measurements," *RCA Review,* vol. 21, pp. 245-252, 1960.
[29] P. Barnes, "Capacitance–Voltage (C-V) Characterization Of Semiconductors," in *Characterization of Materials*, ed: John Wiley & Sons, Inc., 2002.
[30] J. Olsson, R. Valtonen, U. Heinle, L. Vestling, A. Soderbarg, and H. Norde, "A capacitance-voltage measurement method for DMOS transistor channel length extraction," in *Microelectronic Test Structures, 1999. ICMTS 1999. Proceedings of the 1999 International Conference on*, 1999, pp. 135-140.

[31] S. Ko and M. Kohno, "Application of non-contact C-V measurement in evaluation of ion implantation induced wafer charging," in *Ion Implantation Technology. 2002. Proceedings of the 14th International Conference on*, 2002, pp. 295-298.

[32] S. Takamasa, K. Motohiro, H. Sadao, N. Ikuyoshi, and K. Tatsufumi, "Noncontact, Electrode-free Capacitance/Voltage Measurement Based on General Theory of Metal-Oxide-Semiconductor (MOS) Structure," *Japanese Journal of Applied Physics,* vol. 32, p. 4005, 1993.

[33] L. S. Tan, L. C. P. Tan, M. S. Leong, R. G. Mazur, and C. W. Ye, "Characterization of ultrashallow dopant profiles using spreading resistance profiling," *Journal of Vacuum Science & Technology B,* vol. 20, pp. 483-487, 2002.

[34] M. Neshat and N. Armitage, "Terahertz time-domain spectroscopic ellipsometry: instrumentation and calibration," *Optics express,* vol. 20, pp. 29063-29075, 2012.

[35] T. Hofmann, C. M. Herzinger, A. Boosalis, T. E. Tiwald, J. A. Woollam, and M. Schubert, "Variable-wavelength frequency-domain terahertz ellipsometry," *The Review of scientific instruments,* vol. 81, p. 023101, 2010.

[36] Z. Liu, Y. Zhang, S. W. Kok, B. P. Ng, and Y. C. Soh, *Reflection-based near-field ellipsometry for thin film characterization* vol. 124C, 2012.

[37] M. van Exter, C. Fattinger, and D. Grischkowsky, "Terahertz time-domain spectroscopy of water vapor," *Optics Letters,* vol. 14, pp. 1128-1130, 1989/10/15 1989.

[38] S. Nashima, O. Morikawa, K. Takata, and M. Hangyo, "Measurement of optical properties of highly doped silicon by terahertz time domain reflection spectroscopy," *Applied Physics Letters,* vol. 79, pp. 3923-3925, 2001.

[39] A. Pashkin, M. Kempa, H. Nemec, F. Kadlec, and P. Kuzel, "Phase-sensitive time-domain terahertz reflection spectroscopy," *Review of Scientific Instruments,* vol. 74, pp. 4711-4717, 2003.

[40] D. H. Auston, "Picosecond optoelectronic switching and gating in silicon," *Applied Physics Letters,* vol. 26, pp. 101-103, 1975.

[41] D. Jianming, L. Jingle, and Z. Xi-Cheng, "Terahertz Wave Air Photonics: Terahertz Wave Generation and Detection With Laser-Induced Gas Plasma," *Selected Topics in Quantum Electronics, IEEE Journal of,* vol. 17, pp. 183-190, 2011.

[42] C. A. Schmuttenmaer, "Exploring Dynamics in the Far-Infrared with Terahertz Spectroscopy," *Chemical Reviews,* vol. 104, pp. 1759-1780, 2004/04/01 2004.

[43] R. D. Averitt and A. J. Taylor, "Ultrafast optical and far-infrared quasiparticle dynamics in correlated electron materials," *Journal of Physics: Condensed Matter,* vol. 14, p. R1357, 2002.

[44] H. Němec, P. Kužel, and V. Sundström, "Charge transport in nanostructured materials for solar energy conversion studied by time-resolved terahertz spectroscopy," *Journal of Photochemistry and Photobiology A: Chemistry,* vol. 215, pp. 123-139, 9/25/ 2010.

[45] J. B. Baxter and G. G.W., "Terahertz Spectroscopy. ," *Analytical Chemistry,* vol. 83, pp. 4342-4368, 2011.

[46] R. Ulbricht, E. Hendry, J. Shan, T. F. Heinz, and M. Bonn, "Carrier dynamics in semiconductors studied with time-resolved terahertz spectroscopy," *Reviews of Modern Physics,* vol. 83, pp. 543-586, 06/03/ 2011.

[47] D. N. Basov, R. D. Averitt, D. van der Marel, M. Dressel, and K. Haule, "Electrodynamics of correlated electron materials," *Reviews of Modern Physics,* vol. 83, pp. 471-541, 06/02/ 2011.

[48] A. Adam, "Review of Near-Field Terahertz Measurement Methods and Their Applications," *Journal of Infrared, Millimeter, and Terahertz Waves,* vol. 32, pp. 976-1019, 2011/09/01 2011.
[49] J. Lloyd-Hughes and T.-I. Jeon, "A Review of the Terahertz Conductivity of Bulk and Nano-Materials," *Journal of Infrared, Millimeter, and Terahertz Waves,* vol. 33, pp. 871-925, 2012/09/01 2012.
[50] E. R. Brown, K. A. McIntosh, K. B. Nichols, and C. L. Dennis, "Photomixing up to 3.8 THz in low - temperature - grown GaAs," *Applied Physics Letters,* vol. 66, pp. 285-287, 1995.
[51] K. A. McIntosh, E. R. Brown, K. B. Nichols, O. B. McMahon, W. F. DiNatale, and T. M. Lyszczarz, "Terahertz photomixing with diode lasers in low - temperature - grown GaAs," *Applied Physics Letters,* vol. 67, pp. 3844-3846, 1995.
[52] F. Hindle, A. Cuisset, R. Bocquet, and G. Mouret, "Continuous-wave terahertz by photomixing: applications to gas phase pollutant detection and quantification," *Comptes Rendus Physique,* vol. 9, pp. 262-275, 3// 2008.
[53] H. Hamster, A. Sullivan, S. Gordon, W. White, and R. W. Falcone, "Subpicosecond, electromagnetic pulses from intense laser-plasma interaction," *Physical Review Letters,* vol. 71, pp. 2725-2728, 10/25/ 1993.
[54] D. J. Cook and R. M. Hochstrasser, "Intense terahertz pulses by four-wave rectification in air," *Optics Letters,* vol. 25, pp. 1210-1212, 2000/08/15 2000.
[55] M. Kress, T. Löffler, S. Eden, M. Thomson, and H. G. Roskos, "Terahertz-pulse generation by photoionization of airwith laser pulses composed of both fundamental and second-harmonicwaves," *Optics Letters,* vol. 29, pp. 1120-1122, 2004/05/14 2004.
[56] T. Bartel, P. Gaal, K. Reimann, M. Woerner, and T. Elsaesser, "Generation of single-cycle THz transients with high electric-field amplitudes," *Optics Letters,* vol. 30, pp. 2805-2807, 2005/10/15 2005.
[57] X. Xie, J. Dai, and X. C. Zhang, "Coherent Control of THz Wave Generation in Ambient Air," *Physical Review Letters,* vol. 96, p. 075005, 02/23/ 2006.
[58] D. J. Cook, J. X. Chen, E. A. Morlino, and R. M. Hochstrasser, "Terahertz-field-induced second-harmonic generation measurements of liquid dynamics," *Chemical Physics Letters,* vol. 309, pp. 221-228, 8/13/ 1999.
[59] J. Dai, X. Xie, and X. C. Zhang, "Detection of Broadband Terahertz Waves with a Laser-Induced Plasma in Gases," *Physical Review Letters,* vol. 97, p. 103903, 09/08/ 2006.
[60] P. Drude, "Zur Elektronentheorie der Metalle," *Annalen der Physik,* vol. 306, pp. 566-613, 1900.
[61] T.-I. Jeon and D. Grischkowsky, "Nature of Conduction in Doped Silicon," *Physical Review Letters,* vol. 78, pp. 1106-1109, 02/10/ 1997.
[62] T.-I. Jeon and D. Grischkowsky, "Characterization of optically dense, doped semiconductors by reflection THz time domain spectroscopy," *Applied Physics Letters,* vol. 72, pp. 3032-3034, 1998.
[63] M. C. Beard, G. M. Turner, and C. A. Schmuttenmaer, "Transient photoconductivity in GaAs as measured by time-resolved terahertz spectroscopy," *Physical Review B,* vol. 62, pp. 15764-15777, 2000.
[64] N. V. Smith, "Drude theory and the optical properties of liquid mercury," *Physics Letters A,* vol. 26, pp. 126-127, 1/1/ 1968.

[65] N. V. Smith, "Classical generalization of the Drude formula for the optical conductivity," *Physical Review B,* vol. 64, p. 155106, 09/20/ 2001.
[66] L. Duvillaret, F. Garet, and J.-L. Coutaz, "Highly Precise Determination of Optical Constants and Sample Thickness in Terahertz Time-Domain Spectroscopy," *Applied Optics,* vol. 38, pp. 409-415, 1999/01/10 1999.
[67] B. B. Jason and A. S. Charles, "Time-Resolved Terahertz Spectroscopy and Terahertz Emission Spectroscopy," in *Terahertz Spectroscopy*, ed: CRC Press, 2007, pp. 73-118.
[68] I. Pupeza, R. Wilk, and M. Koch, "Highly accurate optical material parameter determination with THz time-domain spectroscopy," *Optics Express,* vol. 15, pp. 4335-4350, 2007/04/02 2007.
[69] T. D. Dorney, R. G. Baraniuk, and D. M. Mittleman, "Material parameter estimation with terahertz time-domain spectroscopy," *Journal of the Optical Society of America A,* vol. 18, pp. 1562-1571, 2001/07/01 2001.
[70] H. Babar, N. Muhammad, A. Mushtaq, and M. Y. A. Raja, "Measurement of thickness and refractive index using femtosecond and terahertz pulses," *Laser Physics Letters,* vol. 10, p. 055301, 2013.
[71] L. Duvillaret, F. Garet, and J.-L. Coutaz, "Influence of noise on the characterization of materials by terahertz time-domain spectroscopy," *Journal of the Optical Society of America B,* vol. 17, pp. 452-461, 2000/03/01 2000.
[72] L. Duvillaret, F. Garet, and J. L. Coutaz, "A reliable method for extraction of material parameters in terahertz time-domain spectroscopy," *Selected Topics in Quantum Electronics, IEEE Journal of,* vol. 2, pp. 739-746, 1996.
[73] L. Duvillaret, F. Garet, J. F. Roux, and J. L. Coutaz, "Analytical modeling and optimization of terahertz time-domain spectroscopy experiments, using photoswitches as antennas," *Selected Topics in Quantum Electronics, IEEE Journal of,* vol. 7, pp. 615-623, 2001.
[74] M. Naftaly, R. A. Dudley, J. R. Fletcher, F. Bernard, C. Thomson, and Z. Tian, "Frequency calibration of terahertz time-domain spectrometers," *Journal of the Optical Society of America B,* vol. 26, pp. 1357-1362, 2009/07/01 2009.
[75] W. Withayachumnankul, B. M. Fischer, and D. Abbott, "Material thickness optimization fortransmission-modeterahertz time-domain spectroscopy," *Optics Express,* vol. 16, pp. 7382-7396, 2008/05/12 2008.
[76] W. Withayachumnankul, B. M. Fischer, H. Lin, and D. Abbott, "Uncertainty in terahertz time-domain spectroscopy measurement," *Journal of the Optical Society of America B,* vol. 25, pp. 1059-1072, 2008/06/01 2008.
[77] S. E. Ralph, S. Perkowitz, N. Katzenellenbogen, and D. Grischkowsky, "Terahertz spectroscopy of optically thick multilayered semiconductor structures," *Journal of the Optical Society of America B,* vol. 11, pp. 2528-2532, 1994/12/01 1994.
[78] M. Theuer, R. Beigang, and D. Grischkowsky, "Highly sensitive terahertz measurement of layer thickness using a two-cylinder waveguide sensor," *Applied Physics Letters,* vol. 97, pp. 071106-071106-3, 2010.
[79] R. Wilk, I. Pupeza, R. Cernat, and M. Koch, "Highly Accurate THz Time-Domain Spectroscopy of Multilayer Structures," *Selected Topics in Quantum Electronics, IEEE Journal of,* vol. 14, pp. 392-398, 2008.
[80] R. A. Cheville, "Terahertz Time-Domain Spectroscopy with Photoconductive Antennas," in *Terahertz Spectroscopy*, ed: CRC Press, 2007, pp. 1-39.

[81] M. Van Exter and D. Grischkowsky, "Characterization of an optoelectronic terahertz beam system," *Microwave Theory and Techniques, IEEE Transactions on,* vol. 38, pp. 1684-1691, 1990.
[82] A. B. True and Y. University, *Terahertz Spectroscopy of Amino Acid Enantiomers and Polymorphs*: Yale University, 2008.
[83] M. Naftaly, "Metrology Issues and Solutions in THz Time-Domain Spectroscopy: Noise, Errors, Calibration," *Sensors Journal, IEEE,* vol. 13, pp. 8-17, 2013.
[84] S. P. Mickan, K.-S. Lee, T.-M. Lu, J. Munch, D. Abbott, and X. C. Zhang, "Double modulated differential THz-TDS for thin film dielectric characterization," *Microelectronics Journal,* vol. 33, pp. 1033-1042, 12// 2002.
[85] J. Balakrishnan, B. M. Fischer, and D. Abbott, "Low noise spinning wheel technique for THz material parameter extraction," *Optics Communications,* vol. 283, pp. 2301-2307, 5/15/ 2010.
[86] M. R. Williams, A. F. True Ab Fau - Izmaylov, T. A. Izmaylov Af Fau - French, K. French Ta Fau - Schroeck, C. A. Schroeck K Fau - Schmuttenmaer, and C. A. Schmuttenmaer, "Terahertz spectroscopy of enantiopure and racemic polycrystalline valine," *Phys Chem Chem Phys.,* 20110616 DCOM- 20111004 2011.
[87] S. Mittleman Dm Fau - Hunsche, L. Hunsche S Fau - Boivin, M. C. Boivin L Fau - Nuss, and M. C. Nuss, "T-ray tomography," *Optics Letters,* vol. 22, pp. 904-906, 20080110 DCOM- 20121002 1997.
[88] C. Wai Lam, D. Jason, and M. M. Daniel, "Imaging with terahertz radiation," *Reports on Progress in Physics,* vol. 70, p. 1325, 2007.
[89] T. Yasui, T. Yasuda, K.-i. Sawanaka, and T. Araki, "Terahertz paintmeter for noncontact monitoring of thickness and drying progress in paint film," *Applied Optics,* vol. 44, pp. 6849-6856, 2005/11/10 2005.
[90] M. Haaser, K. C. Gordon, C. J. Strachan, and T. Rades, "Terahertz pulsed imaging as an advanced characterisation tool for film coatings—A review," *International Journal of Pharmaceutics,* vol. 457, pp. 510-520, 12/5/ 2013.
[91] L. Ho, R. Müller, M. Römer, K. C. Gordon, J. Heinämäki, P. Kleinebudde, *et al.*, "Analysis of sustained-release tablet film coats using terahertz pulsed imaging," *Journal of Controlled Release,* vol. 119, pp. 253-261, 6/22/ 2007.
[92] J. A. Zeitler, C. Shen Y Fau - Baker, P. F. Baker C Fau - Taday, M. Taday Pf Fau - Pepper, T. Pepper M Fau - Rades, and T. Rades, "Analysis of coating structures and interfaces in solid oral dosage forms by three dimensional terahertz pulsed imaging," *Journal of Pharmaceutical Science,* vol. 96, pp. 330-340, 20070103 DCOM- 20070410 2007.
[93] I.-S. Russe, D. Brock, K. Knop, P. Kleinebudde, and J. A. Zeitler, "Validation of Terahertz Coating Thickness Measurements Using X-ray Microtomography," *Molecular Pharmaceutics,* vol. 9, pp. 3551-3559, 2012/12/03 2012.
[94] D. Brock, A. Zeitler Ja Fau - Funke, K. Funke A Fau - Knop, P. Knop K Fau - Kleinebudde, and P. Kleinebudde, "A comparison of quality control methods for active coating processes," *International Journal of Pharmaceutics,* vol. 439, pp. 289-295, 20121119 DCOM- 20130507 2012.
[95] J. Ikram, U. o. N. C. a. C. D. o. Physics, O. S. O. Science, and Engineering, *Terahertz Time of Flight Detection for Absolute Thickness Measurement of Single Side Polished Silicon Wafers*: University of North Carolina at Charlotte, 2010.

[96] A. J. L. Adam, P. C. M. Planken, S. Meloni, and J. Dik, "TeraHertz imaging of hidden paintlayers on canvas," *Optics Express,* vol. 17, pp. 3407-3416, 2009/03/02 2009.
[97] B. Hussain, M. Ahmed, M. Nawaz, M. Saleem, M. Razzaq, M. Aslam Zia, *et al.*, "Simultaneous determination of thickness and refractive index based on time-of-flight measurements of terahertz pulse," *Applied Optics,* vol. 51, pp. 5326-5330, 2012/07/20 2012.
[98] M. Theuer, R. Beigang, and D. Grischkowsky, "Sensitivity increase for coating thickness determination using THz waveguides," *Optics Express,* vol. 18, pp. 11456-11463, 2010/05/24 2010.
[99] A. Rahman, A. Tolbert, and J. Sabol, "Terahertz application: CMP monitoring and thickness determination," 2012.
[100] W. Withayachumnankul, B. M. Fischer, S. P. Mickan, and D. Abbott, "Thickness Determination for Homogeneous Dielectric Materials through THz-TDS," in *Infrared Millimeter Waves and 14th International Conference on Teraherz Electronics, 2006. IRMMW-THz 2006. Joint 31st International Conference on*, 2006, pp. 448-448.
[101] P. U. Jepsen and B. Fischer, "Dynamic range in terahertz time-domain transmission and reflectionspectroscopy," *Optics Letters,* vol. 30, pp. 29-31, 2005/01/01 2005.
[102] J. Dai, J. Zhang, W. Zhang, and D. Grischkowsky, "Terahertz time-domain spectroscopy characterization of the far-infrared absorption and index of refraction of high-resistivity, float-zone silicon," *Journal of the Optical Society of America B,* vol. 21, pp. 1379-1386, 2004/07/01 2004.
[103] W. Withayachumnankul, J. F. O?Hara, W. Cao, I. Al-Naib, and W. Zhang, "Limitation in thin-film sensing with transmission-mode terahertz time-domain spectroscopy," *Optics Express*, vol. 22, pp. 972-986, 2014/01/13 2014.
[104] K. Davis, H. Seigneur, A. Rudack, and W. V. Schoenfeld, "PVMC Tackles c-Si Metrology Challenges," 2012.
[105] C. Richter and C. A. Schmuttenmaer, "Exciton-like trap states limit electron mobility in TiO2 nanotubes," *Nature Nanotechnology,* vol. 5, pp. 769-772, 2010.
[106] Y.-S. Lee, "Principles of Terahertz Science and Technology," 2009.
[107] X.-C. Zhang and J. Xu, "Introduction to THz Wave Photonics," 2010.
[108] G. Li, R. L. Richter Cp Fau - Milot, L. Milot Rl Fau - Cai, C. A. Cai L Fau - Schmuttenmaer, R. H. Schmuttenmaer Ca Fau - Crabtree, G. W. Crabtree Rh Fau - Brudvig, *et al.*, "Synergistic effect between anatase and rutile TiO2 nanoparticles in dye-sensitized solar cells," *Dalton Transactions,* pp. 10078-10085, 20091111 DCOM-20100122 2009.
[109] W. R. McNamara, R. C. Snoeberger Iii, G. Li, C. Richter, L. J. Allen, R. L. Milot, *et al.*, "Hydroxamate anchors for water-stable attachment to TiO2 nanoparticles," *Energy & Environmental Science,* vol. 2, pp. 1173-1175, 2009.
[110] R. A. Kaindl, M. A. Carnahan, D. Hagele, R. Lovenich, and D. S. Chemla, "Ultrafast terahertz probes of transient conducting and insulating phases in an electron-hole gas," *Nature,* vol. 423, pp. 734-738, 2003/06/12/print 2003.
[111] P. A. George, J. Strait, J. Dawlaty, S. Shivaraman, M. Chandrashekhar, F. Rana, *et al.*, "Ultrafast Optical-Pump Terahertz-Probe Spectroscopy of the Carrier Relaxation and Recombination Dynamics in Epitaxial Graphene," *Nano Letters,* vol. 8, pp. 4248-4251, 2008/12/10 2008.

[112] M. J. Paul, J. L. Tomaino, J. W. Kevek, T. DeBorde, Z. J. Thompson, E. D. Minot, *et al.*, "Terahertz imaging of inhomogeneous electrodynamics in single-layer graphene embedded in dielectrics," *Applied Physics Letters*, vol. 101, pp. -, 2012.
[113] G. L. Carr, R. P. S. M. Lobo, J. LaVeigne, D. H. Reitze, and D. B. Tanner, "Exploring the Dynamics of Superconductors by Time-Resolved Far-Infrared Spectroscopy," *Physical Review Letters*, vol. 85, pp. 3001-3004, 10/02/ 2000.
[114] S. Lupi, "Terahertz Spectroscopy of Novel Superconductors," *Advances in Condensed Matter Physics*, 2011.
[115] D. Graham-Rowe, "Terahertz takes to the stage," *Nat Photon*, vol. 1, pp. 75-77, 2007.
[116] C. W. Berry, N. Wang, M. R. Hashemi, M. Unlu, and M. Jarrahi, "Significant performance enhancement in photoconductive terahertz optoelectronics by incorporating plasmonic contact electrodes," *Nat Commun*, vol. 4, p. 1622, 2013.
[117] M. C. Beard, C. A. Turner Gm Fau - Schmuttenmaer, and C. A. Schmuttenmaer, "Progress towards two-dimensional biomedical imaging with THz spectroscopy," *Phys Med Biol.*, vol. 47, pp. 3841-3846, 20021127 DCOM- 20030514 2002.
[118] K. Kawase, Y. Ogawa, Y. Watanabe, and H. Inoue, "Non-destructive terahertz imaging of illicit drugs using spectral fingerprints," *Optics Express*, vol. 11, pp. 2549-2554, 2003/10/06 2003.
[119] M. Herrmann, M. Tani, K. Sakai, and R. Fukasawa, "Terahertz imaging of silicon wafers," *Journal of Applied Physics*, vol. 91, pp. 1247-1250, 2002.
[120] W. Withayachumnankul, G. M. Png, Y. Xiaoxia, S. Atakaramians, I. Jones, L. Hungyen, *et al.*, "T-Ray Sensing and Imaging," *Proceedings of the IEEE*, vol. 95, pp. 1528-1558, 2007.
[121] X. C. Zhang, "Terahertz wave imaging: horizons and hurdles," *Physics in Medicine and Biology*, vol. 47, p. 3667, 2002.
[122] F. Ellrich, T. Weinland, J. Klier, J. Jonuscheit, and R. Beigang, "Terahertz Waves — A New Spectral Band for Industrial Measurement Techniques," *tm - Technisches Messen*, vol. 77, pp. 452-461, 2010.
[123] B. Ferguson, S. Wang, D. Gray, D. Abbot, and X. C. Zhang, "T-ray computed tomography," *Optics Letters*, vol. 27, pp. 1312-1314, 2002/08/01 2002.
[124] S. P. Mickan and X. C. Zhang, "T-Ray Sensing and Imaging," *International Journal of High Speed Electronics and Systems*, vol. 13, pp. 601-676, 2003/06/01 2003.
[125] S. Wang and X. C. Zhang, "Pulsed terahertz tomography," *Journal of Physics D: Applied Physics*, vol. 37, p. R1, 2004.
[126] L. Minkevičius, R. Suzanovičienė, G. Molis, A. Krotkus, S. Balakauskas, R. Venckevičius, *et al.*, "Solar cell imaging and characterization by terahertz techniques," in *SPIE*, 2012, pp. 849613-849613-6.
[127] T. Arnold, M. De Biasio, W. Muhleisen, and R. Leitner, "Investigation of charge carrier dynamics in silicon wafers using terahertz imaging spectroscopy," in *Instrumentation and Measurement Technology Conference (I2MTC), 2012 IEEE International*, 2012, pp. 2478-2481.
[128] P. H. Siegel, "Terahertz Pioneer: David H. Auston," *Terahertz Science and Technology, IEEE Transactions on*, vol. 1, pp. 6-8, 2011.
[129] J. B. Baxter, C. Richter, and C. A. Schmuttenmaer, "Ultrafast Carrier Dynamics in Nanostructures for Solar Fuels," *Annual Review of Physical Chemistry*, vol. 65, pp. 423-447, 2014.

[130] M. van Exter and D. Grischkowsky, "Optical and electronic properties of doped silicon from 0.1 to 2 THz," *Applied Physics Letters,* vol. 56, pp. 1694-1696, 1990.
[131] S. E. Aw, H. S. Tan, and C. K. Ong, "Optical absorption measurements of band-gap shrinkage in moderately and heavily doped silicon," *Journal of Physics: Condensed Matter,* vol. 3, p. 8213, 1991.
[132] R. C. Newman, "Defects in silicon," *Reports on Progress in Physics,* vol. 45, p. 1163, 1982.
[133] G. E. Jellison, F. A. Modine, C. W. White, R. F. Wood, and R. T. Young, "Optical Properties of Heavily Doped Silicon between 1.5 and 4.1 eV," *Physical Review Letters,* vol. 46, pp. 1414-1417, 05/25/ 1981.
[134] A. Redo-Sanchez and X. Zhang, "10 THz Photonics," *Microwave Photonics,* p. 423, 2013.
[135] X. Lu and X.-C. Zhang, "Balanced terahertz wave air-biased-coherent-detection," *Applied Physics Letters,* vol. 98, pp. -, 2011.
[136] C.-Y. Jen and C. Richter, "Silicon wafer thickness measurement using terahertz time domain spectroscopy main," *Proc. SPIE,* vol. 8984, p. 898414, 2014.
[137] D. Ceperley, "Condensed-matter physics: Return of the itinerant electron," *Nature,* vol. 397, pp. 386-387, 1999.
[138] H. v. Löhneysen, "Electron-electron interactions and the metal-insulator transition in heavily doped silicon," *Annalen der Physik,* vol. 523, pp. 599-611, 2011.
[139] M. Dressel and M. Scheffler, "Verifying the Drude response," *Annalen der Physik,* vol. 15, pp. 535-544, 2006.
[140] N. W. Ashcroft and N. D. Mermin, "Solid State Physics," 1976.
[141] M. A. Ordal, R. J. Bell, R. W. Alexander, L. L. Long, and M. R. Querry, "Optical properties of fourteen metals in the infrared and far infrared: Al, Co, Cu, Au, Fe, Pb, Mo, Ni, Pd, Pt, Ag, Ti, V, and W," *Applied Optics,* vol. 24, pp. 4493-4499, 1985/12/15 1985.
[142] C.-Y. Tsai, C.-Y. Tsai, C.-H. Chen, T.-L. Sung, T.-Y. Wu, and F.-P. Shih, "Theoretical model for intravalley and intervalley free-carrier absorption in semiconductor lasers: beyond the classical Drude model," *Quantum Electronics, IEEE Journal of,* vol. 34, pp. 552-559, 1998.
[143] M. Auslender and S. Hava, *Handbook of Optical Constants of Solids* vol. 3: 978-0-12-544415-6, 1998.
[144] M. van Exter and D. Grischkowsky, "Carrier dynamics of electrons and holes in moderately doped silicon," *Physical Review B,* vol. 41, pp. 12140-12149, 06/15/ 1990.
[145] T. Nagashima and M. Hangyo, "Measurement of complex optical constants of a highly doped Si wafer using terahertz ellipsometry," *Applied Physics Letters,* vol. 79, pp. 3917-3919, 2001.
[146] W. Zhang, A. K. Azad, and D. Grischkowsky, "Terahertz studies of carrier dynamics and dielectric response of n-type, freestanding epitaxial GaN," *Applied Physics Letters,* vol. 82, pp. 2841-2843, 2003.
[147] M. Scheffler, M. Dressel, M. Jourdan, and H. Adrian, "Extremely slow Drude relaxation of correlated electrons," *Nature,* vol. 438, pp. 1135-1137, 2005.
[148] M. Hövel, B. Gompf, and M. Dressel, "Dielectric properties of ultrathin metal films around the percolation threshold," *Physical Review B,* vol. 81, p. 035402, 01/05/ 2010.
[149] N. Laman and D. Grischkowsky, "Terahertz conductivity of thin metal films," *Applied Physics Letters,* vol. 93, pp. -, 2008.

[150] P. Drude, "Ueber Oberflächenschichten. I. Theil," *Annalen der Physik,* vol. 272, pp. 532-560, 1889.
[151] I. C. Ho and X.-C. Zhang, "Application of broadband terahertz spectroscopy in semiconductor nonlinear dynamics," *Frontiers of Optoelectronics,* vol. 7, pp. 220-242, 2014/06/01 2014.
[152] A. S. F723-99, "Standard practice for conversion between resistivity and dopant density for boron-doped, phosphorus-doped, and arsenic-doped silicon," ed, 1999.
[153] W. R. Thurber, ed: National Institute of Standards and Technology Special Publication, 1988, pp. 289-290.
[154] P. Norton, T. Braggins, and H. Levinstein, "Impurity and Lattice Scattering Parameters as Determined from Hall and Mobility Analysis in n-Type Silicon," *Physical Review B,* vol. 8, pp. 5632-5653, 12/15/ 1973.
[155] M. M. Jevtić, D. I. Tošić, and D. A. Tjapkin, "Analysis of the infrared plasma reflectivity minimum by a self-consistent method," *Infrared Physics,* vol. 25, pp. 619-624, 7// 1985.
[156] R. T. Kinasewitz and B. Senitzky, "Investigation of the complex permittivity of n - type silicon at millimeter wavelengths," *Journal of Applied Physics,* vol. 54, pp. 3394-3398, 1983.
[157] M. Auslender and S. Hava, "Free carrier contribution to dynamic dielectric function of heavily doped semiconductors. Application to n-type silicon," *physica status solidi (b),* vol. 174, pp. 565-574, 1992.
[158] S. Hava and M. Auslender, "Theoretical dependence of infrared absorption in bulk-doped silicon on carrier concentration," *Applied Optics,* vol. 32, pp. 1122-1125, 1993/03/01 1993.
[159] K. J. Willis, S. C. Hagness, and I. Knezevic, "A generalized Drude model for doped silicon at terahertz frequencies derived from microscopic transport simulation," *Applied Physics Letters,* vol. 102, pp. -, 2013.
[160] G. A. Thomas, M. Capizzi, F. DeRosa, R. N. Bhatt, and T. M. Rice, "Optical study of interacting donors in semiconductors," *Physical Review B,* vol. 23, pp. 5472-5494, 05/15/ 1981.
[161] P. P. Altermatt, A. Schenk, and G. Heiser, "A simulation model for the density of states and for incomplete ionization in crystalline silicon. I. Establishing the model in Si:P," *Journal of Applied Physics,* vol. 100, pp. -, 2006.
[162] P. P. Altermatt, A. Schenk, B. Schmithusen, and G. Heiser, "A simulation model for the density of states and for incomplete ionization in crystalline silicon. II. Investigation of Si:As and Si:B and usage in device simulation," *Journal of Applied Physics,* vol. 100, pp. 113715-113715-7, 2006.
[163] F. Wirbeleit, "Non-Gaussian Diffusion Model for Phosphorus in Silicon Heavy-Doped Junctions," *Diffusion Fundamentals,* vol. 9, pp. 5.1-5.7, 2009.
[164] G. Arfken, *Mathematical Methods for Physicists,* 3rd ed.: Orlando, FL: Academic Press, 1985.
[165] J. del Alamo, S. Swirhun, and R. M. Swanson, "Measuring and modeling minority carrier transport in heavily doped silicon," *Solid-State Electronics,* vol. 28, pp. 47-54, 1// 1985.
[166] D. M. Caughey and R. E. Thomas, "Carrier mobilities in silicon empirically related to doping and field," *Proceedings of the IEEE,* vol. 55, pp. 2192-2193, 1967.
[167] M. Fox, *Optical Properties of Solids*: Oxford University Press, 2001.
[168] A. Fick, "Ueber Diffusion," *Annalen der Physik,* vol. 170, pp. 59-86, 1855.

[169] A. Fargi, N. Hizem, and A. Kalboussi, "Investigation of the kink effect in indium-doped silicon for sub 100 nm N channel MOSFET technology," *International Journal of Nanotechnology,* vol. 10, p. 523, 2013.
[170] A. Valletta, P. Gaucci, L. Mariucci, G. Fortunato, and S. D. Brotherton, "Kink effect in short-channel polycrystalline silicon thin-film transistors," *Applied Physics Letters,* vol. 85, pp. 3113-3115, 2004.
[171] B. G. Vasallo, J. Mateos, D. Pardo, and T. Gonzalez, "Influence of kink effect on the dynamic and noise performance of short-channel InAlAs/InGaAs HEMTs," in *Electron Devices, 2005 Spanish Conference on*, 2005, pp. 123-126.
[172] B. G. Vasallo, H. Rodilla, T. González, G. Moschetti, J. Grahn, and J. Mateos, "Kink effect and noise performance in isolated-gate InAs/AlSb high electron mobility transistors," *Semiconductor Science and Technology,* vol. 27, p. 065018, 2012.
[173] G. S. Chirikjian, *Stochastic Models, Information Theory, and Lie Groups, Volume 1*: Birkhäuser Boston, 2009.
[174] S. W. Jones, "Diffusion in Silicon," IC Knowledge LLC2008.
[175] F. F. Y. Wang, *Impurity Doping Processes in Silicon (Materials processing, theory and practices)*: Elsevier Science Ltd, 1981.
[176] T. E. Tiwald, A. D. Miller, and J. A. Woollam, "Measurement of silicon doping profiles using infrared ellipsometry combined with anodic oxidation sectioning," *AIP Conference Proceedings,* vol. 449, pp. 221-225, 1998.
[177] C. Panagopoulos and H. Badekas, "Growth of anodic SiO2 films," *Materials Letters,* vol. 8, pp. 212-215, 7// 1989.
[178] C. Y. Jen and C. Richter, "Doping Profile Recognition Applied to Silicon Photovoltaic Cells Using Terahertz Time-Domain Spectroscopy," *Terahertz Science and Technology, IEEE Transactions on,* vol. 4, pp. 560-567, 2014.
[179] C.-Y. Jen and C. Richter, "Sample Thickness Measurement with THz-TDS: Resolution and Implications," *Journal of Infrared, Millimeter, and Terahertz Waves,* pp. 1-20, 2014/07/16 2014.
[180] J. C. Irvin, "Resistivity of Bulk Silicon and of Diffused Layers in Silicon," *Bell System Technical Journal,* vol. 41, pp. 387-410, 1962.
[181] F. Séverac, F. Cristiano, E. Bedel-Pereira, W. Lerch, S. Paul, and H. Kheyrandish, "Evidence of the carrier mobility degradation in highly B-doped ultra-shallow junctions by Hall effect measurements," *Materials Science and Engineering: B,* vol. 154–155, pp. 225-228, 12/5/ 2008.
[182] P. A. Stolk, H.-J. Gossmann, D. J. Eaglesham, D. C. Jacobson, C. S. Rafferty, G. H. Gilmer, *et al.*, "Physical mechanisms of transient enhanced dopant diffusion in ion-implanted silicon," *Journal of Applied Physics,* vol. 81, pp. 6031-6050, 1997.
[183] S. Shishiyanu, R. Singh, T. Shishiyanu, S. Asher, and R. Reedy, "The Mechanism of Enhanced Diffusion of Phosphorus in Silicon During Rapid Photothermal Processing of Solar Cells," *Electron Devices, IEEE Transactions on,* vol. 58, pp. 776-781, 2011.
[184] S. W. Crowder, P. M. Rousseau, J. P. Snyder, J. A. Scott, P. B. Griffin, and J. D. Plummer, "The effect of source/drain processing on the reverse short channel effect of deep sub-micron bulk and SOI NMOSFETs," in *Electron Devices Meeting, 1995. IEDM '95., International,* 1995, pp. 427-430.

11 APPENDICES

11.A Equation Derivation for the Accurate Complex Transmission Estimation

THz Transmission $\widetilde{E_T}$ of two peaks is considered as the superposition of $\widetilde{E_{T_1}} + \widetilde{E_{T_2}}$. In this equation, air scan is defined as the reference.

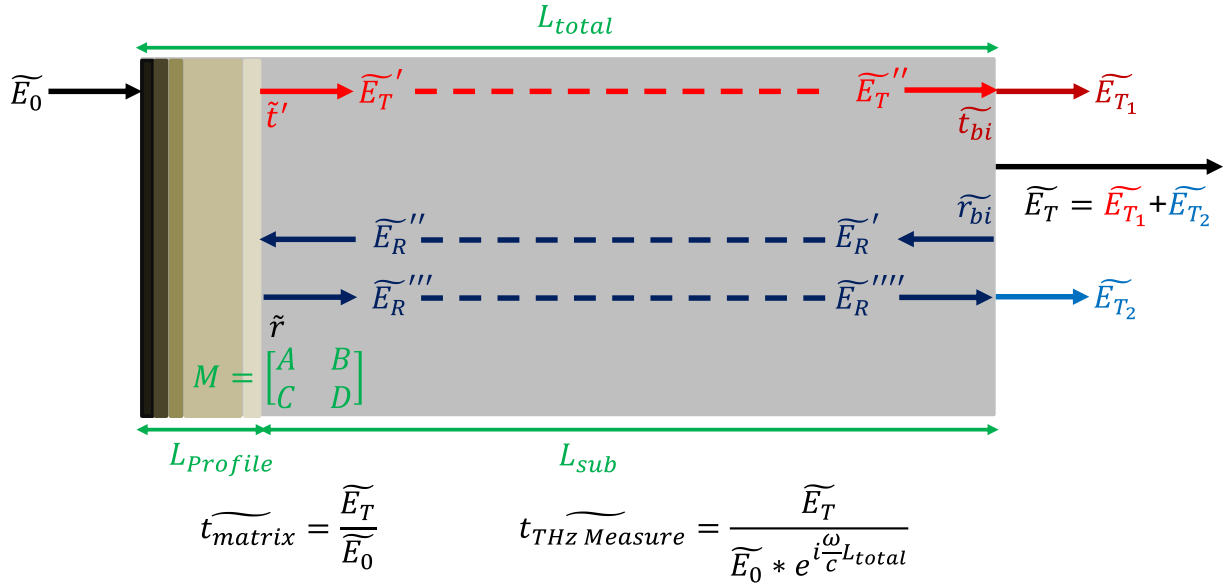

For the main peak transmission $\widetilde{E_{T_1}}$:

$$\widetilde{E_{T_1}} = \widetilde{t_{bi}}\widetilde{E_T}'' = \widetilde{t_{bi}}\widetilde{E_T}' e^{i\frac{n_{sub}\omega}{c}L_{sub}} = \tilde{t}'\widetilde{t_{bi}}\widetilde{E_0} e^{i\frac{n_{sub}\omega}{c}L_{sub}}$$

$$\Rightarrow \frac{\widetilde{E_{T_1}}}{\widetilde{E_0}} = \tilde{t}'\widetilde{t_{bi}} e^{i\frac{n_{sub}\omega}{c}L_{sub}} = \frac{2}{A+Bn_{sub}+C+Dn_{sub}} \frac{2n_{sub}}{n_{sub}+1} e^{i\frac{n_{sub}\omega}{c}L_{sub}}$$

$$\Rightarrow \widetilde{t_{THz_1}} = \frac{\widetilde{E_{T_1}}}{\widetilde{E_0} e^{i\frac{\omega}{c}L_{total}}} = \frac{2}{A+Bn_{sub}+C+Dn_{sub}} \frac{2n_{sub}}{n_{sub}+1} \frac{e^{i\frac{n_{sub}\omega}{c}L_{sub}}}{e^{i\frac{\omega}{c}L_{total}}}$$

For the 1st internal reflection peak $\widetilde{E_{T_2}}$:

$$\widetilde{E_{T_2}} = \widetilde{t_{bl}}\widetilde{E_R}'''' = \widetilde{t_{bl}}\widetilde{E_R}''' e^{i\frac{n_{sub}\omega}{c}L_{sub}} = \widetilde{t_{bl}}\tilde{r}\widetilde{E_R}'' e^{i\frac{n_{sub}\omega}{c}L_{sub}} = \widetilde{t_{bl}}\tilde{r}\widetilde{E_R}' e^{i\frac{n_{sub}\omega}{c}L_{sub}} e^{i\frac{n_{sub}\omega}{c}L_{sub}}$$

$$= \widetilde{t_{bl}}\tilde{r}\widetilde{r_{bl}}\widetilde{E_T}'' e^{i\frac{n_{sub}\omega}{c}L_{sub}} e^{i\frac{n_{sub}\omega}{c}L_{sub}}$$

$$= \widetilde{t_{bl}}\tilde{r}\widetilde{r_{bl}}\widetilde{E_T}' e^{i\frac{n_{sub}\omega}{c}L_{sub}} e^{i\frac{n_{sub}\omega}{c}L_{sub}} e^{i\frac{n_{sub}\omega}{c}L_{sub}} = \widetilde{t_{bl}}\tilde{r}\widetilde{r_{bl}}\tilde{t}'\widetilde{E_0} e^{i\frac{3n_{sub}\omega}{c}L_{sub}}$$

$$\rightarrow \frac{\widetilde{E_{T_2}}}{\widetilde{E_0}} = \widetilde{t_{bl}}\tilde{r}\widetilde{r_{bl}}\tilde{t}' e^{i\frac{3n_{sub}\omega}{c}L_{sub}} = \frac{2n_{sub}}{n_{sub}+1}\frac{An_{sub}+Bn_{sub}-C-D}{An_{sub}+Bn_{sub}+C+D}\frac{n_{sub}-1}{n_{sub}+1}\frac{2}{A+Bn_{sub}+C+Dn_{sub}} e^{i\frac{3n_{sub}\omega}{c}L_{sub}}$$

$$\rightarrow \widetilde{t_{THz_2}} = \frac{\widetilde{E_{T_2}}}{\widetilde{E_0} e^{i\frac{\omega}{c}L_{total}}} = \frac{2n_{sub}}{n_{sub}+1}\frac{An_{sub}+Bn_{sub}-C-D}{An_{sub}+Bn_{sub}+C+D}\frac{n_{sub}-1}{n_{sub}+1}\frac{2}{A+Bn_{sub}+C+Dn_{sub}}\frac{e^{i\frac{n_{sub}\omega}{c}L_{sub}}}{e^{i\frac{\omega}{c}L_{total}}}$$

$$\therefore \widetilde{t_{THz\_Measure}} = \widetilde{t_{THz_1}} + \widetilde{t_{THz_2}}$$

11.B Weighted Table used in the Destructive Doping Profile Measurement

The concept of the weighted table is to put heavier weighting values on profiles with more THz scans experienced. In the practical process, the remaining part of the profile has experienced more THz scans to own a heavier weighted number. Below table is a generalization using the well-known triangular number series to practice the weighted average in 14 THz scans and 25 profile segments. In table (a), the heavier weight (14) is put on the profile at the 14th THz scan. The value is reduced by 1 as the scan number decreases. The summation of each row is defined as the denominators to calculate the ratio in the table (b) by dividing the number in table (a). Blank areas are regions where profiles are already etched. This table can be varied by having different number of etching cycle and profile segment involved.

(a)

			THz Scan Number												
			1	2	3	4	5	6	7	8	9	10	11	12	13
Sections	000-020 nm	1	1												
	020-040 nm	2	1	2											
	040-060 nm	3	1	2	3										
	060-080 nm	4	1	2	3	4									
	080-100 nm	5	1	2	3	4	5								
	100-120 nm	6	1	2	3	4	5	6							
	120-140 nm	7	1	2	3	4	5	6	7						
	140-160 nm	8	1	2	3	4	5	6	7	8					
	160-180 nm	9	1	2	3	4	5	6	7	8	9				
	180-200 nm	10	1	2	3	4	5	6	7	8	9	10			
	200-220 nm	11	1	2	3	4	5	6	7	8	9	10	11		
	220-240 nm	12	1	2	3	4	5	6	7	8	9	10	11	12	
	240-260 nm	13	1	2	3	4	5	6	7	8	9	10	11	12	13
	260-280 nm	14	1	2	3	4	5	6	7	8	9	10	11	12	13
	280-300 nm	15	1	2	3	4	5	6	7	8	9	10	11	12	13
	300-320 nm	16	1	2	3	4	5	6	7	8	9	10	11	12	13
	320-340 nm	17	1	2	3	4	5	6	7	8	9	10	11	12	13
	340-360 nm	18	1	2	3	4	5	6	7	8	9	10	11	12	13
	360-380 nm	19	1	2	3	4	5	6	7	8	9	10	11	12	13
	380-400 nm	20	1	2	3	4	5	6	7	8	9	10	11	12	13
	400-420 nm	21	1	2	3	4	5	6	7	8	9	10	11	12	13
	420-440 nm	22	1	2	3	4	5	6	7	8	9	10	11	12	13
	440-460 nm	23	1	2	3	4	5	6	7	8	9	10	11	12	13
	460-480 nm	24	1	2	3	4	5	6	7	8	9	10	11	12	13
	480-500 nm	25	1	2	3	4	5	6	7	8	9	10	11	12	13
	Substrate		1	2	3	4	5	6	7	8	9	10	11	12	13

(b)

			THz Scan Number												
			1	2	3	4	5	6	7	8	9	10	11	12	13
Sections	000-020 nm	1	1.00												
	020-040 nm	2	0.33	0.67											
	040-060 nm	3	0.17	0.33	0.50										
	060-080 nm	4	0.10	0.20	0.30	0.40									
	080-100 nm	5	0.07	0.13	0.20	0.27	0.33								
	100-120 nm	6	0.05	0.10	0.14	0.19	0.24	0.29							
	120-140 nm	7	0.04	0.07	0.11	0.14	0.18	0.21	0.25						
	140-160 nm	8	0.03	0.06	0.08	0.11	0.14	0.17	0.19	0.22					
	160-180 nm	9	0.02	0.04	0.07	0.09	0.11	0.13	0.16	0.18	0.20				
	180-200 nm	10	0.02	0.04	0.05	0.07	0.09	0.11	0.13	0.15	0.16	0.18			
	200-220 nm	11	0.02	0.03	0.05	0.06	0.08	0.09	0.11	0.12	0.14	0.15	0.17		
	220-240 nm	12	0.01	0.03	0.04	0.05	0.06	0.08	0.09	0.10	0.12	0.13	0.14	0.15	
	240-260 nm	13	0.01	0.02	0.03	0.04	0.05	0.07	0.08	0.09	0.10	0.11	0.12	0.13	0.14
	260-280 nm	14	0.01	0.02	0.03	0.04	0.05	0.07	0.08	0.09	0.10	0.11	0.12	0.13	0.14
	280-300 nm	15	0.01	0.02	0.03	0.04	0.05	0.07	0.08	0.09	0.10	0.11	0.12	0.13	0.14
	300-320 nm	16	0.01	0.02	0.03	0.04	0.05	0.07	0.08	0.09	0.10	0.11	0.12	0.13	0.14
	320-340 nm	17	0.01	0.02	0.03	0.04	0.05	0.07	0.08	0.09	0.10	0.11	0.12	0.13	0.14
	340-360 nm	18	0.01	0.02	0.03	0.04	0.05	0.07	0.08	0.09	0.10	0.11	0.12	0.13	0.14
	360-380 nm	19	0.01	0.02	0.03	0.04	0.05	0.07	0.08	0.09	0.10	0.11	0.12	0.13	0.14
	380-400 nm	20	0.01	0.02	0.03	0.04	0.05	0.07	0.08	0.09	0.10	0.11	0.12	0.13	0.14
	400-420 nm	21	0.01	0.02	0.03	0.04	0.05	0.07	0.08	0.09	0.10	0.11	0.12	0.13	0.14
	420-440 nm	22	0.01	0.02	0.03	0.04	0.05	0.07	0.08	0.09	0.10	0.11	0.12	0.13	0.14
	440-460 nm	23	0.01	0.02	0.03	0.04	0.05	0.07	0.08	0.09	0.10	0.11	0.12	0.13	0.14
	460-480 nm	24	0.01	0.02	0.03	0.04	0.05	0.07	0.08	0.09	0.10	0.11	0.12	0.13	0.14
	480-500 nm	25	0.01	0.02	0.03	0.04	0.05	0.07	0.08	0.09	0.10	0.11	0.12	0.13	0.14
	Substrate		0.01	0.02	0.03	0.04	0.05	0.07	0.08	0.09	0.10	0.11	0.12	0.13	0.14

The reverse mapping concept can be considered as having a special weighted table shown in below. Each profile region is determined by one time scan with the weighted value "1".

			THz Scan Number													
			1	2	3	4	5	6	7	8	9	10	11	12	13	14
Sections	000-020 nm	1	1													
	020-040 nm	2	0	1												
	040-060 nm	3	0	0	1											
	060-080 nm	4	0	0	0	1										
	080-100 nm	5	0	0	0	0	1									
	100-120 nm	6	0	0	0	0	0	1								
	120-140 nm	7	0	0	0	0	0	0	1							
	140-160 nm	8	0	0	0	0	0	0	0	1						
	160-180 nm	9	0	0	0	0	0	0	0	0	1					
	180-200 nm	10	0	0	0	0	0	0	0	0	0	1				
	200-220 nm	11	0	0	0	0	0	0	0	0	0	0	1			
	220-240 nm	12	0	0	0	0	0	0	0	0	0	0	0	1		
	240-260 nm	13	0	0	0	0	0	0	0	0	0	0	0	0	1	
	260-280 nm	14	0	0	0	0	0	0	0	0	0	0	0	0	0	1
	280-300 nm	15	0	0	0	0	0	0	0	0	0	0	0	0	0	1
	300-320 nm	16	0	0	0	0	0	0	0	0	0	0	0	0	0	1
	320-340 nm	17	0	0	0	0	0	0	0	0	0	0	0	0	0	1
	340-360 nm	18	0	0	0	0	0	0	0	0	0	0	0	0	0	1
	360-380 nm	19	0	0	0	0	0	0	0	0	0	0	0	0	0	1
	380-400 nm	20	0	0	0	0	0	0	0	0	0	0	0	0	0	1
	400-420 nm	21	0	0	0	0	0	0	0	0	0	0	0	0	0	1
	420-440 nm	22	0	0	0	0	0	0	0	0	0	0	0	0	0	1
	440-460 nm	23	0	0	0	0	0	0	0	0	0	0	0	0	0	1
	460-480 nm	24	0	0	0	0	0	0	0	0	0	0	0	0	0	1
	480-500 nm	25	0	0	0	0	0	0	0	0	0	0	0	0	0	1